SUBWAVELENGTH ELEMENTS AND PLASMONIC STRUCTURES FOR SPECTRAL FILTERING

by

Alexander Frank Kaplan

A dissertation submitted in partial fulfillment
of the requirements for the degree of
Doctor of Philosophy
(Electrical Engineering)
in the University of Michigan
2013

Doctoral Committee:

Professor L. Jay Guo, Chair
Professor Nicholas A. Kotov
Professor Thomas H. Zurbuchen
Associate Professor Pei-Cheng Ku
Associate Professor Jamie Dean Phillips

DEDICATION

For the endless support and love she has given me, this dissertation is dedicated to Heidi Kaplan, my wife and best friend.

ACKNOWLEDGEMENTS

I have to begin by acknowledging the wealth of support and contributions from my advisor, L. Jay Guo, and current/past members of the Guo Research Group. In particular, I want to thank Dr. Yi-Hao Chen for working with me on negative index materials, Dr. Pran Mukherjee for our work on developing Si etch recipes, along with Dr. Haofei Shi, Yi-Kuei Wu, Dr. Ting Xu, and Dr. Jing Zhou for providing simulations in the work related to color filters and HMMs. I also want to thank Andrew Hollowell, Dr. Tao Ling, Dr. Hui Joon Park, for being fantastic colleagues and being available for discussion about projects during my Ph.D. career. I want to acknowledge the immense help from my colleague, Dr. Myung-Gyu Kang, for training me and mentoring me in my first two years. Thanks for all of those hours in the clean room. Outside of my group, I want to thank Prof. Liangbing Hu and Benjamin Wan at the University of Maryland for their recent collaboration on Li-ion battery anodes. I would like to particularly thank colleagues in the space sciences field for working together on the Si nanograting project. Dr. Jason Gilbert and Rachel Trabert at the University of Michigan put in long hours on testing chamber setup along with particle and UV measurements. Dr. Jürgen Scheer and Prof. Peter Wurz graciously assisted us with testing in their impressive MEFISTO calibration facility at the University of Bern.

I also would like to thank my dissertation committee for all of their help and contributions. My advisor, L. Jay Guo, supported my research in all of my years at the University of Michigan, finding time while I was applying for Japan to discuss his research interests and my own. Thomas Zurbuchen has provided invaluable support and career guidance. Both professors gave me fantastic opportunities through conferences and external labs to collaborate with innovative colleagues outside of my own field. I have always been able to go to Jamie Phillips and Pei-Cheng Ku to discuss ideas and research advances. My entire committee has been a great source of ideas and encouragement. Thank you, Nicholas A. Kotov for saving the day as a late addition to my committee!

I want to acknowledge all of the support of the Lurie Nanofabrication Facility. The entire staff was always supportive with tool assistance, training, and working on new processes. Current staff members such as Brian Armstrong, Rob Hower, Matthew Oonk, and Nadine Wang are valuable sources of processing information and were always ready to assist me. Brian VanDerElzen also provided a wealth of knowledge in the field of deep reactive ion etching.

I also want to thank my friends/colleagues at the University of Michigan for their moral support during this process and wish them luck on their own careers. Amongst the many friends in the University, I want to thank Grace Chen, Justin Foley, Sid Gaba, Vikrant Gokhale, Andrew Hollowell, Dr. Anne Itsuno, Christina Jones, Girish Kulkarni, Paul Schmalenberg, Vikram Thakar, and Yi-Kuei Wu. I also have to give a special thanks to Erin and Nick Ware for keeping me sane in times of mayhem and for the doggy play dates.

I would like to close by thanking my family for pushing me through one of the most rewarding experiences of my life. I couldn't have done this without the support of my wife, Heidi. My parents, in-laws, brothers, and brother-in-law probably provided more support than they knew, particularly my father-in-law, Art, whose own Ph.D. experience helped me through mine.

TABLE OF CONTENTS

Dedication……..……..…ii
Acknowledgements……..……..…iii
List of Figures……...…viii
List of Tables…….…….…..….xv
List of Appendices……..….xvi
List of Abbreviations……...…….…..….xvii
Abstract……...…….....xix

Chapter 1 Introduction 1
1.1 Free-standing Si grating particle detectors 1
1.2 Optical spectrum filters 2
1.3 Broadband absorbing IR metamaterials 3
1.4 Goal of research.....4
1.5 Simulation methods 4
1.5 Organization of thesis 4
Chapter 2 Fabrication of high aspect-ratio Si nanograting structures.....6
2.1 Introduction 6
2.1.1 Nanoimprint lithography (NIL).....6
2.1.2 Silicon deep reactive ion etching (DRIE) 7
2.2 High aspect-ratio Si nanograting fabrication.....10
2.2.1 Si nanostructures with up to (60:1) aspect-ratio.....10
2.2.2 Free-standing Si nanogratings.....16
2.3 Conclusion.....20
Chapter 3 Free-standing Si nanograting structures for UV filtration.....21
3.1 Introduction 21

3.1.1 Space particle sensors....21
3.1.2 Plasmonics....23
3.1.3 Metal-insulator-metal waveguides....27
3.2 Proposed structure....33
3.3 Fabrication....36
3.4 Testing procedure....37
3.5 Results and discussion....39
3.6 Conclusion....46
Chapter 4 Plasmonic color filters fabricated by multilayer transfer lithography....47
4.1 Introduction....47
4.1.1 Metal-insulator-metal nanostructures....47
4.1.2 Fabry Perot filters with minimal angle dependence....48
4.1.3 Contact printing overview....52
4.2 Proposed structure....53
4.3 Fabrication procedure....55
4.4 Results and discussion....56
4.5 Conclusion....59
Chapter 5 High efficiency transmission color filters with tunable bandwidth....60
5.1 Introduction....60
5.2 Proposed structure....61
5.3 Fabrication process....64
5.4 Results and discussion....65
5.5 Conclusion....67
Chapter 6 Hyperbolic metamaterial waveguides for broadband absorption....68
6.1 Introduction....68
6.1.1 Metamaterials and negative refractive index....68
6.1.2 Hyperbolic metamaterials (HMMs)....72
6.2 HMM broadband absorbers.....74
6.3 Fabrication procedure.....76
6.4 Experimental results....78
6.5 Analysis of HMM nanocavities....81

6.5.1 Effective medium simulations....81
6.5.2 Propagation in HMM waveguide....86
6.5.3 Designing the BBA....91
6.6 Conclusion....97
Chapter 7 Conclusion....98
7.1 Summary....98
7.2 Future work....99
7.2.1 Si as a plasmonic material in the UV....99
7.2.2 High aspect ratio Si and ALD for photonics applications....101
7.2.3 HMM nanostructures with high Q resonances....102
7.2.4 Si nanowall structures with CNT coating for solar cells....105
Appendices....106
References....118

LIST OF FIGURES

Figure 2.1 (a) Process flow for nanoimprint lithography and SEM images of (b) a mold and (c) replicated features from the mold in (b) [26].....6

Figure 2.2 A basic diagram showing a Si RIE process [30].....8

Figure 2.3 Process flow for a highly anisotropic gas-chopping etch [33].....9

Figure 2.4 700 nm period oxide mask (including Cr layer) (left) and resulting 6 μm deep Si gratings etched using mask (right).....11

Figure 2.5 Image showing 200 nm period, ~50% duty cycle oxide mask on Si created for etch testing in the Pegasus tool.....12

Figure 2.6 Electron micrographs of the silicon grating after (a) 3, (b) 6, and (c) 9 min of DRIE in a STS Pegasus tool [5].....13

Figure 2.7 Electron micrograph of silicon grating bars after 12 min of DRIE in a STS Pegasus tool using etch parameters listed in Table 2.1 [5].....14

Figure 2.8 Detail of top of grating bars from Fig. 2.7. The SiO_2 mask is still vertical and the duty cycle of the grating is 50% [5].....15

Figure 2.9 SEM images showing (a) tilted view of Si nanowall array and (b) a top-down image demonstrating Si nanowall feature sizes [8].....16

Figure 2.10 Images of free-standing Si gratings from Ref. [4].....16

Figure 2.11 Process outline (a)-(g) for fabrication of free-standing Si nanograting.....17

Figure 2.12 SEM image showing 1 mm period support structure etched all of the way through an SOI wafer.....18

Figure 2.13 (a) Top and (b) side view of fabricated 2.5 μm grating. (c) Diagram showing full support structure. (d) Fraction of ions exiting a 5.5 μm grating with a positive charge [39].....19

Figure 3.1 Diagram showing the operation of the LENA instrument [2].....21

Figure 3.2 Schematic of the Au gratings with a Ni support grid used in MENA [3].....23

Figure 3.3 Graphical representation showing electron oscillations on the surface of a metal at the metal-dielectric interface and accompanying fields. Note that the fields penetrate deeper into the dielectric region than the metal (decaying exponentially from the interface) and that light with H-field parallel to the surface (TM-polarized) is used to excite the oscillations [45].....24

Figure 3.4 Plots of optical constants (n, κ) of Au (left) and Si (right) over VUV to visible wavelengths. The dashed, purple line indicates the Ly-α wavelength (121 nm) while the red arrows indicate regions where the material could be considered an effective metal [48, 49].....26

Figure 3.5 Electric field profiles of surface plasmon modes for a metal-dielectric interface (left) and a symmetric (center) and anti-symmetric (right) plasmon mode in a MIM waveguide [46].....28

Figure 3.6 Propagation length (nm) vs. photon energy (eV) plots for Si-air-Si conventional waveguide modes given TE-polarized light with waveguide core width of 50 nm (left) and 70 nm (right). The length represents the point where the field has decayed to e^{-1} of its peak value. For each structure, two TE odd (antisymmetric) modes and one TE even (symmetric) mode exists in the plotted range (λ ~ 100-300 nm)……...29

Figure 3.7 Propagation length (nm) vs. photon energy (eV) plots for Si-air-Si SPP waveguide modes given TM-polarized light with waveguide core width of 50 nm (left) and 70 nm (right). The length represents the point where the field has decayed to e^{-1} of its peak value. For each structure, two TM odd (antisymmetric) modes and one TM even (symmetric) mode exists in the plotted range (λ ~ 100-300 nm)……...…30

Figure 3.8 COMSOL field profile simulations for 400 nm thick, 200 nm period grating structures with 60 nm trench widths. Plots show the z-component of the field for (a)-(b) TM and TE polarizations for Au gratings and (c)-(d) TM and TE for Si gratings and (f) also shows the y-component of the electric field (E_y) for TM-polarized light on the Si grating, demonstrating a SPP mode. The index profile (e) shows the general structure of the gratings…….….31

Figure 3.9 Figure from Ref. [60] showing a MMIM waveguide schematic. Two types of architectures were investigated, a high-low-high index (b) and a low-high-low index (c), which refer to the relative refractive indices of the materials used…….….34

Figure 3.10 COMSOL field profile simulations for 400 nm thick, 200 nm period gratings with 60 nm trench widths and 10 nm ALD coatings. Plots show the z-component of the field for (a)-(b) TM and TE polarizations for Al_2O_3-coated gratings and (c)-(d) TM and TE for Pt-coated gratings and (f) also shows the y-component of the electric field (E_y) for TM-polarized light on the Al_2O_3-coated grating, demonstrating a SPP mode. The index profile (e) shows a general ALD-coated grating structure…..…35

Figure 3.11 Diagram showing proposed Si grating (left) and ALD-coated structure (right) with typical dimensions.....36

Figure 3.12 Diagram of VUV transmission setup (bottom) and pictures of lamp and test chamber (top). The output of the discharge lamp first passes through a filter with peak transmission at Ly-α (encased in foil to prevent light leakage), then through the Si grating structure which is attached to an aperture plate on top of the photodiode..38

Figure 3.13 SEM images show the (left) top view of a fabricated 2.5 μm depth grating, (top right) side view of a fabricated 2.5 μm depth grating, (bottom right) top view of a grating coated with ~20 nm of ALD Al_2O_3, scale bars show 5 μm, 1 μm, and 500 nm, respectively.....40

Figure 3.14 SEM images show the (left) top view of 2.5 μm depth grating coated with ~20 nm of ALD Pt away from support, (top right) top view showing grating openings near support bar, (bottom right) side view of a separate fabricated structure demonstrating Pt deposition along the entire length of the trenches, scale bars show 2 μm, 1 μm, and 1 μm, respectively.....41

Figure 3.15 UV/visible transmission measurements taken from spectroscopic ellipsometer showing (left) difference between TE and TM transmission (data/simulation) through a 2.5 μm depth Si grating and (right) UV and visible transmission for Si grating, Al_2O_3 ALD, and Pt ALD structures along with simulation of unpatterned, 2.5 μm depth Si layer (green).....42

Figure 3.16 Transmission ratios for various grating samples using vacuum chamber measurement method.....44

Figure 3.17 Transmission ratio data for 3 different areas on the same Pt ALD-coated grating demonstrating the range of defects on the sample.....45

Figure 4.1 Rendition of reflection Fabry-Perot filters with varying thicknesses to create yellow, magenta, and cyan colors.....49

Figure 4.2 Simulated spectra with varying SiO_2 for the resonator dielectric layer in transmission (left) and reflection (right) structure. B/Y was obtained with 100 nm of SiO_2, G/M with 130 nm, and R/C with 170 nm.....50

Figure 4.3 Simulated reflection spectra with varying incident angle (0° to 80°) for magenta color filters with 3 different resonator layer dielectric materials: SiO_2 (n~1.45), Si_3N_4 (n~2.0), ZnSe (n~2.6).....51

Figure 4.4 Summary of results from Fabry-Perot reflective filters showing (a) diagram showing general operation of reflective filter (b) reflection data taken from reflective filters with varying Si_3N_4 thicknesses showing CMY spectra (c) data showing the change in the peak reflection dip wavelength with changing angle of incident light for data (dots) and simulation (curves) (d) SEM (left) and camera images of fabricated Si_3N_4 structures demonstrating CMY colors [72].....52

Figure 4.5 Schematic of metal transfer printing process [76].....53

Figure 4.6 (a) Schematic of the fabricated color filter structure and (b) reflection spectra of the structure with varying periods under TM-polarized illumination [17].....54

Figure 4.7 (a) Index profile of materials (dark blue = Al, red = TiO_2, light blue = air) and (b) normalized magnetic field (H_y, in/out of the page) profile for resonant wavelength and for (c) non-resonant wavelength for 220 nm period yellow filter.....54

Figure 4.8 Schematic of pattern transfer process: (a) surfactant coated SiO_2 mold (b) evaporation of Au/Al/TiO_2 followed by sputtering of thick and continuous Al (c) pressing of the mold into PC substrate and applying temperature/pressure (d) detaching PC sample (highlighted in (c)) from mold [17].....55

Figure 4.9 SEM images of 220 nm period, yellow color filter [17].....56

Figure 4.10 (a) TE and (b) TM simulations (red, dashed) and measured data (black, solid) for yellow reflective filter structure with 220 nm period along with microscope images of respective polarizations. The drop-shaped object is a region on the sample without the top Al grating, which provides a polarization independent reference for the optical images. (c) Picture of front of the final transferred structure on PC. The back (inset) looks like a flat Al film while the front shows a distinct yellow color [17]...57

Figure 4.11 (a) SEM image of fabricated 2D structure using similar process to that shown in Figure 4.8, except utilizing a 2D mold to begin and (b) reflection spectra showing little variance between TE and TM polarized reflection from the structure.....58

Figure 4.12 Graphs showing angular dependence of (a) TE, (b) TM, and (c) unpolarized reflectance spectra of yellow filter. Angle between the source and detector varies from 20° to 50° [17].....59

Figure 5.1 (a) Schematic of transmissive color filter structure and (b) Simulated transmission spectra [18].....62

Figure 5.2 Calculated dispersion of the dielectric waveguide for TM polarized light. The waveguide layer is made of Si_3N_4 with 100nm-thickness. Surrounding material is SiO_2. Green circles and red triangles correspond to simulation and experiment results, respectively. Shaded region indicates the visible spectrum [18].....64

Figure 5.3 (a) SEM image of the fabricated structure. The grating period is 420nm. (b) Comparison between experimental and simulated spectra for blue (280 nm period) and red (420 nm period) color filters. (c) SEM image showing defects in 280 nm period metal grating. Scale bar 3 μm. Optical images of (d) blue and (e) red filter illuminated by TM-polarized white light. Scale bar 5 mm [18].....65

Figure 5.4 Experimental results demonstrating tunable transmission bandwidth variation for a red (420 nm period) filter with and without oxide "buffer" layer [18].....67

Figure 6.1 Summary of results from proposed NIM research showing, on the left, a schematic, SEM image of a fabricated grating, and COMSOL H-field profile (top to bottom). On the right, the top graph plots simulated μ' for structures with varying loss parameters (α values) while the bottom graph plots the simulated n' [98]……..70

Figure 6.2 (a) Diagram showing multilayer fishnet structure (b) fabricated structure made with Ag/MgF_2 stacks using focused ion beam milling [24]……...71

Figure 6.3 (a) Example structure of planar, multilayer effective medium made of highly subwavelength sheets of Ge and Ag and (b) the resulting hyperbolic isofrequency curve (green sphere shows free-space curve) at a certain frequency [22]……73

Figure 6.4 (Left) Diagram of tapered metal-dielectric BBA grating, (center) curve and field simulations showing absorption over a broad range of wavelengths, and (right) dispersion curves demonstrating slow-light waveguide theory [21]……..75

Figure 6.5 Fabrication process and SEM images for broadband absorber structure. (Left) Process flow for fabrication of tapered metal-dielectric structures using nanoimprint

lithography. (Bottom right) SEM image of final 700 nm period structure with 9 stacks of Au-Al_2O_3 and (inset) prior to liftoff (Step 3). (scale bars represent 500 nm)……77

Figure 6.6: Data (black curve) and simulated (red curve) absorption curves for BBAs with SEM images inset. (a) 220 nm period, 3 stack structure (Al-SiO_2) absorbing from ~0.4-1.2 μm, includes angle data at 45° (dashed blue curve). (b) 700 nm period, 9 stack structure (Au-Al_2O_3) absorbing from ~1.5-3 μm. (c) 700 nm period, 11 stack structure (Au-Ge) absorbing from ~2.5-6 μm. (scale bars represent 200 nm, 500 nm, and 500 nm from (a)-(c))……79

Figure 6.7: Contour plot of absorption versus wavelength and angle demonstrating strong absorption over a wide range of angles. Simulated structure is 11-stack samples with 700 nm period and Ge/Au used for materials, targeting absorption in the mid-wave IR……...80

Figure 6.8: Contour plots showing angled absorption data compared with simulation. (a) Contour plot of simulated absorption for 3 stack, SiO_2-Al structure with 220 nm period. (b) Angled data (black box) overlaid on top of simulation plot from the left. Measured data is in the range of 45°-75°……...81

Figure 6.9 Effective medium calculations for Ag-Ge stacked structures showing (a) the effective permittivity (real (black) and imaginary (red) parts) along the direction perpendicular to propagation, (b) the effective permittivity parallel to the propagation direction, and (c) the real part of ε_{xy} for different metal fill ratios…….83

Figure 6.10 Effective medium vs. MIM stack simulations of BBA nanostructures with 700 nm period, 500 nm base width, 900 nm height, and 40% metal fill ratio. On the left, a diagram showing the metal-dielectric stack structure (20 nm Ag (blue), 30 nm Ge (light blue) in air (dark blue) on an Al substrate (red) and the absorption spectrum. On the right, a diagram and plot for an effective medium with the same fill ratio and Ag / Ge optical properties……..84

Figure 6.11 Effective medium simulations of BBA nanostructures with 700 nm period, 500 nm base width, 900 nm height, and 40% metal fill ratio. On the left, 6 profiles showing the normalized H_y at 3 different wavelengths given two media with low or high loss (γ) Ag assumed. Low-loss and high-loss absorption spectra are shown on the bottom right. Field profile simulations on the top right show non-normalized H_y at two wavelengths (3.5 μm and 4.5 μm)…….85

Figure 6.12 COMSOL field profile simulations at λ = 4.50 μm. The top right plot shows the normalized H_y, as in Figure 6.11. The time averaged power flow for the z-direction is also shown on top in the middle. The phase propagation (with arrows following a single node) is shown below. The field profiles highlight that phase propagation opposes power propagation within the waveguide……87

Figure 6.13 Figure showing example of isofreqency curve (Re(k_x) and Im(k_x) vs. k_z) normalized to k_o for λ = 4.5 μm calculated using effective medium and the hyperbolic dispersion relation (shown below). The dashed green line could represent a coupling into the HMM medium while the numbers 1 and 2 represent propagation towards or away

from the k_x=0 point (purple line). On the right, the coupling and k_x=0 points are labeled over the time averaged power flow field profile from Figure 6.12……..89

Figure 6.14 Figure showing example of hyperbolic k-space curves (k_x, k_z) normalized to k_o for λ = 3.06. 3.76, and 4.5 μm calculated using effective medium and the hyperbolic dispersion relation. Dashed lines in nanostructure reflect the point calculated using k_x ~ 5.2 when k_z=0……91

Figure 6.15 Figure demonstrating the effect of height change with constant sidewall angle (75°) and base width (bottom) on the absorption spectrum (top left). Hyperbolic isofrequency curves for 3 wavelengths are plotted in the top right……..92

Figure 6.16 Figure demonstrating the effect of sidewall angle change with constant height (700 nm) and base width (bottom) on the absorption spectrum (top left). Hyperbolic isofrequency curves over for 3 wavelengths are plotted in the top right……..94

Figure 6.17 Figure demonstrating the effect of sidewall angle change with constant top (50 nm) and base width (500 nm) on the absorption spectrum (top left). Hyperbolic isofrequency curves over for 3 wavelengths are plotted in the top right……..95

Figure 6.18 Figure demonstrating two structures for absorption in the short IR. One replaces Ge with Al_2O_3 (ε ~ 4), maintaining similar geometrical parameters (bottom left) while the other uses the same effective medium and feature sizes are decreased (bottom right). Absorption spectra show similar ranges of absorption with varying degrees of cavity confinement (top left). Hyperbolic isofrequency curves over for 3 short IR wavelengths are plotted in the top right……96

Figure 7.1 TE and TM polarized transmission through 240 nm period, 2 mm deep, 70 nm linewidth Si nanograting structure. Yellow region shows area where TE:TM extinction ratio is greater than 50…….100

Figure 7.2 Example figures from papers demonstrating annular aperture arrays (left) [143] and light funneling nanoslit structures (right) [90]…….101

Figure 7.3 High aspect-ratio Si nanoslits fabricated using deep reactive ion etching and coated with Pt using ALD……...102

Figure 7.4 Figure showing single taper (top) and dual-taper (bottom) HMM nanostructures to attain high Q absorption. Normalized magnetic field profiles demonstrate strong field enhancement at the top of the structure with a single taper and the intersection of the dual-taper…….104

Figure A.1: Diagram showing the defined size of the recessed carrier wafer for back-side etching (not to scale). Light blue is for the 4" Si carrier wafer as compared to the light gray for the SOI chip. Dark gray represents the patterned top grating area. The recessed area is shown in dark blue. The dark blue area is slightly larger than the patterned grating area, but still small enough to not overlap the SOI chip sides…110

Figure A.2: Diagram showing the defined size of the recessed carrier wafer for front-side etching (not to scale). Light blue is for the 4" Si carrier wafer as compared to the light gray for the SOI chip. Dark gray represents the patterned back-side area with 1 mm period squares. The recessed area is shown in dark blue. The central dark blue

area is slightly larger than the back-side patterned area, but still small enough to not overlap the SOI chip sides……..112

Figure B.1: Diagram showing single interface surface plasmon mode……113

Figure B.2: Diagram showing metal-insulator-metal waveguide modes…….115

LIST OF TABLES

Table 2.1 Optimized Si grating DRIE parameters [5].....12

Table 3.1 Table of complex index of refraction ($n + i\kappa$) and calculated permittivity ($\varepsilon_1 + i\varepsilon_2$, where $\varepsilon_1 = n^2 - \kappa^2$ and $\varepsilon_2 = 2n\kappa$) for materials at $\lambda = 121$ nm [48, 49].....26

LIST OF APPENDICES

Appendix A: detailed fabrication process for free-standing Si nanogratings using Pegasus 4

Appendix B: derivations of single interface plasmon modes and MIM waveguide modes

LIST OF ABBREVIATIONS

ALD	atomic layer deposition
BBA	broadband absorber/absorption
BOX	buried oxide (layer)
CMY	cyan-magenta-yellow
CNT	carbon nanotube
CSRRG	continuous split ring resonator grating
DRIE	deep reactive ion etching
EM	electromagnetic
EOT	extraordinary optical transmission
EUV	extreme ultraviolet
FOM	figure of merit
FTIR	Fourier transform infrared (spectroscopy tool)
FWHM	full-width at half maximum
GMR	guided-mode-resonance
HMM	hyperbolic metamaterial
IMI	insulator-metal-insulator
IR	infrared
LENA	Low-Energy Neutral Imager
Ly-α	Lyman-alpha
MENA	Medium-Energy Neutral Imager
MHLHM	metal-high-low-high(index)-metal
MIM	metal-insulator-metal
MLHLM	metal-low-high-low(index)-metal
MMIM	metal-multi-insulator-metal

MRWG	metallic resonant waveguide grating
NIL	nanoimprint lithography
NIM	negative refractive index material
PC	polycarbonate
PDMS	polydimethylsiloxane
PDOS	photonic density of states
PECVD	plasma-enhanced chemical vapor deposition
PVD	physical vapor deposition
QMS	quadrupole mass spectrometry
RGB	red-green-blue
RIE	reactive ion etching
RWG	resonant waveguide grating
SEM	scanning electron microscope
SiNW	silicon nanowire
SOI	silicon-on-insulator
SPP	surface plasmon polariton
SRR	split ring resonator
SSQ	Silsesquioxane
TE	transverse electric
TM	transverse magnetic
TOF	time-of-flight
TPV	thermo-photovoltaics
UV	ultraviolet
VUV	vacuum ultraviolet

ABSTRACT

Early research into devices which alter electromagnetic (EM) waves was limited by the ability to only fabricate structures on the macroscopic scale. Scientists have long proposed that devices and materials could be created to manipulate EM waves in ways not possible in nature, but this would typically require subwavelength feature sizes and confinement. The field of plasmonics provided a route around the confinement issue, for example, effectively shrinking light waves into features smaller than a half of their wavelength. Therefore, devices targeting applications for ultraviolet (UV), visible, and some infrared (IR) wavelengths would need sub-micron patterning, ideally over large areas, to achieve these results.

The flood of new fabrication techniques for creating sub-micron features has opened up new research into light manipulation. While the semiconductor industry has been able to manufacture products with features that are tens of nanometers in size using photolithography for over a decade, the cost of this method of patterning has hindered research institutions and smaller companies from attaining similar advances in photonics. This dissertation will focus on the design and fabrication of sub-micron plasmonic elements to manipulate light with wavelengths ranging from the UV to IR. These devices were also designed to be implemented with nanoimprint lithography, a method to create nano-scale features over large areas, which is useful in both laboratory and industry applications.

This work begins by reporting results for free-standing Si nanograting structures fabricated by deep reactive ion etching (DRIE) for use in near-solar particle measuring instrumentation. These structures focus on allowing solar particles to pass through for collection while simultaneously removing UV radiation which can harm the instrumentation. The theory involves shrinking a Si waveguide feature size down to less than a half wavelength of the targeted UV light (Lyman-α (Ly-α), λ~121 nm) to induce absorption but leave open area for

particle transmission through the free-standing structure. Nanogratings with >25:1 aspect ratio are fabricated into a free-standing Si layer and UV attenuation rates on the order of 10^{-4} are demonstrated while greatly improving structural stability and visible light attenuation when compared to previous designs.

Results for structures fabricated for visible light manipulation are presented next, with the focus being on device efficiency, angle dependence, and large area fabrication for use in spectral filtering applications. Novel plasmonic structures utilizing nanoimprint and transfer fabrication techniques are demonstrated in order to realize color filtration through strong absorption or high transmission of targeted visible wavelengths. A reflective, yellow filter with near perfect absorption at selected blue wavelengths is demonstrated over a large area through pattern transfer lithography. Red and blue transmissive filters are presented with some of the highest transmission efficiency (up to 90%) reported and can be easily fabricated through one patterning step. These devices could find use in a new generation of display or portable spectroscopy devices.

Finally, nano-scale structures can be used to form metamaterials with other unique optical properties. When multi-width metal-insulator structures are fabricated in stacks, with highly subwavelength layer thicknesses, an effective medium with interesting properties can be generated for the IR regime. For example, a nanostructure with hyperbolic dispersion is demonstrated, with unique waveguide properties that create broadband absorption over wide wavelength ranges. In this work, structures are demonstrated with broad absorption (> 80%) over visible, short-wave, and mid-wave IR regions by utilizing a simple fabrication process that can incorporate a variety of materials. Simulations are used to explain an ideal absorber structure by analyzing light propagation in a hyperbolic metamaterial structure. These structures have been proposed for a variety of fields including defense applications and thermo-photovoltaics (TPV).

Chapter 1

Introduction

Scientists have worked for decades to develop materials and devices which manipulate electromagnetic (EM) waves through utilization of subwavelength structures. Naturally, due to fabrication restraints, early research focused on longer wavelengths and macro-scale structures, but scientists' ambitions grew as feature sizes shrank. If structures could be fabricated on the micro- or nano-scale over large areas, a wealth of new devices could be created to manipulate wavelengths ranging from the infrared (IR) to ultraviolet (UV) regions of the spectrum.

While photolithography has long been the poster child for the microchip industry with its ability to replicate smaller and smaller feature sizes over larger and larger areas, its cost and complexity can limit its uses for small companies and universities focused on optics applications. Nanoimprint lithography has proven to be an extremely valuable tool given that it can replicate feature sizes near that of the microchip industry over relatively large areas at a fraction of the cost. Simple, periodic structures have been fabricated with feature sizes in the tens of nanometers.

If the intent is to manipulate light in the optical range of the electromagnetic spectrum, sub-micron, periodic features can be created over large areas using nanoimprint lithography. This technique allows fields of research in metamaterials, waveguides, and plasmonics, among others, to develop in the optical regime, touching innumerable applications and devices such as color displays, sensors, lithography tools, and energy generation.

1.1 Free-standing silicon grating particle detectors

Research into the composition and energy of neutral gases in the solar system has added deep insights into its origins, processes that form planetary atmospheres, and possible hazards to spacecraft. However, important questions still remain unaddressed due to the inherent limits of the technology used for these sensors. Some of the first measurement systems employed quadrupole mass spectrometry (QMS) systems [1], but these were limited by mass resolution

issues. This led to the development of the Low-Energy Neutral Atom (LENA) imager [2] specifically for low-energy (15 to 1250 eV) atoms such as neutrals in the solar wind or magnetosphere. This structure inherently filters out UV light which could lead to noise in particle measurements, but its bulky architecture is considered very expensive to send into space.

The Medium Energy Neutral Atom (MENA) imager [3] was developed to block UV light by using a gold grating in which the slits act as waveguides while still allowing particles to pass through and be measured. When they are narrower than a half-wavelength of the incident light, the waves become evanescent and cannot propagate well. The intensity for this radiation will drop exponentially. The main disadvantage of this structure lies in the durability since soft gold gratings require complicated fabrication and support structures for reliable operation.

This led to the development of a free-standing grating made entirely of Si. Si functions approximately as a metal in deep UV, allowing for impressive UV absorption while greatly improving the durability and ease of fabrication [4]. This research progressed further when I worked with the authors of Ref. [4] to develop an etch which could achieve a 6 μm deep Si nanograting with 60:1 aspect-ratio [5]. This thesis will highlight improvements on the previous Si nanograting architecture to achieve greater UV suppression by utilizing waveguide theory. New applications for Si nanogratings in optics such as UV polarizers [6-7] and solar cells or use in Li-ion batteries [8] will also be presented for future study.

1.2 Visible spectrum filters

Spectral filters operating in the visible regime are key elements in various technologies ranging from color displays and LEDs to image sensors. Despite the wide variety of fields utilizing this technology, most continue to rely on formulated chemicals, inks, and other coatings to transmit or remove desired portions of the optical spectrum. This includes the standard tri-color package of red, green, and blue (RGB) filters used in TVs [9] or films to remove IR [10] or UV [11] to improve signal detection.

Recent research has focused on thin-film, fabricated structures to overcome some of the scaling, integration, and durability issues encountered with traditional spectral filtering technology. Popular filtering structures utilize waveguide coupling [12], plasmonics [13], Fabry-Perot architectures [14], and extraordinary optical transmission (EOT) [15], as reported by Ebbesen [16]. While each of these structures seeks to exploit certain advantages, almost all

applications desire filters with high intensity, spectral control, and simple fabrication and integration. Additionally, display technology requires the ability to fabricate structures which can be viewed from a wide range of angles over large areas. With these goals in mind, this work demonstrates plasmonic spectral filters which are applicable in a wide variety of technologies with the ability to be fabricated over large areas.

This thesis summarizes the work of Ref. [17], where the fabrication of a reflective, yellow color filter with high angular tolerance using multilayer pattern transfer lithography was reported. With recent interest in reflective displays and e-paper, this device fulfills the need for a high intensity filter which is viewable over a wide angular range and can be fabricated on flexible substrates. The work of Ref. [18] is also presented where large-area transmission color filters with some of the highest peak transmission values reported in literature were created. This structure has the added advantage of controlling the bandwidth through variation of the so-called "buffer layer" thickness, making it an intriguing option for sensors and on-chip spectroscopy technology.

1.3 Broadband absorbing IR metamaterials

Similar metal-insulator-metal (MIM) structures as those mentioned above can also be used to generate resonances at IR wavelengths. Much of recent research has focused on utilizing multiple resonators packed within a subwavelength region to effectively absorb IR over a broad band of wavelengths [19-20] with the goal of creating controlled thermal emission for applications in defense or thermo-photovoltaics. A similar broadband absorber (BBA) was proposed where multiple metal-insulator layers are stacked on top of one another, supposedly creating a waveguide which slows light over a broad range of wavelengths for absorption [21].

Another interesting effect occurs when multiple metal-insulator layers with highly subwavelength thicknesses are stacked on top of one another. This essentially creates an anisotropic effective medium, or “metamaterial,” at longer wavelengths showing interesting properties not found in nature such as hyperbolic dispersion [22], extremely high photonic density of states [23], or negative refraction [24]. When these layers are patterned into a tapered nanostructure such as Ref. [21], a large range of wavelengths can be coupled into the structure and absorbed, effectively creating a BBA structure. This thesis will present results from fabricated tapered nanostructures over large areas. Thorough simulations are presented to

demonstrate the link between coupled MIM resonators and hyperbolic metamaterial theory. Ideal BBA absorption designs for various wavelength ranges are discussed and a possible application for highly sensitive field confinement is presented for future study.

1.4 Goal of research

The goal of this work is to demonstrate the effectiveness of plasmonic nanostructures for spectral filtration applications over a wide wavelength range. The ability to fabricate devices with highly sub-micron features over large areas allows for new applications that can be transferred to large-scale production. For UV wavelengths, nano-scale channels can be approximated as lossy plasmonic waveguides to filter out Ly-α radiation. As the wavelength increases, plasmonic gratings can be used to couple light into Fabry-Perot or waveguide modes to absorb or transmit specific wavelengths. Finally, as the wavelength pushes into the IR and becomes much larger than the feature size, nano-structures can begin to be approximated as meta-atoms in an overall metamaterial with unique properties that are not found in nature.

1.5 Simulation methods

The majority of spectral simulations and field profile figures are generated using COMSOL Multiphysics finite element analysis software. Some simulation work was performed for Si nanogratings using GSolver (Grating Solver), a so-called “rigorous diffraction grating analysis” software package (www.gsolver.com). This software was used during research that called for extensive simulation of gratings with a variety of structural parameters (height, trench width, periodicity) in order to reduce simulation time. Results were confirmed in COMSOL, which was then used to generate field profiles. Sources for optical constants are defined in each section, but were typically taken from Palik [48,49] or Johnson and Cristy [85] table values or a simple Drude model.

1.6 Organization of thesis

The organization of the thesis proposal is as follows: Chapter 2 will describe the fabrication of high aspect-ratio Si nanograting structures for use in particle detectors, including high aspect-ratio Si etching advances and uses of the structure in applications such as Li-ion batteries.

Chapter 3 discusses the design, simulation, and spectral testing of the free-standing Si grating structures and their connection with MIM waveguide theory. Results showing impressive UV blocking and effective particle transmission confirm their use for space instrumentation. Chapter 4 describes a thin-film, reflective color filter using gratings fabricated by pattern transfer lithography. Structures achieved precise control of color and high angular tolerance, making them useful for reflective color displays. Chapter 5 outlines a transmission grating color filter with ultra-high transmission efficiency and bandwidth control. Structures with 75-90% peak efficiencies were fabricated with variable full-width at half maximum values depending on structural parameters. Chapter 6 extends the metal-insulator structures discussed above to applications in the IR for hyperbolic metamaterial nanostructures used as broadband absorbers. Structures are demonstrated at various wavelength ranges and resonances with high angle tolerance related to the hyperbolic nature of the effective medium. Chapter 7 gives a summary and proposes future work.

Chapter 2

Fabrication of high aspect-ratio Si nanograting structures

2.1 Introduction

2.1.1 Nanoimprint lithography (NIL)

NIL was originally demonstrated in 1995 [25] with the goal of creating a new fabrication technology focused on reproducing high-resolution nanoscale features over large areas with a high rate of efficiency. The standard thermal process begins by fabricating a mold by creating a pattern using conventional lithography techniques such as photolithography, laser interference lithography, or electron beam lithography, and transferring the pattern using reactive ion etching (RIE) into a hard substrate (Si or SiO_2, for example). The pre-patterned mold is then pressed into a certain material (often, specifically formulated imprint resists) by applying high pressure and heat over a period of time. The following figure from [26] gives a basic process flow along with results from some of the smallest features created at this time:

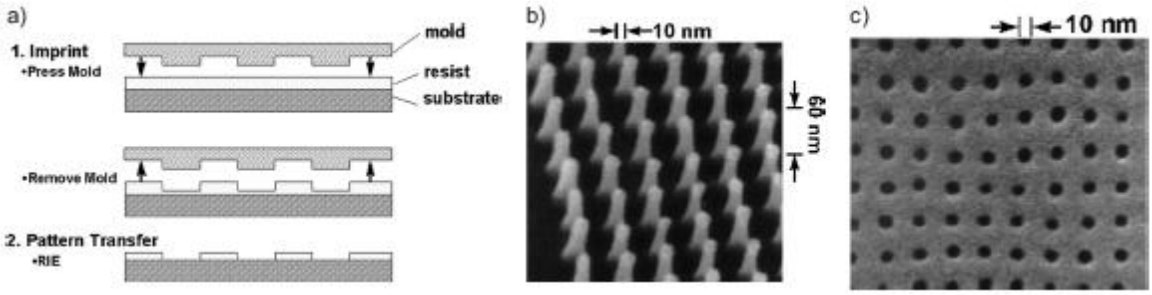

Figure 2.1 (a) Process flow for nanoimprint lithography and SEM images of (b) a mold and (c) replicated features from the mold in (b) [26].

To assist with the imprinting process, molds are often given a treatment to coat them with a surfactant that reduces sticking during the imprint process. The mold is then placed in contact with a resist-coated substrate. The two are then heated to a temperature above the so-called glass

transition temperature of the resist so that when pressure is applied to the system, the resist flows into the defined mold structure after a certain amount of time, leaving a thin residual layer to cushion the mold from direct contact with the substrate. The system is then cooled below the glass transition temperature to solidify the polymer and allow for demolding. The thin residual layer between the taller grating lines shown in Figure 2.1(a) above can then be removed through RIE and subsequent RIE or liftoff processes can then be performed using the final pattern as a mask.

It is also briefly worth mentioning that nanoimprint lithography can achieve similar results using UV-curable resists instead of the thermal process described above. While similar to the process flow in Figure 2.1(a), UV nanoimprinting involves controlled doses of UV light through the mold (which must be semi-transparent to UV) along with pressure, typically at room temperature, to allow for imprinting and curing of the resist. One important material is described in Ref. [27]. Silsesquioxane, or SSQ, materials were used in various projects because the material can easily be patterned on a flexible, plastic substrate. This material can then be given a surface treatment similar to that for Si or SiO_2 molds mentioned above and used as an imprint mold itself. These flexible SSQ molds were often useful for imprinting on surfaces which proved difficult for rigid molds, such as flexible or curved surfaces, and were also used for processes requiring multiple imprint steps where particle defects can often interfere with hard mold imprinting.

By utilizing NIL, I have been able to efficiently and repeatedly replicate grating structures over large areas suitable for optical applications. Numerous processing technologies such as roll-to-roll nanoimprint lithography [28] have been in development to be used in a factory setting to allow for fabrication on an industrial scale.

2.1.2 Deep reactive ion etching (DRIE)

Imprinted resist can be used as a mask for further etching into the substrate, but we often use the resist pattern to etch another material (metals, oxides, etc.) or define a pattern for liftoff which is then used as a mask. Creating high aspect-ratio structures using vertical etch processes has become more and more difficult as feature sizes have reduced and resist often does not stand up to long RIE processes. Selectivity between the etched material and the mask decreases with feature size as lateral etching becomes more of an issue and masks themselves typically need to be of higher aspect-ratio to achieve a similar depth. Ideally, the etch rate should be much higher

for the target material than the mask (selectivity) to achieve high aspect-ratio structures, but the vertical nature of the etch (anisotropy) also becomes more difficult to control while maintaining selectivity requirements for masking layers. If truly vertical structures are desired on the μm or nm scale, a high degree of control over the etch rate and direction must be kept without sacrificing the selectivity mentioned above.

While wet etching is still utilized for plenty of etching processes due to parameters such as ease, cost, and selectivity, obtaining ultra-high aspect-ratio nanostructures primarily resides in the realm of so-called "dry" etching techniques. These etches are inherently anisotropic, but cannot achieve nearly as high of selectivity as wet processing, particularly in direct writing processes such as focused ion beam or electron beam writing.

To achieve better selectivity while taking advantage of the anisotropic nature of dry etching, scientists typically rely on plasma processes such as reactive ion etching (RIE) [29,30]. This form of etching is a middle ground between two basic types of plasma etching: sputtering and chemical etching. Sputtering involves bombarding the substrate with energetic ions that may have no particular selectivity between materials. Naturally this creates a highly anisotropic etch, but etch rates between the mask and target material will not differ greatly, limiting the depth of the etch. The opposite end of the spectrum is plasma chemical etching. Similar to wet etching in terms of high selectivity and low anisotropy, this process involves the generation of a plasma with ions targeted to etch specific materials, but is typically done at a high pressure and low energy.

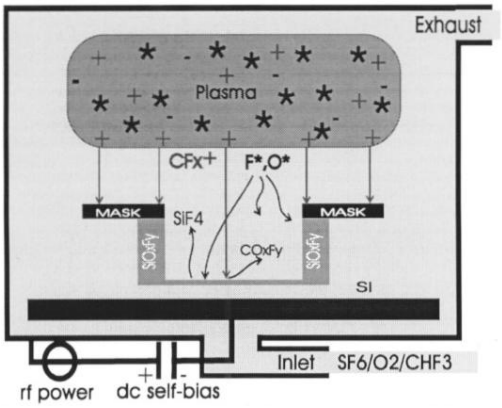

Figure 2.2 A basic diagram showing a Si RIE process [30].

RIE combines these two processes by using reactive ions along with physical bombardment (see Figure 2.2). In addition to providing a middle ground between sputtering and chemical etching, the physical bombardment of plasma ions increases the desorption of byproducts from the chemical reaction during the etch, greatly increasing anisotropy. The directionality of this process can even be improved upon with certain deep RIE (DRIE) technologies. This can involve etches performed at very low temperatures (cryogenic etches) to limit the reactions of ions with the sidewalls of a feature, thus increasing anisotropy [31], or alternating cycles of etching and passivation to protect sidewalls (Bosch etches) [32,33]. Since the latter is the process used in the work described in this chapter, more detail will be given below.

The basic process flow of a highly anisotropic, cycled, gas-chopping etch is shown in Figure 2.3.

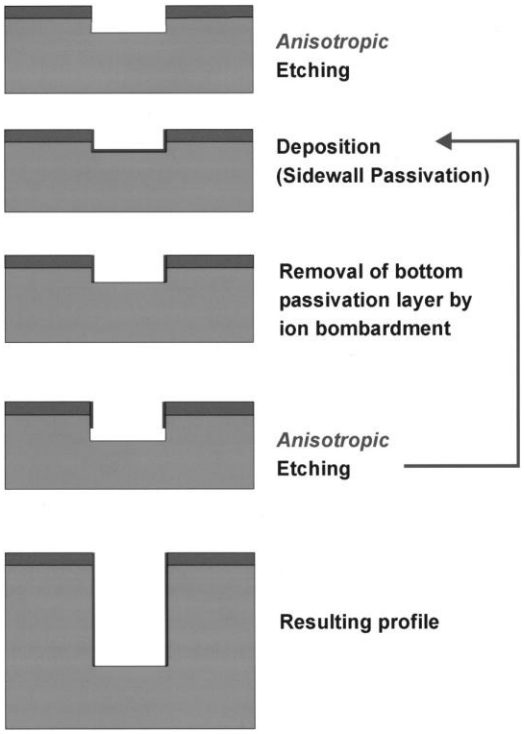

Figure 2.3 Process flow for a highly anisotropic gas-chopping etch [33].

This process can be applied to Si etching since this is a common material and the method involved in the research presented here. It begins with an etch process with SF_6 gas in the etch chemistry for a short period of time (seconds). C_4F_8 gas is then flowed during a passivation step,

creating a sidewall layer to prevent lateral etching. The process is then repeated. This time, the highly directional etch step will first remove the bottom passivation layer before continuing to etch the Si. After many cycles, this process can generate vertical, high-aspect-ratio Si structures. While not pictured in Figure 2.3, this process also generates roughness on the sidewalls with a periodicity determined by the etch/passivation cycle times. This so-called "scalloping" can cause issues in certain applications and will be discussed later.

2.2 High aspect-ratio Si nanograting fabrication

High aspect-ratio Si etches have become more desirable as applications involving nanoscale structures with high thicknesses have grown. These applications often necessitate nanoscale features for interaction with light or small particles, as well as a larger surface area or depth for the interaction to occur. Perhaps the most common high aspect ratio Si structure being researched is the nanowire (SiNW). Papers such as Ref. [34] have utilized nanoimprint lithography along with DRIE processing to create SiNW structures over large areas with aspect ratios >50:1. Silicon wires have been proposed for applications including solar cells [35] and even Li-ion battery anodes [36], as will be discussed later. Others have sought to create high aspect ratio Si nanoholes [37] using nanoimprint and DRIE with the objective of fabricating a membrane to separate particles of certain sizes.

The application related to the research presented here involves fabricating Si nanogratings, targeting applications such as space-based particle sensors [4], x-ray diffraction gratings [5], or even a possible polarizer for short wavelength UV light, similar to Ref. [6]. Achievements in Si DRIE were also applied to fabricate high aspect-ratio nanowalls structures for use in Li-ion battery anodes [8]. These applications not only require high aspect ratios, but features of around 100 nm or less, often with smooth sidewalls (low scalloping). The following reviews the results of etches targeting the fabrication of these high aspect ratio structures.

2.2.1 Si nanostructures with up to (60:1) aspect ratio

The Si etching work performed with Pran Mukherjee of the Massachusetts Institute of Technology and summarized in Ref. [5] was achieved by a variety of etches and modifications to recipes using the Pegasus DRIE tool utilizing a Bosch process manufactured by STS. With greater control over gas flow, power, and etch/deposition time, this tool can provide deeper structures with smoother sidewalls over much larger scales than previous works [4, 38].

Oxide or metal masks provide the best selectivity in the Pegasus tool due to the etchant gases used. SiO_2 masks were chosen to reduce tool contamination and created on Si wafers initially using nanoimprint lithography as a patterning method. Si wafer pieces were created with approximately 250 nm of thermally grown oxide. Approximately 10 nm of Cr was deposited on the samples to act as a mask for patterning the oxide. 700 nm gratings were then imprinted on the surface using mr-I 8030 (Microchem) resist and a Nanonex NX2000 imprinter (Nanonex, NJ). The residual resist layer was then etched using RIE. The remaining resist was used as a mask for etching of the Cr. After removal of the resist with acetone, the Cr mask was used for etching of the oxide layer to create a 700 nm period mask with a duty cycle of approximately 75% (see Figure 2.4(left)). After the Cr was removed, the samples could be used in the Pegasus for Si etch testing.

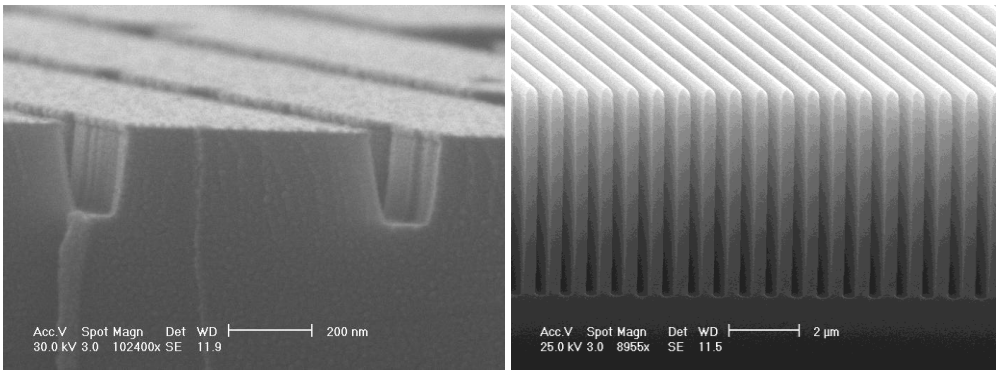

Figure 2.4 700 nm period oxide mask (including Cr layer) (left) and resulting 6 μm deep Si gratings etched using mask (right).

After optimization of various gas flows, platen and coil powers, etch/deposition times, and temperatures (Table 2.1), 6 μm deep Si gratings were etched using the Pegasus tool with low sidewall roughness (Figure 2.4(right)). This process was then tested to create 200 nm period gratings with the goal of reaching an aspect ratio greater than 50:1 (height vs. trench width). The process to create the oxide grating mask used in these tests (outlined in Ref. [5]) was performed by other colleagues at the Massachusetts Institute of Technology. Figure 2.5 shows the final oxide mask created.

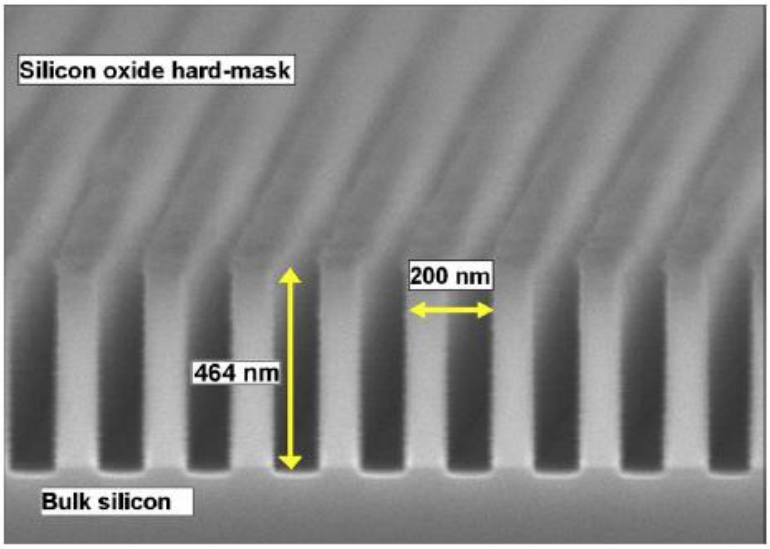

Figure 2.5 Image showing 200 nm period, ~50% duty cycle oxide mask on Si created for etch testing in the Pegasus tool.

Using these oxide gratings as a mask, various tests were run to optimize the original recipe for smaller features. The final Si etch process used to create the images in the figures below is summarized in the Table 2.1.

TABLE II. Grating DRIE parameters.

Device parameter	Deposition cycle	Etch cycle
SF_6 Flow rate (SCCM)	0	200
C_4F_8 Flow rate (SCCM)	150	80
Coil power (W)	2000	1100
Platen power (W)	0	30–60[a]
Cycle time (s)	1	1.5
Base pressure (mTorr)	7.5	
Chuck temperature (°C)	−15	

[a]Linear ramp over 12 min.

Table 2.1 Optimized Si grating DRIE parameters [5].

To begin, etch and deposition cycle times were set to some of the lowest values allowable on the tool (~ 1 second) with the aim of reducing scalloping, which can greatly affect the optical properties of the final structure. Similar to the cryogenic etch mentioned earlier [31], the chuck temperature was set to -15 °C to reduce sidewall etching. The base pressure was also kept as low as possible (depending on the gas flow, 7.5-10 mTorr can be achieved with little fluctuation) to

increase the ion mean free path. Various etches were then run to optimize gas flow and power to achieve the results given below. It is important to note that the bias (platen) power used in the etch cycle is linearly ramped, increasing as the etch progresses deeper, to reduce undercut and promote selectivity at the beginning of the etch while providing high enough power as the etch progressed deeper.

Figure 2.6 shows a progression of the etch depth from 2 μm to 5 μm with etch times of 3 minutes to 9 minutes while Figure 2.7 shows the final 6 μm deep etch after 12 minutes.

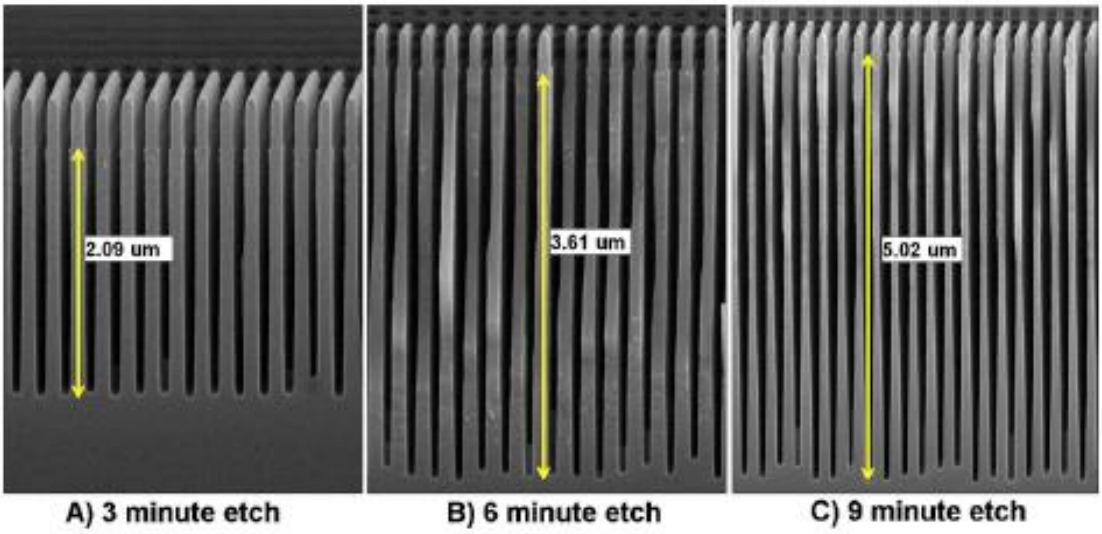

Figure 2.6 Electron micrographs of the silicon grating after (a) 3, (b) 6, and (c) 9 min of DRIE in a STS Pegasus tool [5].

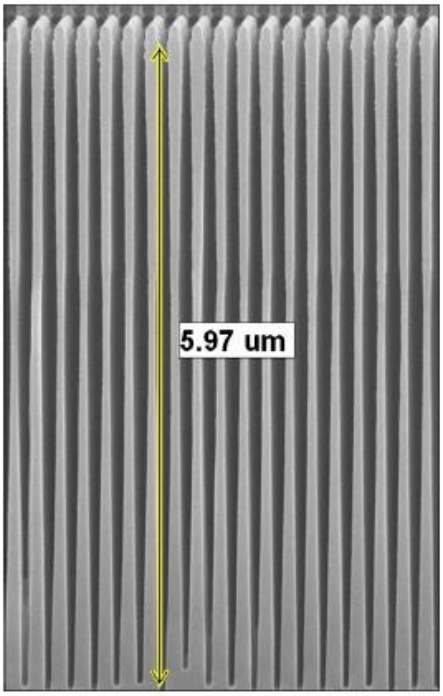

Figure 2.7 Electron micrograph of silicon grating bars after 12 min of DRIE in a STS Pegasus tool using etch parameters listed in Table 2.1 [5].

These results show a 60:1 aspect ratio grating was achieved using DRIE. Figure 2.8 shows that some of the oxide mask still remains, leaving the possibility of deeper structures. However, issues with the reduction in Si line-width due to mask erosion, often called "bowing," midway through as the grating etch progresses would need to be resolved. Referring to Figures 2.7 and 2.8, one can clearly see that the Si line-width decreases from just over 100 nm at the top to tens of nanometers near the middle of the etch. This bowing can occur due to the tapered nature of the mask, lack of selectivity, or charging of the mask causing ion deflection, leading the mask to wear away at the edges as the etch progresses deeper or cause reduction in the Si line width. The issue may possibly be mitigated by using a mask with better selectivity, such as a metal, but we note that metals were not allowed in the chamber at the time of fabrication.

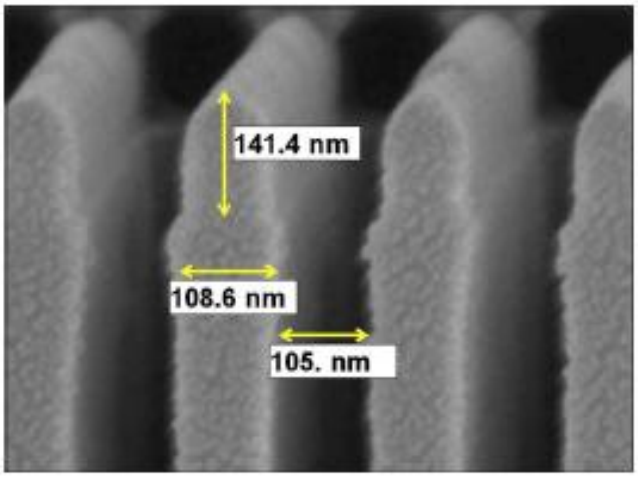

Figure 2.8 Detail of top of grating bars from Fig. 2.7. The SiO_2 mask is still vertical and the duty cycle of the grating is 50% [5].

This procedure was also utilized in the fabrication of high aspect-ratio Si nanowall structures for use in Li-ion battery anodes. As summarized in Ref. [8,36], Si has an extremely high capacity for storing Li, making it a targeted material for battery applications. However, the material expands and contracts during charging and discharging, requiring nanostructures with spacing in between to allow for large volume changes. Si nanowall structures with features as small as 50 nm but approximately 1 μm tall were fabricated using a DRIE process (Figure 2.9) since they can achieve the impressive stability of SiNWs while having a lower surface area improves initial charging efficiency, making them more applicable for higher power applications.

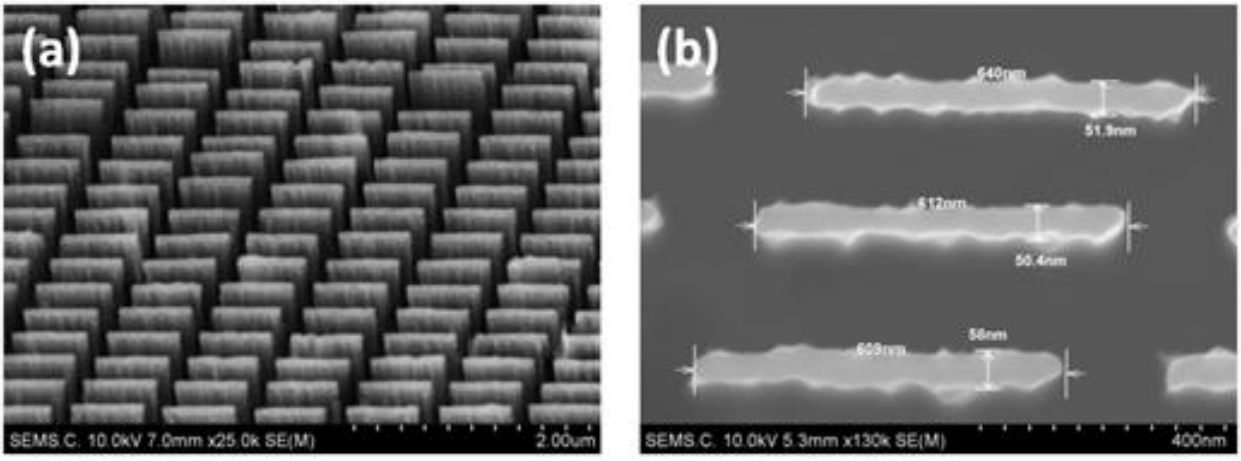

Figure 2.9 SEM images showing (a) tilted view of Si nanowall array and (b) a top-down image demonstrating Si nanowall feature sizes [8].

2.2.2 Free-standing Si nanogratings

In previous work, a self-supported, Si nanograting with sub-100 nm trench widths and high aspect-ratio was proposed for blocking UV light while still allowing particles to pass through [4, 38] (Figure 2.10).

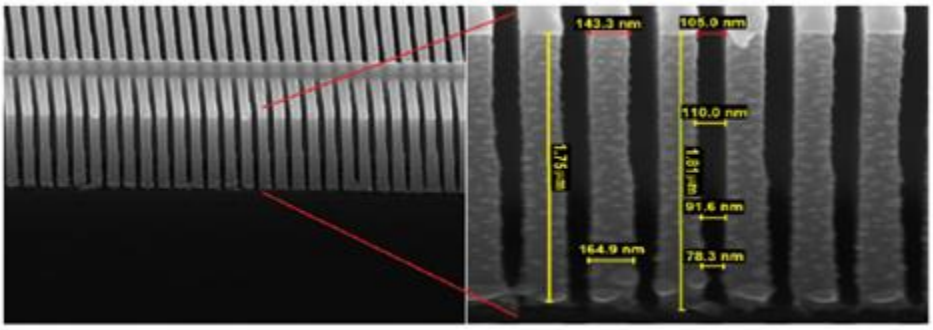

Figure 2.10 Images of free-standing Si gratings from Ref. [4]

While a more detailed discussion will be presented in Chapter 3, the primary wavelength these gratings were designed to absorb was approximately 121 nm, known as the Lyman-alpha (Ly-α) wavelength. This is the primary UV wavelength emitted by the Sun and it is extremely harmful to equipment used to measure particle properties in space instrumentation. By fabricating gratings with periods larger than the wavelength (220 nm, in this case) but trench widths less than 1/2 of the size (~60 nm or less) and thicknesses of 2 μm or greater, each slit can be treated a lossy waveguide which absorbs the harmful UV light while still allowing particles to pass

through and be collected for measurement. While obtaining impressive results, new structures and fabrication techniques have been proposed to create taller gratings with narrower trenches, smoother sidewalls, and new material coatings to achieve better UV blocking.

To utilize the impressive new tool and etch results detailed above, I altered the procedure to create new free-standing grating structures for further testing. A detailed schematic of the process is shown in Figure 2.11.

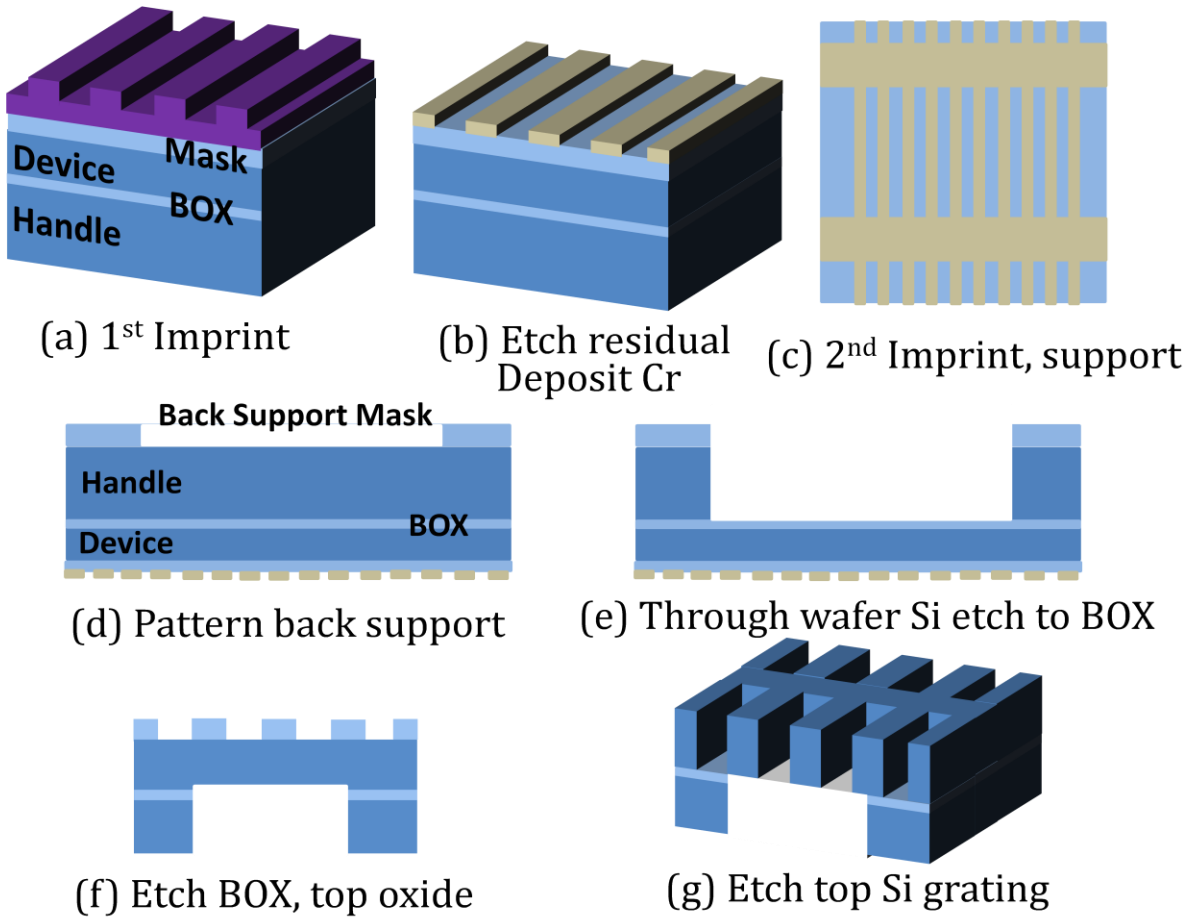

Figure 2.11 Process outline (a)-(g) for fabrication of free-standing Si nanograting.

The process begins with a silicon-on-insulator (SOI) wafer. Figure 2.11(a) includes a diagram showing a rough cross section of the wafer (not to scale) and the terminology used for the fabrication procedure. The "device" layer is the top layer of the SOI wafer and this thickness determines the final height of the grating (a few μm thick). The buried oxide layer ("BOX") is beneath the device layer (a few hundred nm thick). The "handle" makes up the majority of the

wafer thickness and is typically a few hundred μm thick. As shown in Figure 2.11(a), an oxide "mask" layer is deposited on the SOI wafer using plasma-enhanced chemical vapor deposition (PECVD). Imprint resist (mr-I 8030) is then patterned into a 220 nm grating on the sample using imprint lithography (Nanonex NX2000). After etching of the residual layer, Cr can be deposited by e-beam evaporation and following liftoff, a 220 nm period Cr grating is generated on the "mask" oxide layer. Figure 2.11(c) involves repeating the previous process steps to create an 11 μm period Cr grating perpendicular to the 220 nm period grating that will eventually define a support structure in the Si using the same process as Figure 2.11(a) and (b).

With the top Cr mask ready, the sample is then flipped over. A thick oxide layer is deposited on the back of the SOI wafer using PECVD and a photoresist (SPR 220, Microchem) is spun onto the back. This photoresist is then exposed with a large, back-side Si support pattern which is used as a mask to etch the thick oxide layer on the back as shown in Figure 2.11(d). This structure consists of a 1.5 cm x 1.5 cm crossed pattern with a 1 mm period and 150 μm linewidth at an angle of approximately 45 degrees with the 220 nm period grating on the opposite side of the wafer.

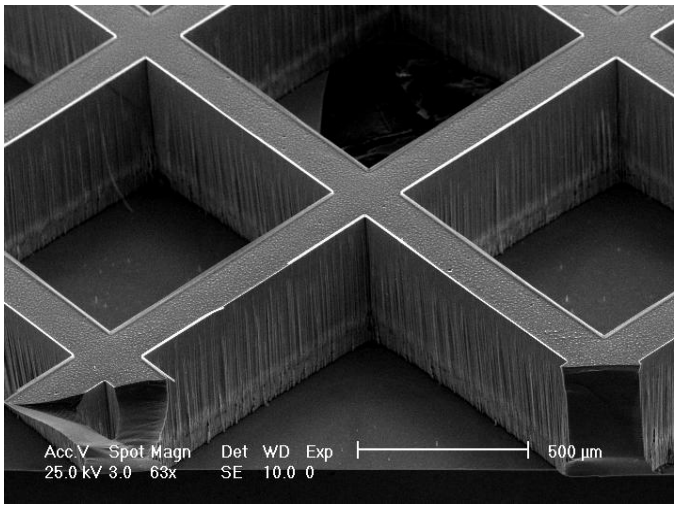

Figure 2.12 SEM image showing 1 mm period support structure etched all of the way through an SOI wafer.

In Figure 2.11(e), using this newly patterned thick oxide layer as a mask, the Si "handle" layer of the sample is etched using the Pegasus tool (see Figure 2.12). This etch progresses until the "BOX" layer is reached. In Figure 2.11(f), the top oxide "mask" layer is etched using the Cr

grating as a mask. Also, the "BOX" layer is then removed using a normal oxide etching process in a RIE tool. This opens a window of bare Si which will be the areas where the final Si grating is free-standing. After removal of the Cr grating, the oxide is used as a mask to etch the "device" layer Si until it etches completely through into the areas opened by the back side etch (Figure 2.11(g)). This creates the final Si grating structure. A more detailed process is described in Appendix A.

Figure 2.13 shows SEM images of the final structure for a 2.5 μm thick, free-standing Si grating fabricated using the process above, but the same process steps were used with different SOI wafers to create gratings with different device layer thicknesses (4.5 and 5.5 μm, for example).

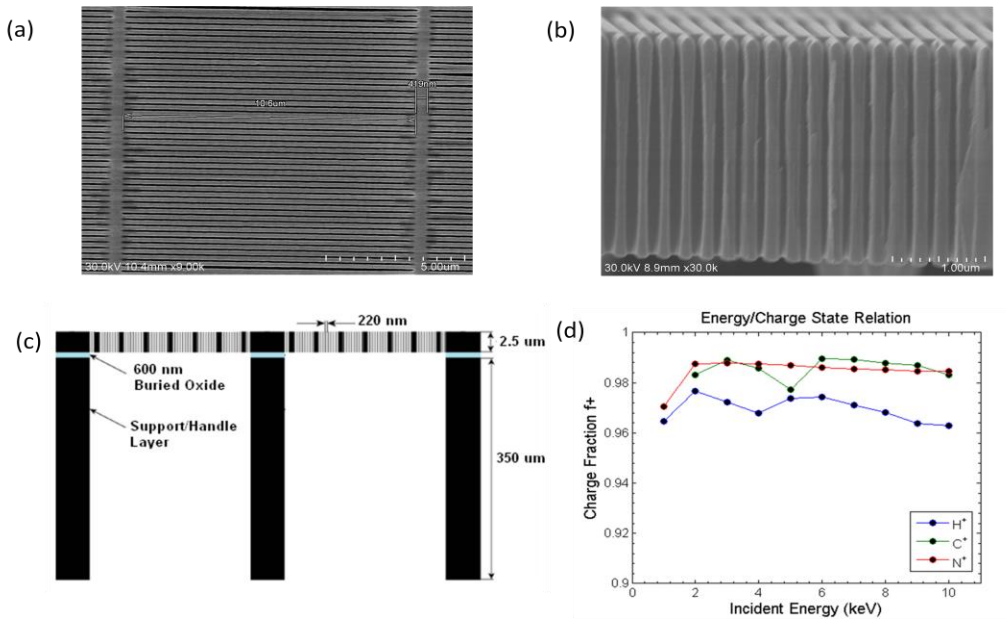

Figure 2.13 (a) Top and (b) side view of fabricated 2.5 μm grating. (c) Diagram showing full support structure. (d) Fraction of ions exiting a 5.5 μm grating with a positive charge [39].

Example ion transmission results were run on a 5.5 μm thick grating to confirm the passage of particles and the full etching of the device layer. The results show the fraction of various types of incident positive ions (H^+, C^+, N^+) exiting the 5.5 μm grating with a positive charge as a function of incident energy. With values of approximately 96% and above for transmission, these results demonstrate little alteration in the ion charge or energy when passing through the trenches [39]. Overall, approximately 10% of incident ions were transmitted as compared to an open hole,

similar to results reported for previous structures [40], and approximately equal to the expected open area of the gratings.

With the advances made in Si etching outlined above, free-standing Si nanogratings with higher thicknesses, narrower trenches, and reduced scalloping were created, improving on the results presented in Ref. [4, 38]. While these structures could provide impressive UV blocking on their own while allowing particle transmission, Chapter 3 will outline further improvements to the structure brought about by improved understanding of the UV suppression mechanism of free-standing Si nanogratings.

2.3 Conclusion

Si nanogratings were etched using a newly designed DRIE recipe outlined above, achieving some of the highest recorded aspect ratios for etched nanostructures using DRIE, approximately 60:1. Primarily, the results presented here were utilized to further research in deep UV suppressing particle filters for use in space-based applications (Chapter 3), achieving higher aspect ratios than previously reported results, but the work was also applied to fabrication of Si nanowall structures for use as Li-ion battery anodes. With these capabilities, advancements in applications such as UV suppression for particle sensors and x-ray spectroscopy can continue. This etch process can also be applied to create other high aspect ratio Si structures as mentioned earlier (nanowires, nanoholes, etc.) for applications such as solar cells or high-aspect ratio templates for creating other nanostructures.

Chapter 3

Free-standing Si nanogratings for UV filtration

3.1 Introduction

3.1.1 Space particle sensors

While over 50 years have passed since the launchings of Sputnik and Explorer I, many unanswered questions remain regarding the origins of our solar system. Since then, numerous missions have been sent throughout space with a variety of instruments to gather data on the space environment around Earth, other planets, and to the edge of our solar system. In-situ measurements near the Sun have been some of the most coveted data in understanding the continuous source of particles flowing out from the Sun called the solar wind.

Quadrupole mass spectrometry (QMS) systems were used in some of these first measurements, but more recently on the Huygens probe [1]. Another example of a recent instrument is The Energetic Particle and Plasma Spectrometer on the MESSENGER mission [41]. Many of the QMS systems require a high particle flux or they become hindered by mass resolution and throughput issues. Some sensors also require ionized particles for measurement and cannot collect reliable data on neutrals. The Low-Energy Neutral Atom (LENA) imager (shown in Figure 3.1) was designed to combat these issues and measure low-energy neutral atoms such as those from the solar wind.

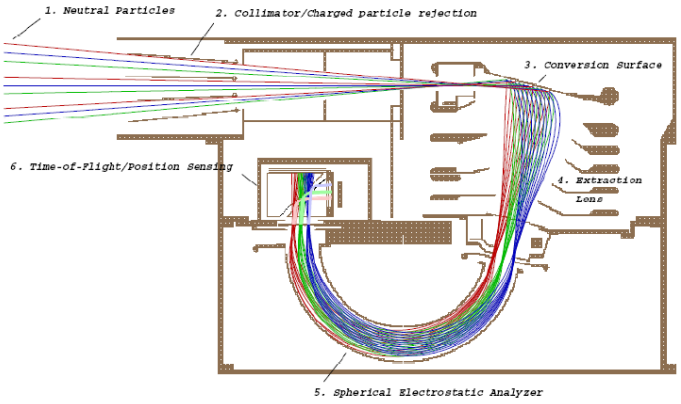

Figure 3.1 Diagram showing the operation of the LENA instrument [2].

LENA suppressed ions and electrons while ionizing a fraction of incident neutrals via charge-exchange after impact on a polished, highly negative conversion surface. This highly negative surface injects the particles into an electrostatic deflection system which suppresses the high flux of Lyman-α (Ly-α) and other EUV wavelengths. In many environments, the ratio of Ly-α to neutrals typically ranges from 10^{10}-10^{12}, by far the most dominant, and can wreak havoc with the signal-to-noise ratio. The ions are accelerated to high energies before passing through a carbon foil, which generates start electrons, and the speed is measured with a time-of-flight (TOF) telescope similar to that in [41]. The key enabling subsystems for LENA are the EUV/ Ly-α suppression, and the charge exchange surface. It is important to note that this was achieved by utilizing a heavy (>20 kg) and therefore high-cost system, which is often not feasible for long-distance space voyages.

One structure to address the issues listed above with a more lightweight architecture was the Medium-Energy Neutral Atom (MENA) imager [3]. The idea behind the structure is to use nanoscale grids which would effectively filter UV radiation while allowing particles to pass through. While more information will be given in Section 3.1.3, one can define the grating trenches as lossy waveguides when they are narrower than a half-wavelength of the incoming light, leading to evanescent fields that decay at a rate of $e^{-\propto z}$, where α and z represent an absorption coefficient and the grating depth, respectively. The structure used for MENA is shown in Figure 3.2. The final structure flown on the mission consisted of ~400 nm thick Au lines with ~60 nm trench widths (200 nm period), achieving suppression on the order of 10^{-5} of Ly-α. These results opened a new field of devices, but the Au gratings are created using interference lithography and electroplating to fill gaps in photoresist with Au, greatly limiting the aspect ratio and area of the structure. Also, the lines are not very robust and a Ni support structure is required which can be difficult to fabricate and could create mismatch issues when the device is heated to high temperatures.

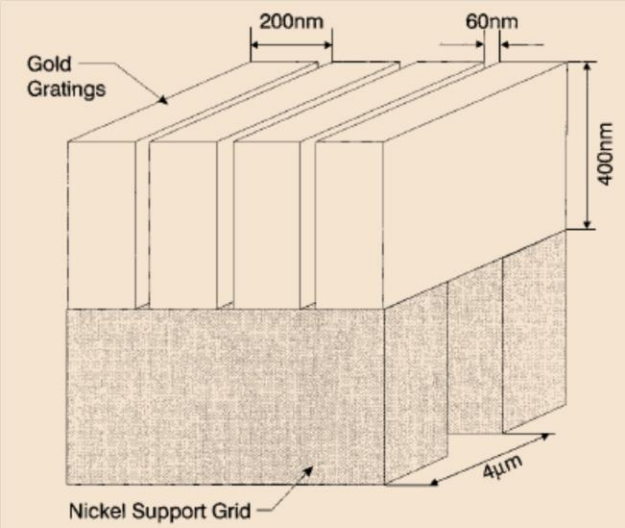

Figure 3.2 Schematic of the Au gratings with a Ni support grid used in MENA [3].

Self-supported, single material Si gratings fabricated by NIL were then researched as outlined earlier in Section 2.2.2, providing a much less complicated fabrication procedure, a stronger material, and a much larger area (see Figure 2.10) [4,38]. These structures were tested with a xenon arc lamp for the UV (188–385 nm) and achieved transmission values as low as 10^{-4}. Issues such as wider than desired trench widths could have caused higher than expected transmission values at these wavelengths, as well as scalloping, but a further understanding of the nature of light propagation in this structure has brought to light impressive improvements in UV blocking by understanding the changes in the nature of waveguides using Si.

3.1.2 Plasmonics

Many recent textbooks [42, 43] and review papers [44-46] have been written on the subject of plasmonics and cover the breadth of material much more thoroughly than needed here. The key points summarized below are primarily to assist with the understanding of metal-insulator-metal (MIM) waveguide structures which will be referred to throughout this work. Hosts of other papers have been published reviewing plasmonics for a variety of applications, but only the few cited above will be referred to here.

Plasmonics is a field describing the interaction between light and metal through the idea that waves (if given the proper momentum) can couple to oscillations of free electrons on the surface of a metal surrounded by a dielectric. Figure 3.3 below shows a typical graphic used to illustrate this phenomenon.

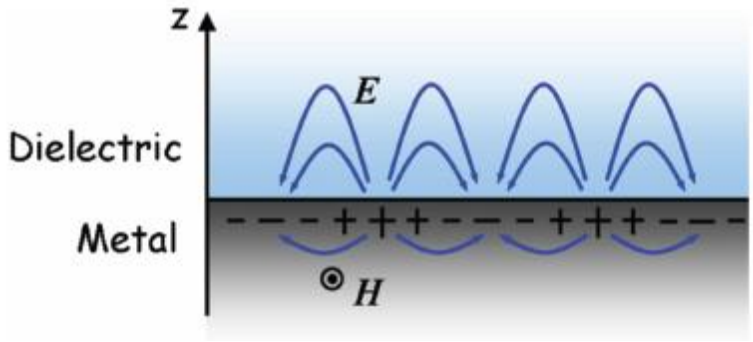

Figure 3.3 Graphical representation showing electron oscillations on the surface of a metal at the metal-dielectric interface and accompanying fields. Note that the fields penetrate deeper into the dielectric region than the metal (decaying exponentially from the interface) and that light with H-field parallel to the surface (TM-polarized) is used to excite the oscillations [45].

Along with the electron oscillations, the figure also shows that there is a highly localized electromagnetic field which propagates along with the oscillations and can even be coupled out after propagation. The combination of the oscillations and field are called a surface plasmon polariton (SPP). This strong localization also means that the field is very strongly enhanced near this surface, leading to a host of new sensor or solar cell architectures that primarily rely on the thin region near the metal. The field actually decays exponentially away from the interface, penetrating much deeper into the dielectric region than the metal. The figure also shows the H-field is polarized in and out of the page, showing that transverse magnetic or TM-polarized light is used to excite the oscillations. These aspects of the field will become particularly important when analyzing MIM structures.

One of the primary fields which was heavily researched in plasmonics was its use for chip-scale guiding of signals in an effort to replace current electrical technology. Researchers have studied the idea of replacing lossy electrical circuitry where large amounts of heat are generated with waveguides where light could propagate much faster throughout the "circuit," but photonics would run into a road block with traditional waveguides. Dielectric waveguide structures are limited by their size and are not able to effectively confine light with λ much larger than the core thickness, leading to much larger structures than their electrical counterparts. Nanoscale sizes and optical elements did not mix until the field of plasmonics was introduced. While other structures have been explored, MIM waveguides are one of the primary technologies targeted for chip-scale integration due to their ability to confine visible light in nanometer-scale

cavities (much smaller than $\lambda/2$) that could lead to propagation over relatively long distances with the proper materials. The theory behind these structures is summarized in the next section.

Before analyzing these structures, a final area to investigate is over what region certain materials exhibit more metallic properties, and therefore over what wavelength range they may become more useful as a plasmonic material. Although there has been much recent research in non-traditional plasmonic materials [47], metals are typically the go-to material when it comes to plasmonics at visible wavelengths. The majority of these materials have a bulk plasma frequency (ω_p) (the resonance frequency of the free electrons or damped oscillators on the surface of the material) in or near the visible spectrum. At frequencies much lower than ω_p, the light will not penetrate well into the material and reflectivity is high, just like we would expect for a metal. Under these conditions, the complex index of refraction ($n + i\kappa$) of the material is characterized by low n and high κ (relating to absorption loss). This can also be characterized using dielectric permittivity ($\varepsilon_1 + i\varepsilon_2$, where $\varepsilon_1 = n^2 - \kappa^2$ and $\varepsilon_2 = 2n\kappa$), leading to materials with metallic properties being characterized by a large, negative ε_1 and a positive ε_2.

At frequencies very close to or higher than ω_p, the metallic properties of the material begin to break down. In the case of most metals (outside of Al, which has a plasma frequency in the deep UV), this means that they do not approximate metals at VUV wavelengths, our region of interest. Figure 3.4 shows plots of Au (the material used in the MENA instrument) and Si (our proposed material for fabrication) over UV/visible wavelengths, with the Ly-α wavelength labeled with a dashed, purple line. The effective regions where each material more closely approximates a metal in terms of optical properties (negative ε_1, for example) are roughly shown by the red arrows. Table 3.1 shows the (n, κ) values at Ly-α (121 nm) for materials of interest. All values are from experimental data retrieved by Palik [48, 49].

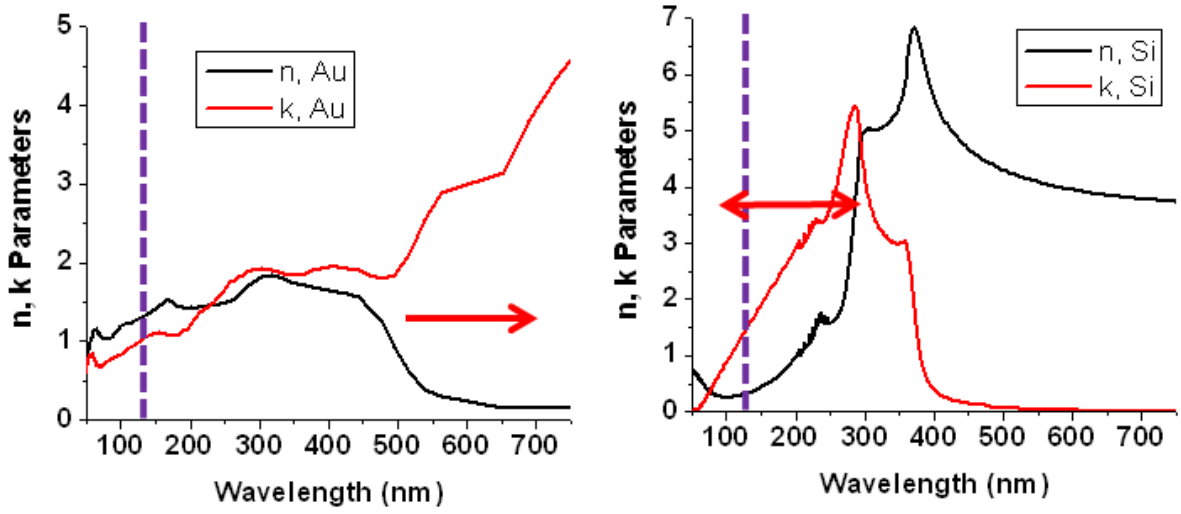

Figure 3.4 Plots of optical constants (n, κ) of Au (left) and Si (right) over VUV to visible wavelengths. The dashed, purple line indicates the Ly-α wavelength (121 nm) while the red arrows indicate regions where the material could be considered an effective metal [48, 49].

Material	n (Palik)	κ (Palik)	ε_1	ε_2
Si	0.295	1.3	-1.6	0.767
Al	0.044	1.18	-1.39	0.104
Au	1.265	0.967	0.67	2.447
Pt	1.35	1.18	0.43	3.186
Al_2O_3	2.519	0.629	5.95	3.169

Table 3.1 Table of complex index of refraction (n + iκ) and calculated permittivity ($\varepsilon_1 + i\varepsilon_2$, where $\varepsilon_1 = n^2 - \kappa^2$ and $\varepsilon_2 = 2n\kappa$) for materials at λ = 121 nm [48, 49].

As is expected by theory, Au does not operate well in terms of optical properties as a metal at λ = 121 nm. The plasma frequency of Au is in the visible spectrum (producing its yellowish color), and it more closely approximates a lossy dielectric with n ~ 1 at UV wavelengths. Meanwhile, Si proves to have more metallic optical properties in this regime, similar to Al, which has a plasma frequency in the VUV. Although not often mentioned, it was

reported in Ref. [50] through electron loss measurements that Si has a volume plasmon energy of ~16 eV, or around λ_p = 77 nm, similar to Al. These results seem to be confirmed by Palik [48, 49] given that ε_1 becomes negative at wavelengths greater than ~75 nm.

Obviously there are differences between the materials overall since Si does not function optically as a metal at much lower frequencies (visible, for example), but a material with metallic properties in the UV that can be easily patterned into high aspect-ratio nanostructures could prove useful in other applications. One key could be to make use of the higher loss of Si in this range, making it more ideal than Al for absorption applications. Si has been proposed as a possible polarizer material in the UV due to its interesting properties [51], but it does not mention Ref. [50] explicitly. We will see that another possible application could be an inverse polarizer architecture such as that in Ref. [6].

3.1.3 Metal-insulator-metal (MIM) waveguides

In the section above we discussed the optical properties of Si in the VUV and showed how they more closely approximate a metal than Au at these wavelengths. Since we propose to replace the Au structure utilized in space instrumentation and outlined in Ref. [3], it is important to understand the method of analysis used to describe waveguiding in Si nanograting structures.

A thin dielectric core surrounded by metal which can be approximated as semi-infinite (applicable here since light does not penetrate deep enough into Si at Ly-α to couple to neighboring slits) has been studied in various papers and is typically referred to as a metal-insulator-metal (MIM) or plasmonic/metallic "slot" waveguide [13, 52-55]. While other structures have been investigated for waveguiding capabilities, primarily the insulator-metal-insulator (IMI) structure [56], MIM structures offer the unique ability to confine propagating light into nanometer-scale cavities much smaller than the free-space wavelength, easily rivaling previous structures in terms of its ability to be integrated into applications such as chip-scale photonics.

Although they operate similarly to dielectric waveguides by guiding light due to refractive index differences between the core and cladding, MIM waveguides can support guided plasmonic modes along with traditional dielectric waveguide modes. Plasmonic modes also represent solutions to Maxwell's equations and exist at a single metal-dielectric interface. Derivations for plasmonic modes at a single metal-dielectric interface and MIM modes are shown in more detail in Appendix B, but some of the basic properties are discussed below.

Figure 3.5 shows electric field plots for plasmonic modes at a metal-dielectric interface as well as the two types of guided plasmonic modes in MIM waveguides which will be discussed below.

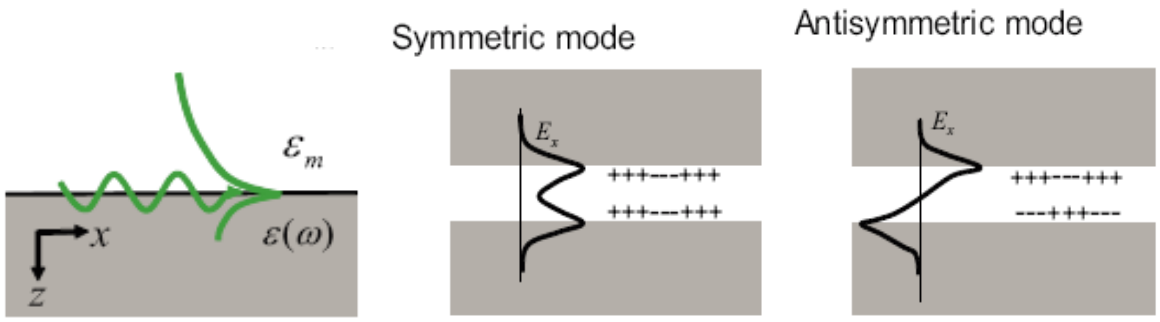

Figure 3.5 Electric field profiles of surface plasmon modes for a metal-dielectric interface (left) and a symmetric (center) and anti-symmetric (right) plasmon mode in a MIM waveguide [46].

As mentioned in 3.1.2, TM-polarized light (H-field in y-direction), if coupled correctly, can excite propagating surface modes coupled to electron oscillations. The field profile shown on the left represents a single-interface mode with electric field amplitudes decaying exponentially away from the surface. If unbounded by another metal surface, fields will penetrate much deeper into the dielectric region than the metal, limiting the confinement and ability to integrate into chip-scale applications. The other field profiles represent MIM waveguide modes which can be either symmetric (center) or antisymmetric (right). These can also be referred to as even and odd modes, respectively. Conventional waveguide modes are also attainable with TM-polarized light, but the core widths considered in this work are small enough that only plasmon modes will be discussed. Conventional waveguide modes also exist for TE-polarized light, becoming evanescent and effectively cut off when the core width is below $\lambda/2$. These modes will be included in the analysis of Si nanogratings because their propagation lengths are much longer than the TM-polarized modes, as will be presented.

The study in Ref. [13] provides a thorough analysis of SPP modes in MIM waveguide structures, but the primary focus of MIM waveguide works is to find structures which *increase* propagation length while we are attempting to effectively decrease propagation length of Ly-α. To begin, since absorption in a material is proportional to the imaginary part of the permittivity (ε_2), and we can see from Table 3.1 that Si has a ε_2 approximately 7 times that of Al at Ly-α, Si

could provide more loss to all conventional waveguide and SPP modes overall. Utilizing the equations outlined in Ref. [13] and Appendix B, the effective propagation constant (β) of TE and TM waveguide modes in an MIM structure can be easily calculated. The effective propagation length of a given mode can be calculated by: L = 1 / (2*Im(β)). Figures 3.6 and 3.7 show propagation lengths in nm for conventional TE waveguide modes and TM SPP modes, respectively, for two different trench widths.

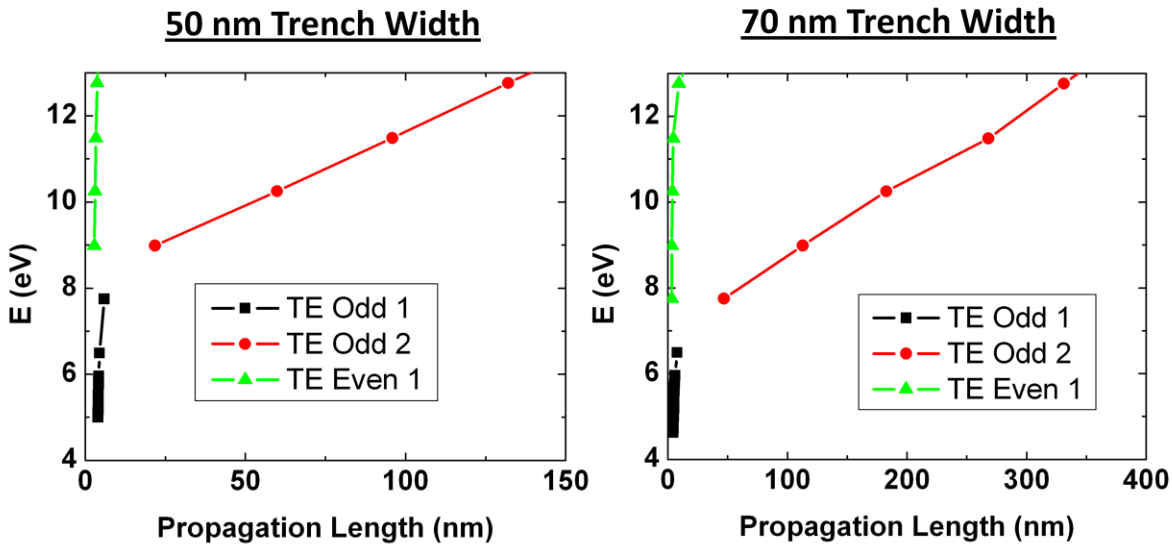

Figure 3.6 Propagation length (nm) vs. photon energy (eV) plots for Si-air-Si conventional waveguide modes given TE-polarized light with waveguide core width of 50 nm (left) and 70 nm (right). The length represents the point where the field has decayed to e^{-1} of its peak value. For each structure, two TE odd (antisymmetric) modes and one TE even (symmetric) mode exists in the plotted range (λ ~ 100-300 nm).

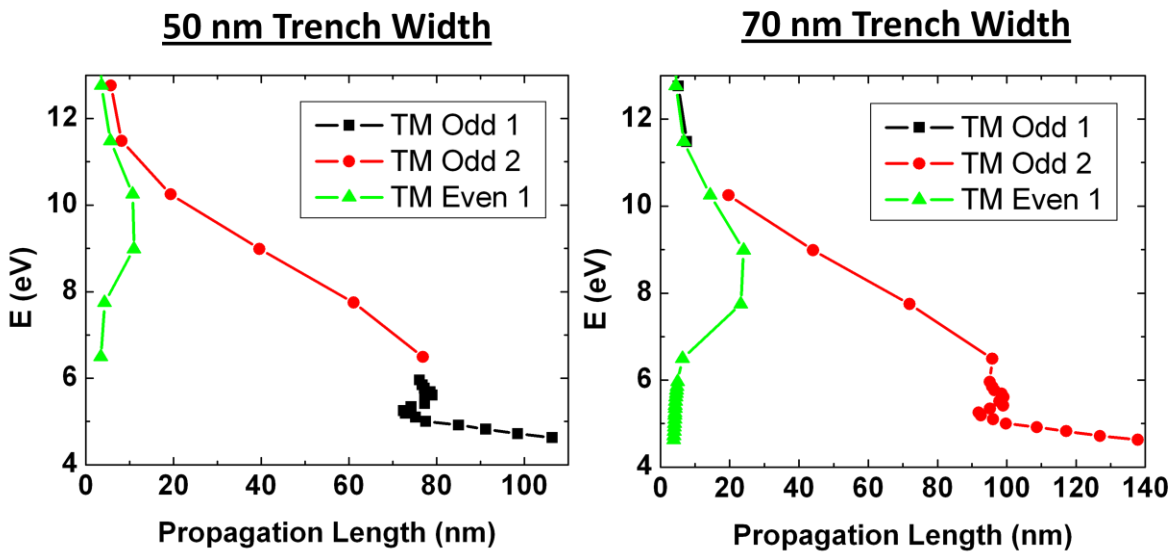

Figure 3.7 Propagation length (nm) vs. photon energy (eV) plots for Si-air-Si SPP waveguide modes given TM-polarized light with waveguide core width of 50 nm (left) and 70 nm (right). The length represents the point where the field has decayed to e^{-1} of its peak value. For each structure, two TM odd (antisymmetric) modes and one TM even (symmetric) mode exists in the plotted range (λ ~ 100-300 nm).

As expected from previous results, antisymmetric (odd) guided modes tend to have longer propagation lengths as compared to symmetric (even) modes. Furthermore, narrower trench widths cut off longer wavelength modes and lead to decreased propagation length at a given energy / wavelength. We can also notice that propagation lengths are typically much longer for TE waveguide modes as compared to TM SPP modes. This is particularly true at our target wavelength of 121 nm (~10 eV) where TM propagation lengths are on the order of 20 nm or less while TE modes reach nearly 200 nm for wider trench widths. By utilizing a lossy plasmonic material such as Si, the impressive propagation lengths discussed in Ref. [13] are not attainable, leaving the focus on reducing TE transmission. In order to reach desired transmission efficiency on the order $< 10^{-4}$, approximately 9-10 times the propagation length would be required. Given a propagation length of ~ 200 nm for a trench width of 70 nm, gratings of approximately 2 μm in depth should adequately block both polarizations, but variations in etching leading to wider trench widths are common and even deeper gratings would be required.

Au (which was used for the MENA structures [3] mentioned in 3.1.1) and other metals have even larger ε_2 values in this regime, but fields also penetrate deeper into the material as compared to Si or Al due to a refractive index of ~ 1 and lead to higher loss, effectively blocking

Ly-α for both polarizations of light. For example, TE and TM polarizations were both blocked for Au MENA gratings of only 400 nm of depth. Example field profile simulations from COMSOL are shown in Figure 3.8 to demonstrate the difference in propagation at Ly-α in equivalent Au and Si structures.

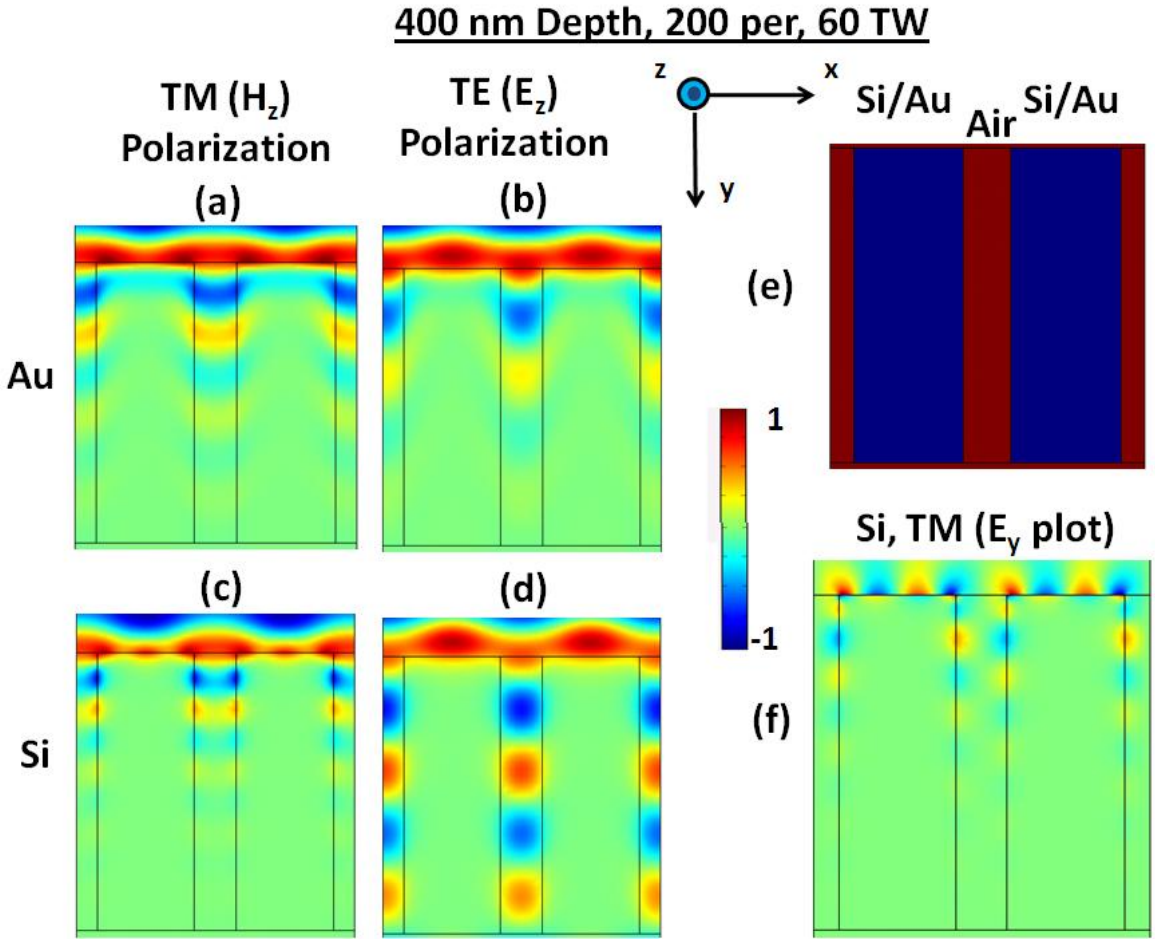

Figure 3.8 COMSOL field profile simulations for 400 nm thick, 200 nm period grating structures with 60 nm trench widths. Plots show the z-component of the field for (a)-(b) TM and TE polarizations for Au gratings and (c)-(d) TM and TE for Si gratings and (f) also shows the y-component of the electric field (E_y) for TM-polarized light on the Si grating, demonstrating a SPP mode. The index profile (e) shows the general structure of the gratings.

The figure shows simulations for Au and Si grating structures with equivalent dimensions (400 nm depth/thickness, 200 nm period, 60 nm trench width). Figure 3.8(a) and (c) show z-component of the magnetic field (H_z) for TM polarized light for Au and Si, respectively. Figure 3.8(b) and (d) show the z-component of the electric field (E_z) for TE polarized light. A diagram

showing the index profile of the structures is given in Figure 3.8(e). As mentioned above, it is clear to see that fields penetrate into the lossy Au grating material, and since the trench width is just below cutoff for Ly-α, both TE and TM modes decay exponentially along the grating depth.

Since the optical properties of Si are quite different at this wavelength, different modes propagate in the structure. For example, due to the metallic nature of Si, the TM-polarized mode is a SPP mode, leading to surface oscillations in the y-component of the electric field (E_y) along the propagation direction of the light. Figure 3.8(f) shows a plot of E_y under the same conditions as Figure 3.8(c), clearly demonstrating anti-symmetric E-field patterns which decay quickly along the grating depth. As described in Ref. [13], when the trench width becomes small enough, only the anti-symmetric SPP mode (also shown on the right in Figure 3.5) will propagate, but SPP modes tend to be more lossy, especially with a non-ideal plasmonic material such as Si. This shows that Si can surpass TM blocking as compared to Au grating structures with the same dimensions.

The TE mode in Figure 3.8(d) more closely resembles a typical guided mode in a parallel plate or MIM structure. While loss in the Si material still leads to field attenuation for SPP modes, the TE decay will not progress as quickly as Au due to the lack of field penetration into the cladding. Increasing the grating depth to increase the distance over which loss can occur would not be enough to compensate, so it is clear that trench widths would need to be decreased to a much smaller size as compared to the Au structure to ensure adequate cutoff and obtain TE transmission on the order of 10^{-4} or less.

As demonstrated in the etching results from Chapter 2, a uniform trench width of 50 nm or less over a 2 μm or greater depth was not achieved due to so-called “bowing” caused by mask erosion during the etch process. While metal masks could be used to combat this issue, trench width variation may not be eliminated completely. Furthermore, reduction in trench width will also lead to reduced particle transmission to unacceptable levels for measurement. Finally, due to the non-metallic nature of Si at visible wavelengths, lower energy photons can still pass through the structure and cause some noise for particle measurements as well.

An ideal grating structure would be able to achieve similar UV attenuation to MENA despite some processing variation while using a stronger grating material, but more open area for particle transmission and visible attenuation are also desirable.

3.2 Proposed structure

To achieve the goals listed above, it will be shown that atomic layer deposition (ALD), also known as atomic layer epitaxy (ALE), can be used to coat finished grating structures and achieve impressive attenuation. Good overviews of relevant process information can be found in Ref. [57-59], but the basic premise involves a cycling, two-step process similar to that discussed in DRIE in Chapter 2. While similar to a standard chemical vapor deposition process in which gases are flowed to induce surface reactions and material growth, ALD has two precursor materials that are used in alternating steps in order to create a self-limiting reaction and control of the layer thickness on the atomic monolayer level, ~0.1 Å. While this processing technique has already found a home in the semiconductor industry for applications such as gate dielectrics of transistors and trench capacitors, exciting new research is progressing and leading to new materials that can be deposited with this processing technique [58, 59]. Due to the decreasing cost and new materials being developed, ALD has only recently been investigated for optics applications. We will show below that ALD materials such as Al_2O_3 and Pt can be used to coat fabricated Si nanogratings to greatly increase UV attenuation, and even visible attenuation in the case of Pt.

The improvement in attenuation can once again be understood by a kind of reverse design methodology similar to that used above for MIM waveguides. In Ref. [13], designs are demonstrated in order to investigate the *increase* of propagation length for guided modes. More recent works [60-62] have analyzed how plasmonic MIM modes are altered through the use of a graded or multi-dielectric core in order to increase propagation, often referred to as metal-multi-insulator-metal (MMIM) waveguides. A figure from Ref. [60] is reproduced below to demonstrate a MMIM architecture.

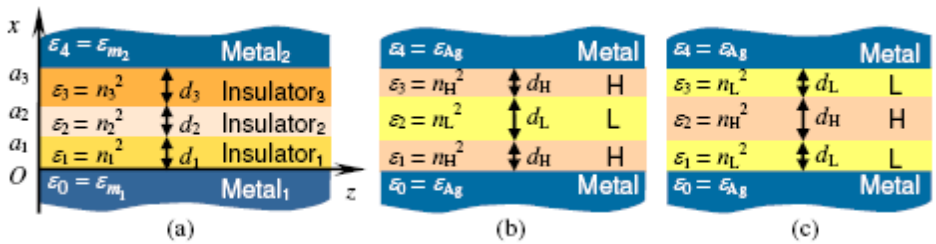

Figure 3.9 Figure from Ref. [60] showing a MMIM waveguide schematic. Two types of architectures were investigated, a high-low-high index (b) and a low-high-low index (c), which refer to the relative refractive indices of the materials used.

The figure shows a general diagram of a three-insulator design in 3.9(a). Referring to the relative refractive indices of the core materials, Figures 3.9(b) and (c) show a high-low-high index (MHLHM) and low-high-low index (MLHLM) schematic, respectively. The paper focuses particularly on the improved propagation lengths of MLHLM structures when compared with MIM waveguides with low index cores, proving that the loss of the anti-symmetric mode can be reduced. This is primarily due to the change in field confinement and localization in the structure, with more of the field being localized in the high index center of the core and less interaction with the metal leading to lower loss and longer propagation. As expected, traditional waveguide theory still applies in the small cavities, so LHL core essentially acts as an additional waveguiding element in the overall structure. It can be shown later in Chapter 5 that similar principles can be used to create transmission color filters with varying bandwidth by affecting field confinement.

Therefore, to *decrease* the propagation length in our structure, we investigated coating a free-standing Si grating with an ALD layer of a material such as Al_2O_3 or Pt to increase loss in our structure. By looking at the refractive indices of Al_2O_3 and Pt in Table 3.1, we can see that a MHLHM structure will be formed since $n_{ALD} > n_{vacuum}$, leading to an increased confinement of the field in the higher index regions near the metal cladding instead of in the center with the MLHLM structure mentioned above for both TE and TM polarizations. For TE waves, the alteration of the waveguide modes can lead to an increased attenuation, but as demonstrated in Ref. [60], low-loss, high-index materials could actually increase the propagation length of the TM anti-symmetric mode for very thin layers. COMSOL simulations showing gratings with the same dimensions as those simulated in Figure 3.8 are shown below.

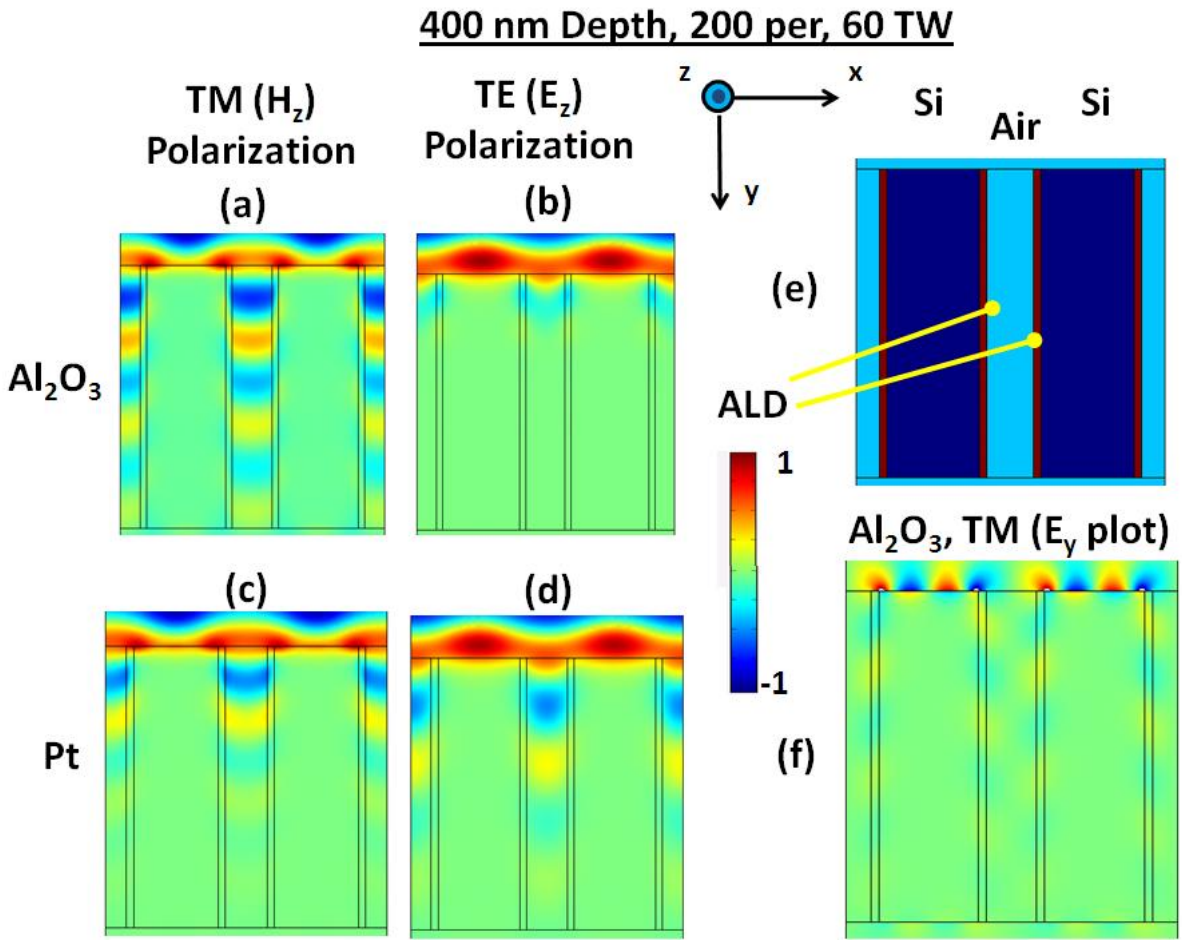

Figure 3.10 COMSOL field profile simulations for 400 nm thick, 200 nm period gratings with 60 nm trench widths and 10 nm ALD coatings. Plots show the z-component of the field for (a)-(b) TM and TE polarizations for Al_2O_3-coated gratings and (c)-(d) TM and TE for Pt-coated gratings and (f) also shows the y-component of the electric field (E_y) for TM-polarized light on the Al_2O_3-coated grating, demonstrating a SPP mode. The index profile (e) shows a general ALD-coated grating structure.

Figure 3.10 shows field profile simulations for TE and TM polarization in ALD-coated (10 nm of Al_2O_3 or Pt) Si gratings at Ly-α. We can see that absorption of TE modes has increased for both ALD materials when compared with the Si gratings with the same dimensions (400 nm depth, 200 nm period, 60 nm trench width) from Figure 3.8. We also notice that while the absorption loss, related to ε_2, for both of these materials used in ALD coatings will be quite high (Table 3.1), that the TM anti-symmetric mode still has a slightly increased propagation length when compared with a standard Si grating, as predicted in Ref. [60], particularly for the higher index Al_2O_3 coating. While an increase the grating depth to approximately 2.5 μm (the

same as our fabricated structures), could increase the attenuation distance enough to remove the TM component for both structures, thicker ALD coatings could be more effective as well.

Given the simulation results above, Pt-coated gratings of larger depth (~2.5 μm) should provide efficient blocking of both TE and TM polarized light. These gratings also have the added advantage of blocking visible light (as will be shown below), leading to even lower noise reaching a particle detector.

3.3 Fabrication

Utilizing the improvements in Si etching and fabrication presented in Chapter 2, new Si gratings were attempted with device layer depths primarily of 2.5 μm and 4.5 μm, following NIL-based fabrication procedures outlined in Section 2.2.2 and Figure 2.11. Gratings with a 220 nm period and trench widths of approximately 75 nm (with some bowing) could be fabricated to test UV and particle transmission. As outlined above, since Si gratings alone could not achieve high enough extinction of incoming UV light due to the metallic nature of the material at 121 nm, two types of ALD coatings were added to finished gratings to achieve sufficient blocking (Figure 3.11).

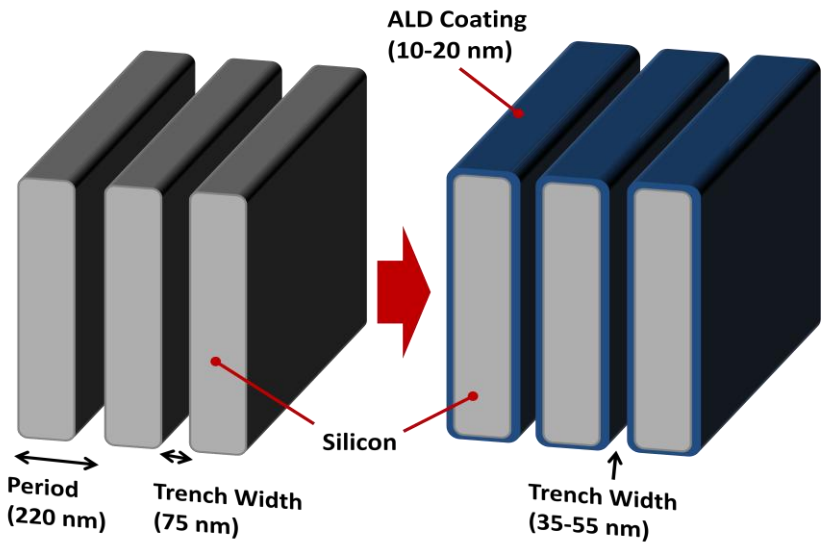

Figure 3.11 Diagram showing proposed Si grating (left) and ALD-coated structure (right) with typical dimensions.

Al_2O_3 was coated on gratings of both 2.5 μm and 4.5 μm depths, with thicknesses from 10 nm up to 20 nm for the shallower gratings and only 10 nm for the deeper structure. Depositions were performed onsite using an Oxford OpAL ALD tool. Under the assumption that Al_2O_3 acts as a high-index, lossy dielectric, the typical waveguide mode pattern should be altered due not only to decreasing trench width well below a value of $\lambda/2$ (~35 nm trench width at the top, in the case of 20 nm ALD), but also incorporating a non-ideal cladding medium to increase confinement in a lossy material during propagation. Contacts at the National Institute of Standards and Technology (NIST) performed Pt ALD on 2.5 μm depth gratings using an Oxford FlexAL run at 300 °C using a process / precursors similar to Ref. [59], depositing approximately 10 nm or 20 nm of Pt on the structure. As mentioned above, due to the lower plasmon frequency of Pt, like the Au used in MENA, it also acts as a lossy medium with a slightly higher index of refraction than air (shown in Table 3.1). Unlike the Al_2O_3 coatings, Pt-coated structures could provide an added bonus of being relatively opaque at visible frequencies as well, effectively blocking further noise caused by visible solar emission.

3.4 Testing Procedure

Gratings were tested for light transmission using two different tools. The first involved simple spectral transmission testing similar to that conducted in Ref. [4] over the range from approximately 190 nm and into the visible region (up to ~ 750 nm) using a Woollam M-2000 Ellipsometer. While the data produced requires more complex analysis than the MIM waveguide theory given above to explain visible light propagation, with explanations of grating diffraction and plasmonic resonances necessary, these measurements provided good confirmation of the impressive UV blocking capability of the fabricated structures and also give a possible quantity for defective areas present. Furthermore, these measurements were able to demonstrate the effect of the gratings on TE and TM polarized light, which is not possible in our second measurement scheme. Finally, the Pt-coated ALD structure needs to be tested for visible light transmission as well to determine if it can further reduce noise for the particle detectors.

The second measurement scheme was developed utilizing a H_2 microwave discharge lamp which emits a strong output at the Ly-α wavelength, described in Ref. [63]. Since we are now measuring transmission at vacuum UV (VUV) wavelengths, a vacuum chamber is required

to remove air which can absorb VUV emission from the lamp. A general diagram and images of the setup are given below in Figure 3.12.

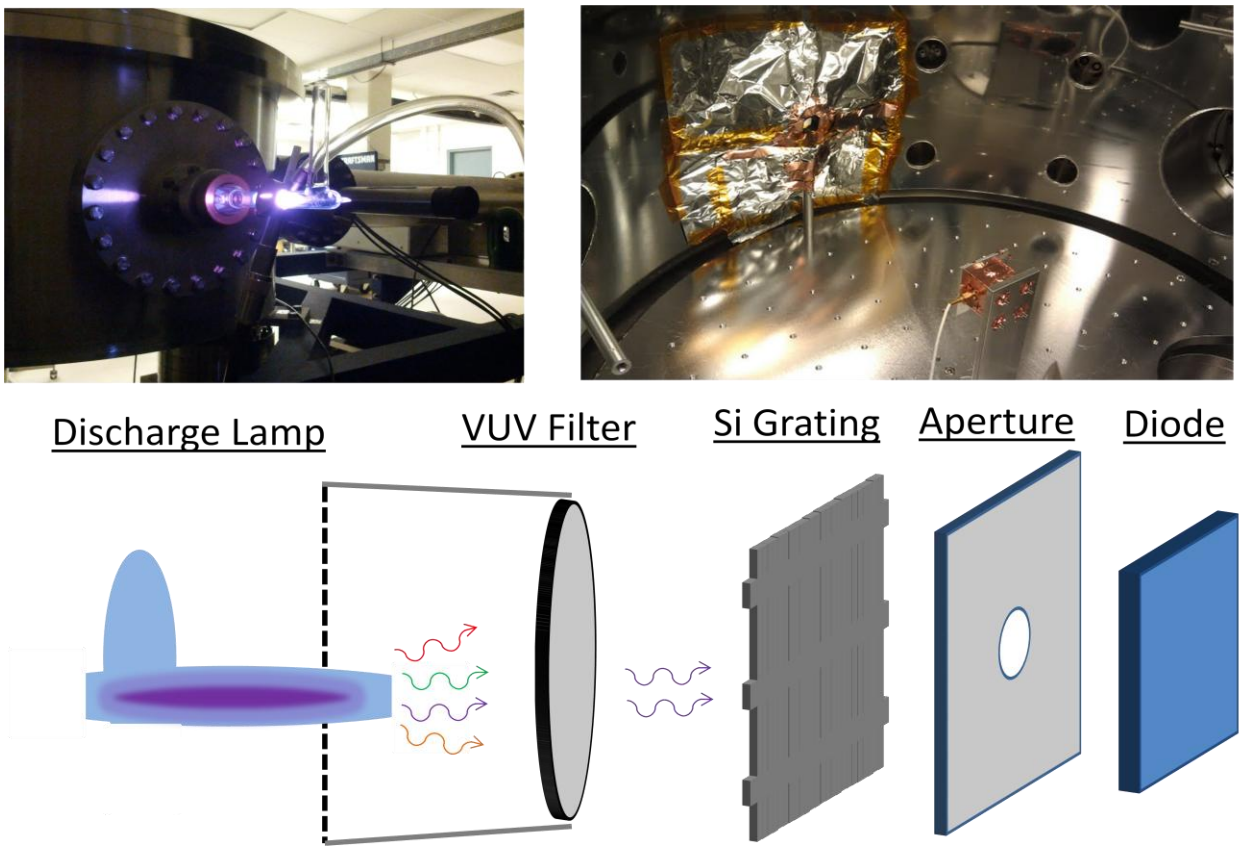

Figure 3.12 Diagram of VUV transmission setup (bottom) and pictures of lamp and test chamber (top). The output of the discharge lamp first passes through a filter with peak transmission at Ly-α (encased in foil to prevent light leakage), then through the Si grating structure which is attached to an aperture plate on top of the photodiode.

As illustrated in Figure 3.12 both in the discharge lamp picture (top left) and schematic (bottom left), since an argon plasma is used to generate the Ly-α output, visible light is also output by the lamp into the chamber. While visible light could possibly be allowed in the grating design, the photodetector utilized (AXUV-100G, International Radiation Detectors, NIST calibrated) will not distinguish between light passing through the gratings of any wavelength, showing a relatively high responsivity across the entire visible range. To combat this issue, first, a filter was introduced into the setup (Pelham Optics 122FNB VUV Narrowband Optical Filter) that passes approximately 15% of VUV centered around 122 nm with a full-width at half maximum of just 20 nm, effectively blocking out visible light on the order of 10^3-10^4 greater than the Ly-α. Light

then passes through a Si grating sample attached to a plate with a machined circular aperture (varied from 1-3 mm in diameter) which can then be fitted over the photodiode. This aperture also allows us to select areas of the grating with fewer visible defects. With this setup, the ratio of the currents from the photodetector with and without the Si grating can provide relative transmittance data.

Due to the strength of the source, visible light could still be seen through the filter (although greatly attenuated), so a further precaution was taken to attempt to verify that measured results were mostly due to UV transmission. For each of the gratings tested, transmission measurements were taken on the grating alone as well as with a piece of fused silica (SiO_2) between the grating and the aperture. Reference measurements with an open aperture and fused silica-covered aperture were also taken. Fused silica of sufficient thickness is known to effectively reflect or absorb all UV light in this range. This way the measurements with and without fused silica could be compared with each other to determine the fraction of grating transmission that is due to visible light alone (with the silica) as opposed to the light exiting the VUV filter (without the silica), which still contains a small visible component (not shown in Figure 3.12).

The results from both transmission measurements are presented and discussed in the following section.

3.5 Results and discussion

Some images from final fabricated structures are shown below in Figures 3.13 and 3.14.

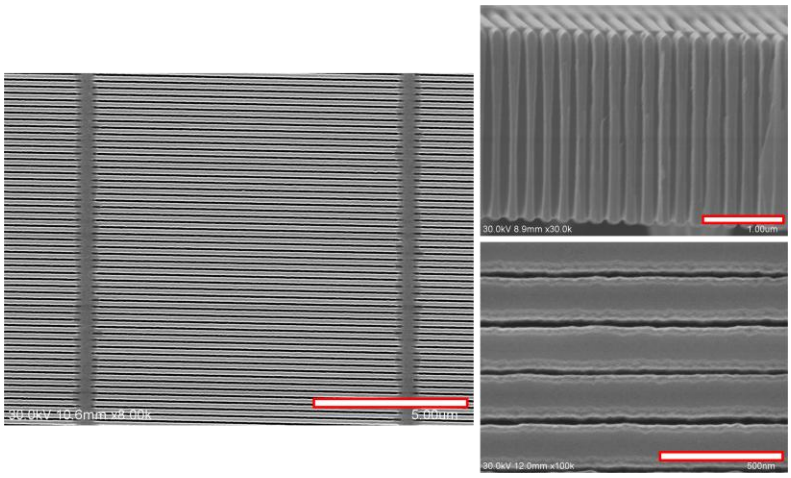

Figure 3.13 SEM images show the (left) top view of a fabricated 2.5 μm depth grating, (top right) side view of a fabricated 2.5 μm depth grating, (bottom right) top view of a grating coated with ~20 nm of ALD Al_2O_3, scale bars show 5 μm, 1 μm, and 500 nm, respectively.

Figure 3.13 shows images of a fabricated 2.5 μm depth grating with top trench widths of approximately 75 nm and a period of 220 nm. However, the image on the top right clearly shows line width reduction as the etch progresses deeper (bowing). This bowing is taken into account in later simulations and effectively acts to increase the core width of our waveguides, causing increased transmission, particularly of TE polarization, as demonstrated in Figure 3.6. The image on the bottom right shows a top view of a grating after ~20 nm of Al_2O_3 is deposited using ALD, effectively closing the gap to approximately 35 nm, but trench widths are still larger as the grating gets deeper. ALD coatings become extremely important not only to reduce trench width at the top, but to coat the sidewalls with a less conductive material, increasing attenuation of UV. This can effectively increase loss enough to compensate for the bowing of the Si grating.

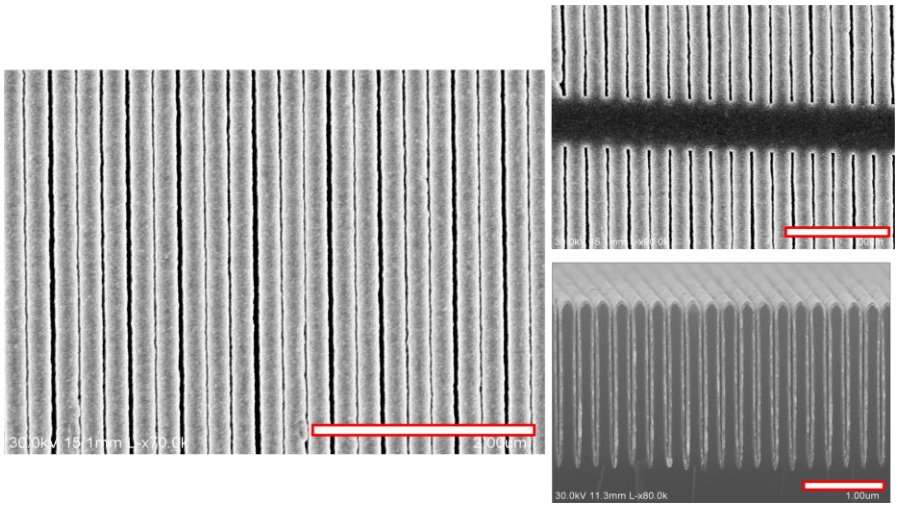

Figure 3.14 SEM images show the (left) top view of 2.5 μm depth grating coated with ~20 nm of ALD Pt away from support, (top right) top view showing grating openings near support bar, (bottom right) side view of a separate fabricated structure demonstrating Pt deposition along the entire length of the trenches, scale bars show 2 μm, 1 μm, and 1 μm, respectively.

Figure 3.14 shows images from structures coated with Pt using ALD. Unlike the Al_2O_3 coated structure, this grating may have been mishandled, causing the grating lines to stick together, as shown in the image on the left. Since the largest top trench width is still around 50 nm, this should not greatly affect UV transmission, but it will actually reduce visible transmission since periodic, metallic gratings of this period tend to show transmission bands in the visible. The image on the top right shows little sticking since it is near a support bar and shows trench width reduction down to ~35 nm. The image on the bottom right shows deposition on a separate structure fabricated on a Si wafer to demonstrate that the Pt ALD coating penetrates entirely into the trenches, coating the entire structure.

Results showing transmission measurements from the spectroscopic ellipsometer are presented in Figure 3.15.

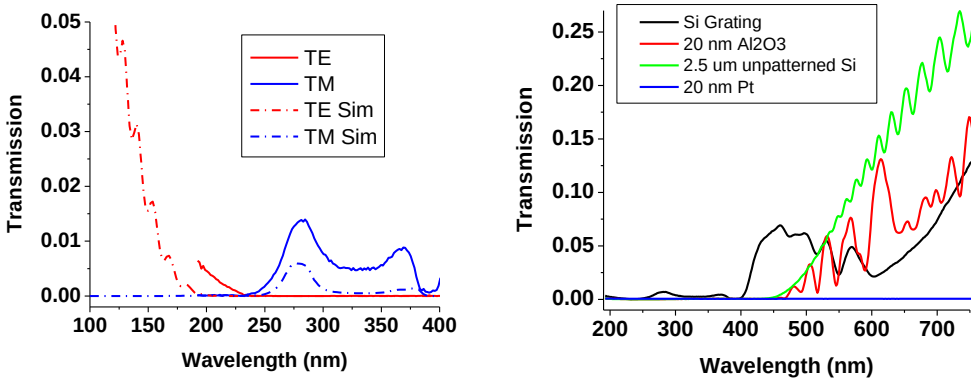

Figure 3.15 UV/visible transmission measurements taken from spectroscopic ellipsometer showing (left) difference between TE and TM transmission (data/simulation) through a 2.5 μm depth Si grating and (right) UV and visible transmission for Si grating, Al_2O_3 ALD, and Pt ALD structures along with simulation of unpatterned, 2.5 μm depth Si layer (green)

The data serves to highlight a few important points. The graph on the left shows the difference between TE and TM UV transmission for both data and simulation for the 2.5 μm depth Si grating shown in Figure 3.13 (no ALD coating). Data can only be taken down to ~190 nm, but both data and simulation clearly show TE transmission increasing as wavelengths decrease toward the VUV, approaching the cutoff point for the normal TE waveguide modes of the MIM structure when the trench width is closer to $\lambda/2$. The TM data and simulation shows, as expected, that TM light is effectively blocked or absorbed by the grating once the light starts coupling to the SPP TM modes. The graph also shows slight transmission peaks at nearly identical locations for the data and simulation, but the data shows a higher magnitude for both TE and TM. While a portion of this could be due to slight material differences, it will be shown later that all of the gratings have defects present which could account for approximately 0.01-0.1% transmission in certain areas.

The data on the right serves primarily to highlight the visible transmission of the tested structures relative to the UV. As presented here and discussed later, certain Si samples transmit much more at visible wavelengths than others. While detailed analysis of the variety of resonances in these curves is outside the scope of this thesis, we will later see that variations between the signals recorded in our second transmission measurement method could be due to varying visible transmission of the samples, limiting the accuracy of the collected data. It is also important the notice that none of the slight peaks in the UV seen for the Si grating are present for

any of the other samples, demonstrating that ALD-coated structures greatly increase the loss in the UV range. We can also see that the Pt-coated grating curve has approximately 0% across the entire range, as expected.

Measurements using the second measurement method are now presented in order to provide a first attempt at measuring Ly-α transmission for Si gratings. However, due to the alterations in the setup above, this data can only provide an approximation to the effect of Si gratings and ALD-coated gratings on Ly-α attenuation. For one, an accurate spectrograph has not been produced for the source to determine the ratio between Ly-α and the visible light generated by the plasma. We attempted to compensate for this with the added filter and fused silica measurements, but error can still be introduced into the process since some light (including visible) can be reflected off of the fused silica surface and cause variation in the expected results. To attempt to compensate for this, transmission measurements were not simply taken as a simple ratio, but a multiplicative factor was added to account for approximately 5% of visible light that might be reflected (Fresnel reflection) during the fused silica (FS) measurement. This factor was obtained to create near-zero transmission for the data taken from an unpatterned, 2.5 μm thick, free-standing Si layer which was measured as well. If our measurement method is actually accurate to determine Ly-α transmission, then 0% Ly-α should transmit through the Si layer since we are sure that no defects are present. The equation for calculating the transmission ratio based off of the currents measuring from the photodiode becomes:

$$Transmission = \frac{Nanograting - 1.0588 * Nanograting(FS)}{Open\ Aperture - 1.0588 * Open\ Aperture(FS)}$$

This is obviously not an ideal way to collect accurate data and a vacuum monochromator measurement similar to that performed for the MENA tests would be much more accurate to determine Ly-α transmission, but interesting properties about the gratings such as defect density and the effects of ALD coating can still be gathered from the data, as well as a determination of whether the gratings can effectively attenuate Ly-α.

Calculated transmission ratios for various gratings are presented below in Figure 3.16.

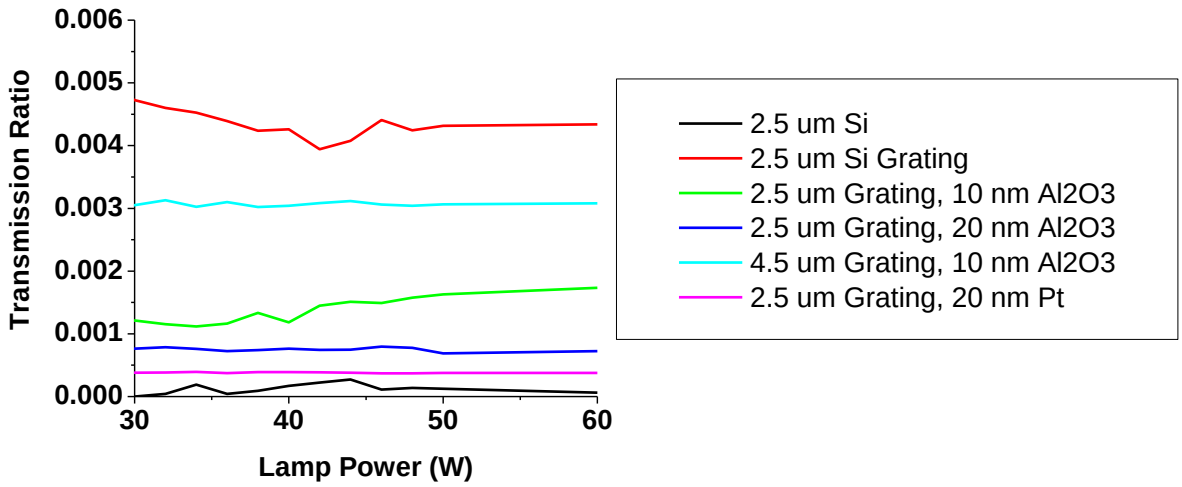

Figure 3.16 Transmission ratios for various grating samples using vacuum chamber measurement method.

The data in Figure 3.16 shows the transmission ratio for the fabricated gratings (in addition to the unpatterned, 2.5 μm thick, free-standing Si layer) calculated using the equation above for various powers supplied to the H_2 discharge lamp. Changing the power mainly serves to determine whether our method takes into account any variation in the lamp intensity or ratio of UV to visible that might occur with changing power. Little variation in the transmission intensity with the lamp power seems to be shown. We can clearly see from the data that measurements cannot be taken as absolutes since the transmission through the solid Si layer is not zero. The multiplicative factor would need to change for each lamp power and this is not accurate.

Given that there can be some variation in our measurement method, the data still progresses as would be expected. For example, the next lowest transmission is given by the Pt ALD-coated grating, which provided the best UV blocking ability in our simulations. It should be noted, however, that this measurement was taken at a point on the grating with the least visible defects. While we want to avoid defects that can ruin our measurements, if our method was accurate, we would still be able to account for defective areas. Figure 3.17 shows three measurements at 3 different points on the Pt-coated grating where there were varying amounts of defects. It obviously shows that a defect plugging method would be need to achieve adequate Ly-α blocking for space probe applications.

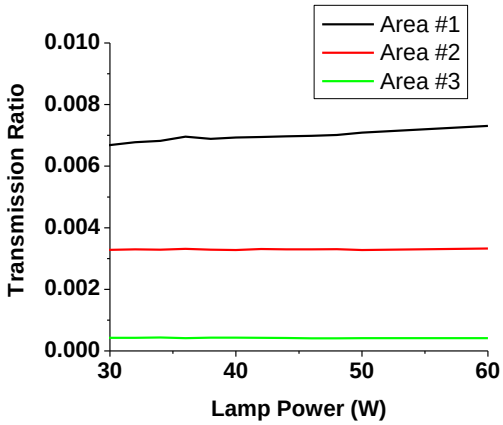

Figure 3.17 Transmission ratio data for 3 different areas on the same Pt ALD-coated grating demonstrating the range of defects on the sample.

Despite trying to find an area with the least defects, it is possible that the lowest values (~10^{-4}) taken at area #3 are representative of defects in the nanoimprinting mask on the micro or nano-scale which could still allow light to pass through, but wouldn't be visible to the eye.

Looking back at the data in Figure 3.16, we see that the next highest transmission ratio is for the 20 nm Al_2O_3-coated grating. While it is most likely that visible light is still affecting these measurements, we would expect that Al_2O_3 would not be as effective at blocking Ly-α and that thinner layers would also be less effective, as confirmed above. The 4.5 μm deep Al_2O_3-coated grating provides a good example for how bowing can affect transmission. Despite having the same thickness as the 2.5 μm grating and a much longer distance for propagation loss, bowing can reduce Si line width well below 100 nm for deep structures (as shown in the ultra high aspect-ratio trench etch results in Chapter 2). This increase in trench width coupled with the possible increase in TM propagation in Al_2O_3 MHLHM structures is the most likely reason for the increase transmission. Finally, the standard 2.5 μm grating shows the highest transmission. Unfortunately, we cannot tell from the measurements whether TM-polarized light is more effectively blocked than TE, but the simulations and data in Figure 3.15 seem to confirm that this relationship should still hold. Assuming TM transmission is 0% and that the measurement method is accurate, this would give TE transmission on the order of 1% for an uncoated grating, far above what it would need to be for an adequate rejection ratio.

3.6 Conclusion

The work presented above provides new analysis and the first data taken at Ly-α collected on Si nanogratings for use as UV absorbers in particle detection instruments. Although Au gratings were used in past instrumentation, Si was proposed as a material with the possibility for a stronger device with an easier method for large area fabrication, but Si has more metallic optical properties than Au in the VUV. It was seen that Si gratings could still provide high UV blocking while possibly allowing for greater particle flux, but new analysis methods relying on MIM waveguide theory were needed to create an optimum structure. By realizing that TM-polarized light was coupling to lossy SPP modes while TE-polarized light was coupling to waveguide modes, trench widths much less than $\lambda/2$ (< 60 nm) would be required to achieve similar UV blocking to Au.

Since these structures would not only be difficult to fabricate but would also lead to lower particle flux, ALD coatings were proposed to increase loss while allowing wider trench widths. Pt ALD coatings would also be able to provide blocking of visible light to make more ideal detectors. Samples were fabricated using processes outlined in Chapter 2 and Al_2O_3 or Pt ALD coatings were added. While non-idealities in the fabrication and measurement process led to some variation between data and simulations, it was still shown that free-standing Si nanogratings could provide a robust, large-area UV filter that could achieve higher UV rejection with larger open area for particle transmission. This work also demonstrates a use for Si as a material with metallic optical properties in the VUV, hopefully leading to further research into nanostructured Si for VUV manipulation.

Chapter 4

Plasmonic color filters fabricated by multilayer transfer lithography

4.1 Introduction

4.1.1 Metal-insulator-metal nanostructures

Metal-insulator-metal (MIM) structures have been used in a wide range of fields ranging from metamaterials [24, 64] to plasmonic devices [65] to color filters [66, 67]. Out of these fields, color filter technology has been a widely sought after application since it can be applied to large markets in displays, CMOS image sensors, or light emitting diodes, among others. Most of these devices currently use patterned dyes which absorb complementary colors and pass red, green, and blue (RGB) transmission filters, utilizing sources built into the product to project light through the filters into the eye. Scientists have steadily researched thin film alternatives to current color filter technology in hopes of reducing the cost or complexity of the fabrication process, improving performance through better spectral control or smaller pixel sizes, reducing the amount of "wasted light" absorbed by traditional filters, or reducing the chemical waste inherent in other patterning processes.

For color filter applications such as [66], frequencies are chosen to couple specific modes in and out of the device through tailoring of the input and output slit. While this device could effectively create the RGB colors required for typical applications, the overall transmission was still very low and the design did not lend itself to traditional color filter architectures. Ref. [67] displays a much more viable method for manufacturing color filters and was actually done using a very similar method to what I presented in Ref. [17] and will outline below.

In previous work, a plasmonic MIM grating structure was fabricated using focused ion beam lithography to create red, green, and blue (RGB) pixels higher transmission intensities and sharper resonances than previous reported works [68] for use in display technology. In this structure the top metal grating coupled transverse magnetic (TM) light (electric field

perpendicular to the grating) of a specific frequency band, which could be defined by the period of the grating, into the plasmonic waveguide while the bottom grating (ideally with an identical structure) coupled the light out to the far field.

In Ref. [17], we proposed a similar structure to be utilized for reflective display technology. Instead of passing certain frequency bands for transmission, these same bands could be targeted for absorption, creating a complementary color spectrum for reflective color (Cyan, Magenta, Yellow (CMY instead of RGB)) by using a MIM lossy waveguide structure. Reflective technology is advantageous for flexible displays. Here, a fabrication method is needed to process on flexible substrates and over large areas, unlike our previously reported MIM transmission filters which were made on hard substrates using focused ion beam patterning.

4.1.2 Fabry Perot filters with minimal angle dependence

While many of the above proposed structures have achieved impressive color filtering capabilities, a key feature which inhibits many devices is angular dependence [69-71]. For most of the applications above, wide viewing angles are required in order for the device to function properly. In previous work that is currently under review [72] and more recently published work [73], a design related to a Fabry-Perot etalon was presented in order to demonstrate the lack of angle dependence of certain MIM filters due to the dielectric insulator material.

A Fabry-Perot interferometer or etalon is a common tool used in telecommunications, lasers, and spectroscopy, consisting of two partially transmitting mirrors at the end of a cavity. As light propagates between the mirrors, interference between the reflected waves leads to filtering. Constructively interfering, in-phase waves lead to a high transmission peak while destructive, out-of-phase waves lead to a minimum. The phase difference between succeeding reflecting waves is given by $\delta = (2\pi/\lambda)2nd\cos\theta_2$, where λ is the wavelength, n is the index of the cavity, d is the cavity length, and θ_2 is the angle after transmission through the first mirror. The transmission of the structure can be solved for if one knows the reflectance of the two mirrors. If both surfaces have a reflectance of R, the overall transmission is given by $T = \frac{(1-R)^2}{1+R^2-2R\cos\delta}$.

This concept was applied to color filtering in Ref. [14]. The basic structure does not necessarily require any patterning. A thin Ag film can be deposited on a clean glass substrate, followed by dielectric layers of chosen thicknesses to define a specific cavity length / color, and finished with another thin Ag film. While a great deal of the filter's performance depends on the

material quality, particularly the roughness of the thin Ag film, the relative ease of fabricating this structure makes it valuable. Additionally, the majority of the non-transmitted light is reflected and can therefore be recycled by a back reflector since it is not absorbed in the structure.

Using this previous work, new Fabry-Perot filter devices were fabricated and investigated for angular tolerance [72]. While Ref. [14, 73] utilize the transmission structure, Figure 4.1 shows a general schematic of a different design which can be used as a reflective color filter. The bottom Ag layer is made much thicker than the top layer in order to reflect all light. Instead of transmitting a specific band of frequencies, this structure will absorb that band and reflect all other frequencies, creating CMY colors.

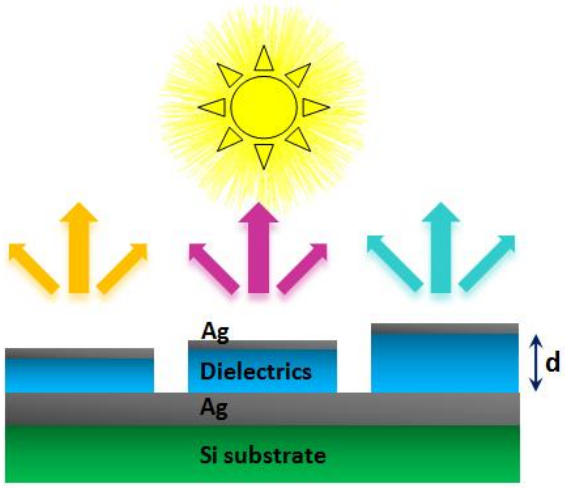

Figure 4.1 Rendition of reflection Fabry-Perot filters with varying thicknesses to create yellow, magenta, and cyan colors.

Previous work regarding the transmission filter [14] used SiO_2 as a dielectric layer to achieve RGB colors. This structure was proven to have very little variation in color when the viewing angle was changed from 0° to 12°, but after this point, color selectivity degraded. In Figure 4.2, COMSOL simulations were run for varying SiO_2 thicknesses to achieve RGB spectra using the transmission filter design (left) and CMY spectra for the reflection filter design (right). The proposed thicknesses varied from 100-170 nm of SiO_2 for the resonator dielectric (not the cladding layer, which is always assumed to be 100 nm thick). Similar spectra could be obtained for other dielectric materials (Si_3N_4, ZnSe) with thinner layers needed for higher refractive indices. Like Ref. [14], we found a tradeoff between bandwidth and overall transmission with

varying Ag film thickness, also depending on parameters used for simulation. ~20 nm of Ag was used in our simulations.

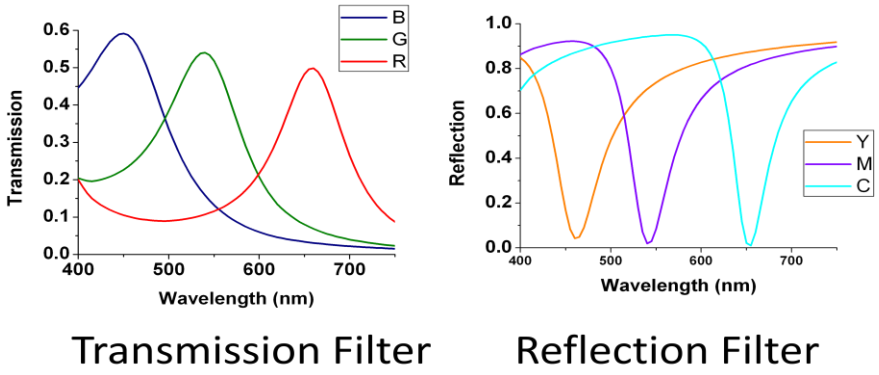

Figure 4.2 Simulated spectra with varying SiO_2 for the resonator dielectric layer in transmission (left) and reflection (right) structure. B/Y was obtained with 100 nm of SiO_2, G/M with 130 nm, and R/C with 170 nm.

To address the problem of incident angle / color variation, dielectric materials with varying refractive indices were investigated using the reflective filter geometry although, as demonstrated in Ref. [73], similar principles are applicable to the transmission structure. In the initial equation for the phase difference between succeeding reflected waves ($\delta = (2\pi/\lambda)2nd\cos\theta_2$), the angle θ_2 represents the angle within the resonator cavity, after transmission through the top, semi-transparent mirror. According to the equation, when the angle shifts to larger values, the transmission wavelength (λ) will blue shift, causing color variation. This angle can be easily determined using Snell's law $\sin\theta_1 = n\sin\theta_2$ (see Figure 4.4(a)), given the index of refraction of the resonator cavity layer (n) and the incident angle (θ_1) of light (assuming air as the external medium, for now). With increasing θ_1, a larger n can be used to keep θ_2 small despite the larger θ_1, reducing the amount of blue shift and angular dependence. This is shown in angle-varied COMSOL simulations in Figure 4.3 for reflection devices, using three materials: SiO_2 (n~1.45), Si_3N_4 (n~2.0) and ZnSe (n~2.6).

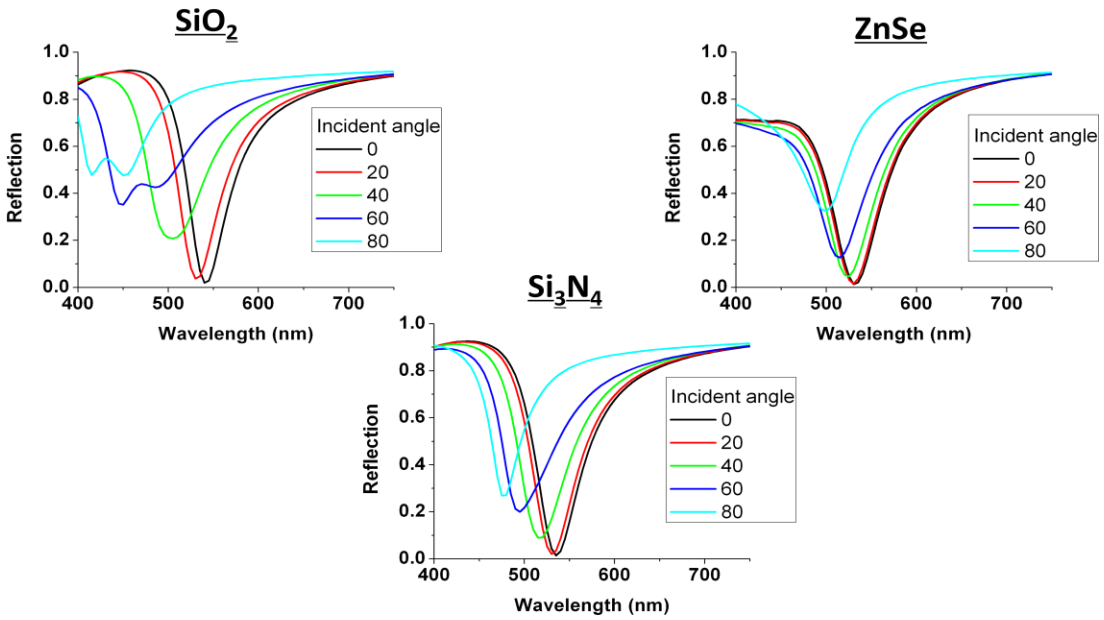

Figure 4.3 Simulated reflection spectra with varying incident angle (0° to 80°) for magenta color filters with 3 different resonator layer dielectric materials: SiO_2 (n~1.45), Si_3N_4 (n~2.0), ZnSe (n~2.6).

From these results we can confirm that dielectric materials with higher refractive indices greatly reduce the angular dependence of the color filter. Transmission and reflection filters using SiO_2 as the dielectric can shift over 100 nm in peak wavelength when varying from 0° to 80° while using ZnSe leads to a shift of approximately 30 nm. Using these simulations, devices were fabricated to demonstrate all 3 reflection colors and angle dependence with different dielectric materials. Fabrication of these devices was very simple as long as one has a good degree of control over layer thickness. Ag layers were deposited using e-beam evaporation on top of a thin (1-2 nm) Ge layer, which is used to improve film quality. Dielectric layers were deposited using either plasma enhanced chemical vapor deposition (PECVD) or e-beam evaporation. Reflection measurements were taken using a Filmetrics F20 for normal incidence while a Woollam variable-angle spectroscopic ellipsometer (WVASE32) was used for angled reflection measurements. Figure 4.4 provides a summary of the results.

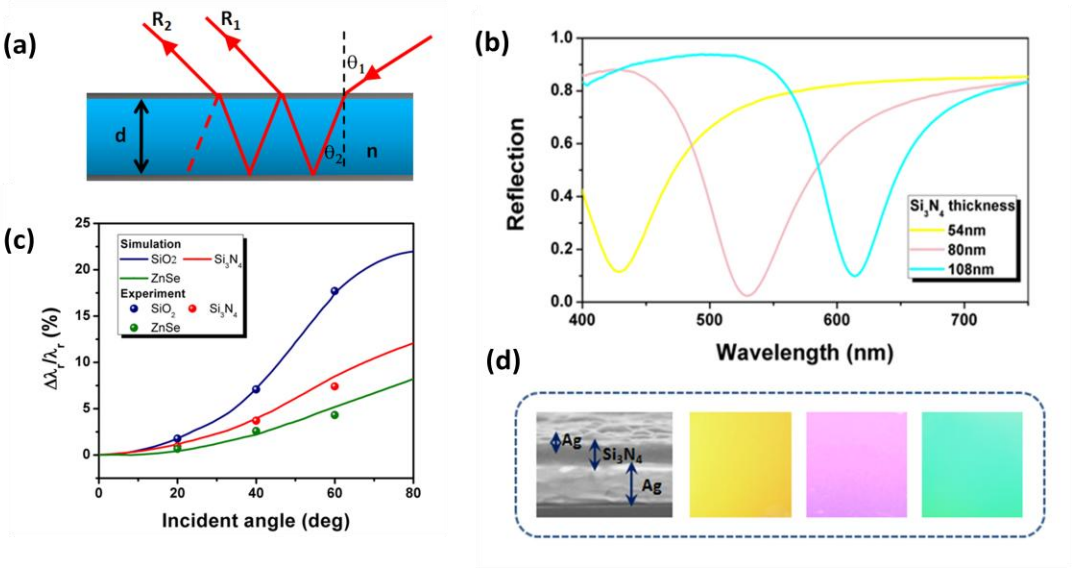

Figure 4.4 Summary of results from Fabry-Perot reflective filters showing (a) diagram showing general operation of reflective filter (b) reflection data taken from reflective filters with varying Si_3N_4 thicknesses showing CMY spectra (c) data showing the change in the peak reflection dip wavelength with changing angle of incident light for data (dots) and simulation (curves) (d) SEM (left) and camera images of fabricated Si_3N_4 structures demonstrating CMY colors [72].

Normal incidence reflection data from fabricated structures with varying thicknesses (54, 80, and 108 nm for yellow, magenta, and cyan, respectively) of Si_3N_4 are shown in Figure 4.4(b) along with a SEM image of a fabricated structure and camera images showing the CMY colors in Figure 4.4(d). Angled measurements were taken and the change in the peak reflection dip was tracked and plotted in Figure 4.4(c), clearly showing good agreement between data and simulation. Higher index dielectrics such as ZnSe show a much smaller shift in reflection ($\Delta\lambda_r/\lambda_r$) with varying incident angle, as expected, allowing for colors that do not vary much with viewing direction.

By utilizing the angle-insensitivity of higher index dielectric Fabry-Perot resonators and the MIM grating absorption filter geometry propsed in section 4.1.2, CMY color filters can be fabricated that can be utilized in thin film reflective display applications. Similar work has also been proposed with thin layers of high index semiconductors to be used in image sensing technologies [74]. The next challenge comes in developing a fabrication method to create filters over large areas that can be used on the flexible substrates that are more common for reflective applications.

4.1.3 Contact printing overview

Using the methods outlined in this section, it is possible to transfer multilayer patterns such as metal-insulator-metal (MIM) layers. While methods involving NIL mentioned above can be utilized for a wide range of applications, they can be difficult on soft, flexible, or non-flat substrates. Microcontact printing, or "soft lithography," was a popular process that used flexible stamps made of materials such as polydimethylsiloxane (PDMS) to transfer self-assembled monolayers to substrates where they could act as a mask for wet etching [75]. Metal transfer printing [76, 77] has more recently been used to directly transfer metal patterns to soft and hard substrates. This is accomplished by first depositing the metal onto a pre-patterned mold. This mold is then placed in contact with the desired substrate while heat and pressure are applied as shown in Figure 4.5. The metal is transferred over due to chemical bonding or higher adhesion to the substrate as opposed to the mold. This metal layer can then be used as a mask for an etching or liftoff process, but experiments have also been done to transfer metal layers for direct purposes such as transparent metal electrodes [78].

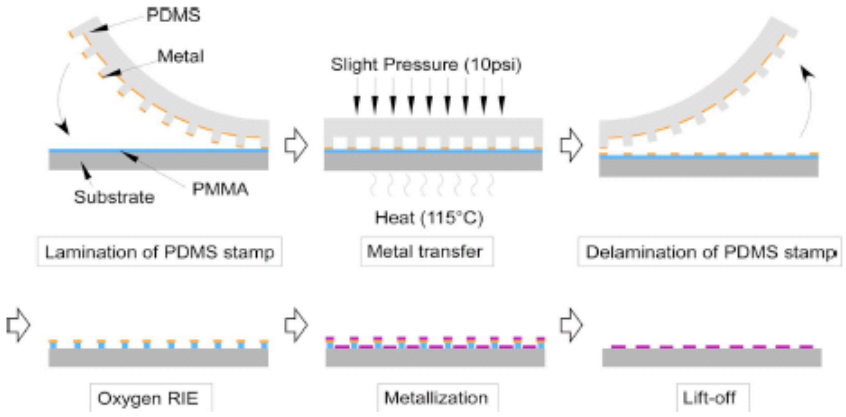

Figure 4.5 Schematic of metal transfer printing process [76].

Given the impressive results from these previous works, we believed that similar processing techniques could be used to transfer our MIM grating color filter structure onto a flexible substrate over a large area.

4.2 Proposed structure

Reflective color displays have become a hot topic in recent technology with large markets in products such as electronic readers and portable displays. The targeted device is a portable, low power display (possibly on a flexible substrate for e-paper applications) which

ideally would use natural light instead of expensive, power-consuming back lighting required for transmission filters. With this objective in mind, a reflective MIM grating structure (Figure 4.6) was proposed and fabricated over a large area using multilayer pattern transfer lithography [17].

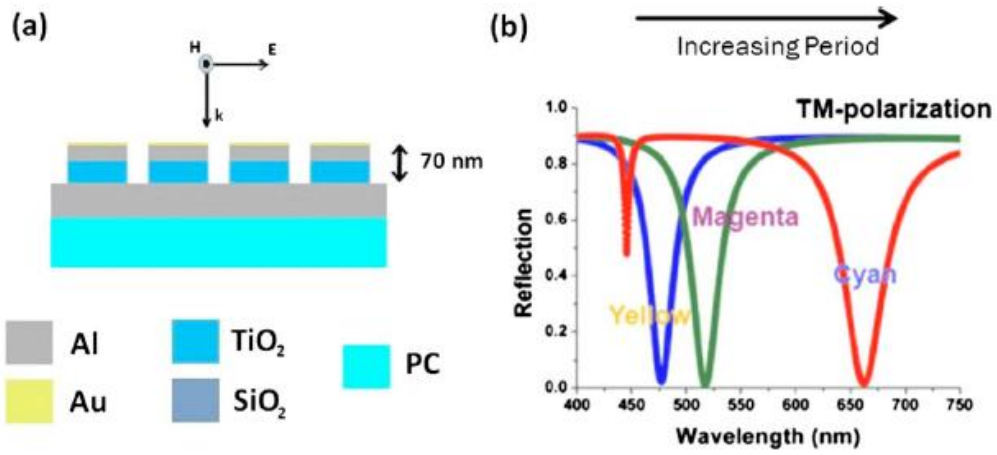

Figure 4.6 (a) Schematic of the fabricated color filter structure and (b) reflection spectra of the structure with varying periods under TM-polarized illumination [17].

Similar to Ref. [68], the top grating period of the MIM structure determines the specific frequency band of light coupled into a plasmonic waveguide, but with the absence of a bottom grating and due to interference with the incoming wave, the light is effectively trapped and absorbed while all other frequencies are reflected, generating a lossy plasmonic waveguide for a specific frequency band. Figure 4.7 shows COMSOL field profiles showing the structural makeup as well as resonance and non-resonance wavelength magnetic field profiles.

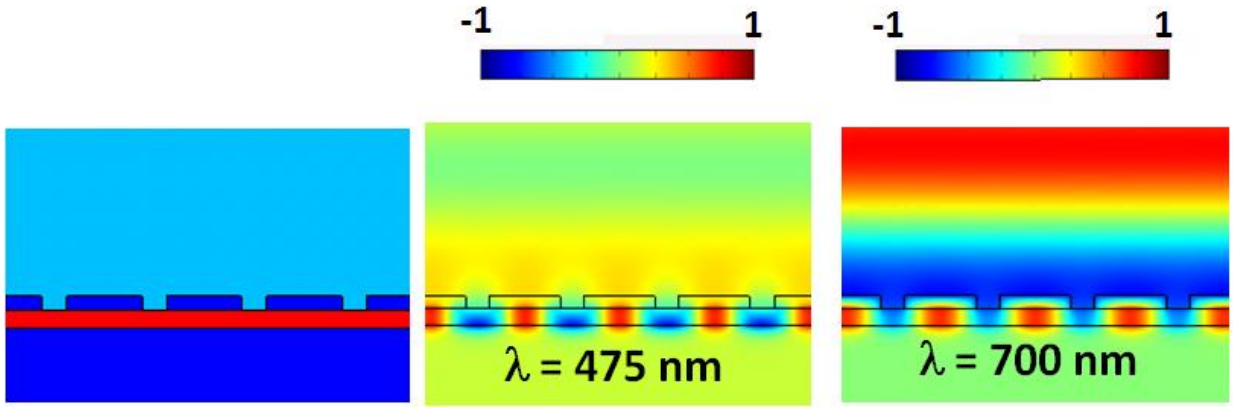

Figure 4.7 (a) Index profile of materials (dark blue = Al, red = TiO_2, light blue = air) and (b) normalized magnetic field (H_y, in/out of the page) profile for resonant wavelength and for (c) non-resonant wavelength for 220 nm period yellow filter

Using this principle, cyan, magenta, and yellow (CMY) color filters could be created by varying the grating period and used as pixels to generate other colors. This method would be much easier for processing as opposed to Fabry-Perot reflective filters above because depth variation to change the color would require much more complex techniques. Pattern transfer lithography was used to transfer a large-area MIM grating filter onto a flexible substrate, making this structure and process a viable candidate for future reflective display devices.

4.3 Fabrication process

A SiO_2 mold was created through traditional NIL methods to act as a stamp for the pattern transfer process. It should be noted that while this structure was used due to the ease of creating deep features, a PDMS mold could also be used as well. The process to deposit and transfer the structure over is outlined in Figure 4.8.

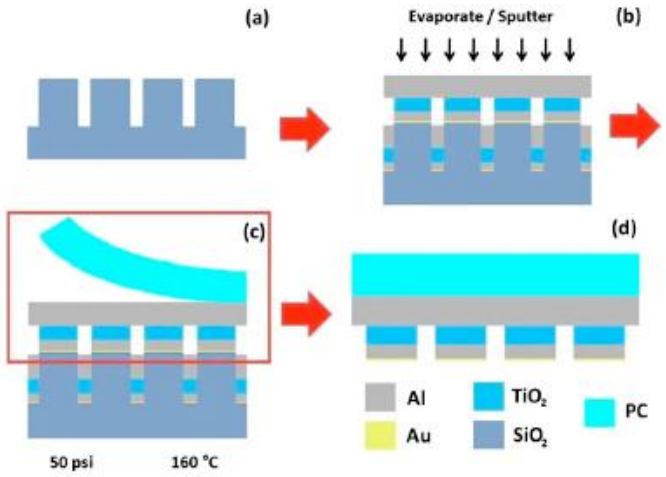

Figure 4.8 Schematic of pattern transfer process: (a) surfactant coated SiO_2 mold (b) evaporation of Au/Al/TiO_2 followed by sputtering of thick and continuous Al (c) pressing of the mold into PC substrate and applying temperature/pressure (d) detaching PC sample (highlighted in (c)) from mold [17].

The SiO_2 mold was first treated with a fluoro-surfactant to reduce adhesion, allowing for easier transfer. The entire reflective grating structure was then deposited onto the mold by evaporation and sputtering. First, a very thin (5 nm) Au layer was deposited since Au does not adhere very well to the mold surface (this is more ideal than Al for the transfer process). Next, 30 nm of Al

and 40 nm of TiO_2 were deposited. All of these steps used e-beam evaporation due to the importance of directionality. Even with e-beam evaporation, some lateral growth of material still occurs, but this was later taken advantage of to produce new filtering structures highlighted in Chapter 6. However, in this case, most of the material not deposited on the top of the grating lines would enter the trenches. Finally, a 100 nm Al layer was sputtered over the sample (final structure shown in Figure 4.8(b)). Sputtering was chosen for a more conformal deposition. Some infiltration between the grating lines was possible, but the trench width was minimal and the sputtered Al formed a continuous layer (see the bottom layer in Figure 4.9).

After the deposition processes are finished, the mold is placed in contact with a flexible, polycarbonate (PC) substrate and a uniform pressure (50 psi) and temperature (160 °C) were applied using a Nanonex NX2000 nanoimprinting tool for 5 minutes. After cooling, the color filter (highlighted in Figure 4.8(c)) could simply be peeled off to realize the final structure in Figure 4.8(d). SEM images of the structure are shown in Figure 4.9. Some particulates appear on the sample due to transfer of material deposited on the sidewalls of the grating, but this did not greatly affect the optical characteristics.

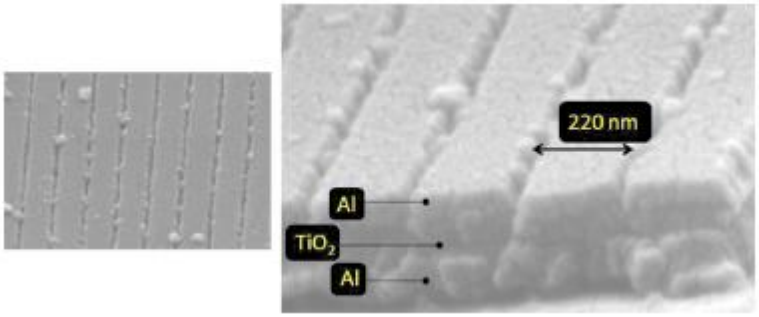

Figure 4.9 SEM images of 220 nm period, yellow color filter [17].

Reflection measurements were taken using a Filmetrics F20 system. Angular measurements were performed using a Woollam variable-angle spectroscopic ellipsometer (WVASE 32). Images were taken using a Philips XL30 FEG SEM.

4.4 Results and discussion

The structure fabricated was a yellow color filter using a 220 nm period grating. The original mold (and final structure) were chosen with this specific period fabricated with a high

duty cycle (>80%) to create high confinement of a complementary band of wavelengths (blue, for the yellow filter). After fabrication, we then compared the reflected spectrum normal to the surface with the simulated spectrum (Figure 4.10).

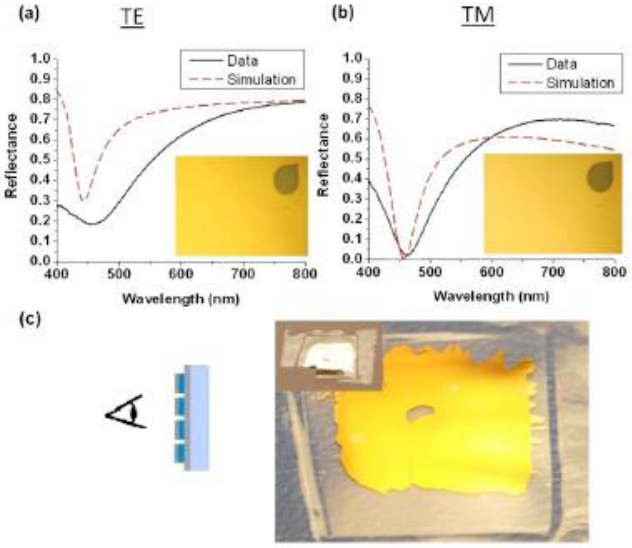

Figure 4.10 (a) TE and (b) TM simulations (red, dashed) and measured data (black, solid) for yellow reflective filter structure with 220 nm period along with microscope images of respective polarizations. The drop-shaped object is a region on the sample without the top Al grating, which provides a polarization independent reference for the optical images. (c) Picture of front of the final transferred structure on PC. The back (inset) looks like a flat Al film while the front shows a distinct yellow color [17].

The first thing to notice when comparing the data with simulation is the good match between the experimental and simulated spectra. The resonance wavelength is nearly the same as predicted by simulation. This can easily be altered by changing the period of the grating. There is an increase in bandwidth when compared to the simulations, but this could possibly be caused by linewidth variation or the particulates mentioned earlier. These issues could possibly be solved with better initial mold fabrication and more controlled deposition. Next, both the simulated and experimental spectra show a strong coupling of targeted wavelengths into the structure, with a near 0% reflectance at the resonance while reflecting ~70% at other wavelengths. This provides a very high contrast to create the sharp yellow color.

Finally, there is also an apparent coupling of blue wavelengths for the TE polarized light as well. While the finding wasn’t understood at the time, it was later discovered that this is due to a Fabry-Perot effect discussed in 4.1.2 where a specific frequency band of light is transmitted through the thin film and reflects multiple times to be absorbed [72]. This absorption region can

be controlled by the thickness of the TiO_2 layer and it turns out that the thickness selection happened to coincide with a yellow filter. This lack of polarization dependence could also be useful in creating a strong color as shown in our images. Figure 4.10(c) shows the front-side image of the yellow filter while the inset shows the contrasting back side image which looks like the 100 nm Al film. A 2-dimensional structure (metal squares instead of gratings) produced a more polarization- and thickness-independent effect to the spectrum as well although, as discussed below, angle tolerance may be affected. Results for a fabricated 2D structure are shown below in Figure 4.11.

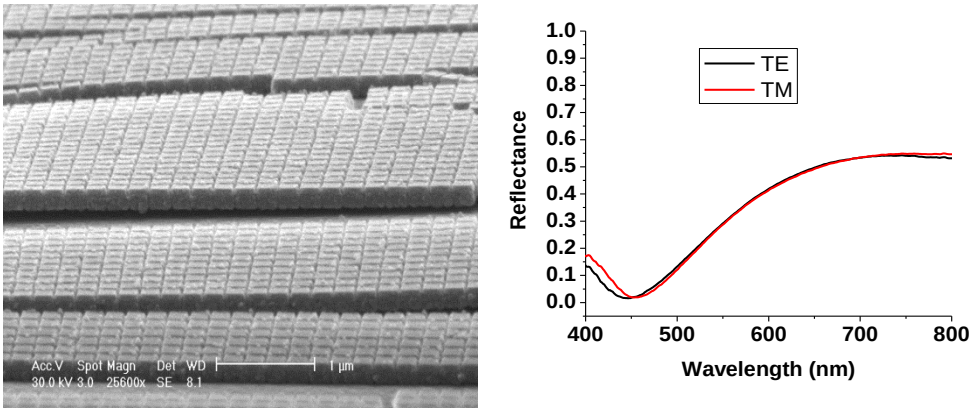

Figure 4.11 (a) SEM image of fabricated 2D structure using similar process to that shown in Figure 4.8, except utilizing a 2D mold to begin and (b) reflection spectra showing little variance between TE and TM polarized reflection from the structure.

The next important feature to highlight is the low dependence of the sample's color on incident angle. For reflective (as well as transmissive) color filters, high angular tolerance could be a strict requirement for many devices. Figure 4.12 shows reflection spectra for TE, TM, and unpolarized light at various angles.

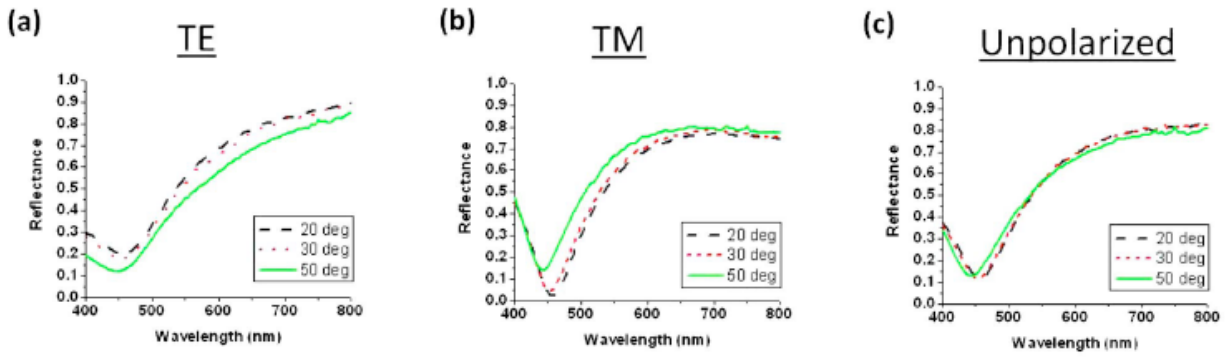

Figure 4.12 Graphs showing angular dependence of (a) TE, (b) TM, and (c) unpolarized reflectance spectra of yellow filter. Angle between the source and detector varies from 20° to 50° [17].

This data was collected using the WVASE 32 ellipsometer with an Al mirror used as a reference. The angles listed are measured between the source and detector. As expected, the TM data shows that there is some variation in the spectra since different angles can change the coupled wavelength, but the data for TE clearly shows that the sample color will remain yellow even when tilted at an angle due to the relative angle-independence of the Fabry-Perot resonance mode for high index dielectrics. The image in Figure 4.10(c) which was also taken at an angle and the unpolarized spectrum measurements in Figure 4.12(c) seem to show, however, that the overall effect of angle changes on the color is not very large. It is also important to note that the angular rotation was done parallel to the grating as opposed to perpendicular. While not shown, it was later found that coupling depends on incident angle as well as whether the sample is viewed perpendicular or parallel to the grating. This variation was still not considered very large in the given angle range, but slightly different than that shown here.

4.5 Conclusion

This work showed a new form of reflective color filter where the spectrum could be easily controlled by the period of the top grating. This structure absorbs light over a specific frequency band while reflecting light at other wavelengths with a very high angular tolerance. Future work investigated a similar structure, outline in Chapter 6, which looked into applications for strong absorption over bands of the IR spectrum. This work also showed that metal transfer lithography techniques could be applied to multilayer structures as well. With the ability to evaporate with more directionality (creating more vertical sidewalls instead of tapering) and

deeper molds, it is possible that even more layers and other complex structures could be transferred using this procedure. A very similar method was recently used to transfer large stacks of negative index materials onto flexible substrates [79].

Chapter 5

High efficiency transmission color filters with tunable bandwidth

5.1 Introduction

While much of the work in Chapter 4 focused on reflective color filters and improvements on angular tolerance, other aspects of spectral filtering are also under investigation. Transmission filters used in typical display technologies such as televisions may require wide viewing angles, but other applications such as near-to-eye displays (NEDs), image sensing, and spectroscopy applications may trade viewing angle issues for other parameters such as transmission intensity and spectral purity.

Research on devices to achieve these goals has progressed down a variety of avenues. Recent extraordinary optical transmission (EOT) devices [70, 80] have begun to apply the research conducted by Ebessen, et. al. [16, 81, 82] into color filtration, but early results have achieved relatively low transmission. Metal-insulator-metal structures mentioned in Chapter 4 [66, 68] utilize plasmonic waveguide structures to filter specific wavelength bands, but higher transmission values and narrower bandwidths may be required for some of the above applications.

Resonant waveguide gratings (RWG) [69, 71, 73] have also received attention due to their ability to achieve higher transmission peaks. Most papers cite the work of Kanamori et al. [69] as one of the first examples of the RWG structure. Subwavelength period Si gratings were used to create a "guided-mode resonant" (GMR) condition when placed on a dielectric substrate. With subwavelength periods, only the zeroth order diffraction mode and evanescent/surface modes are available. Evanescent modes are excited at specific wavelengths determined by the grating period and constructively interfere with zeroth order light that passes through, effectively creating a bandpass filter where the peak wavelength is controlled by the period of the grating [83]. Further work, and the more recent studies in Ref. [71, 84], sought to increase control over the peak transmission and color purity from RWG structures by incorporating metal gratings to

excite surface plasmon modes at the surface and inserting guiding layers with a higher refractive index than the surroundings in order to create interference between the grating and guiding layer modes. Most of these structures were either simulated or fabricated using techniques that cannot be applied to manufacturing situations (e-beam, focused ion beam).

5.2 Proposed structure

The fabricated structure presented below is a nanostructured color filter referred to as a metallic resonant waveguide grating (MRWG) with the ability to achieve some of the highest reported peak transmission values while allowing for control over the spectral bandwidth [18]. The structure and simulated transmission spectra are shown in Figure 5.1.

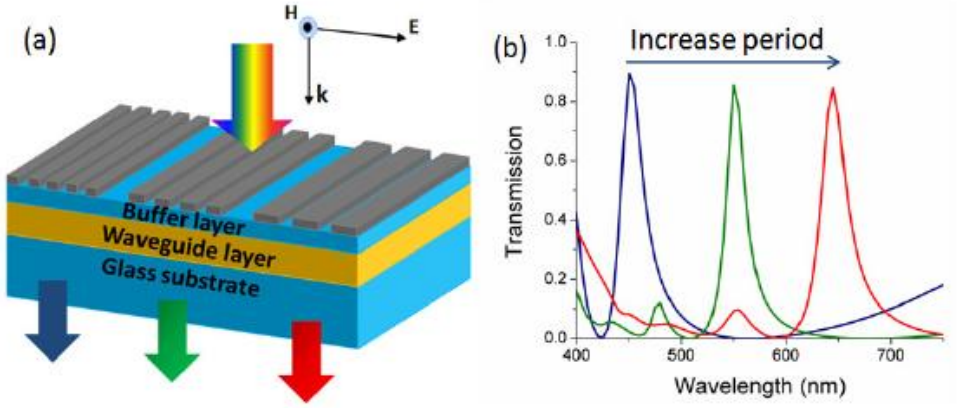

Figure 5.1 (a) Schematic of transmissive color filter structure and (b) Simulated transmission spectra [18].

The schematic of the structure in Figure 5.1(a) consists of two dielectric layers deposited on a glass substrate with a wide linewidth metallic grating on top. Similar to the reflective color filter in Chapter 4 and other RWG structures, by varying the period, one can change the color of the filter. Simulated transmission spectra from COMSOL of red, green, and blue (RGB) filters are shown in Figure 5.1(b) with periods of approximately 280, 350, and 420 nm, respectively. Simulations used dielectric constants measured by spectroscopic ellipsometry and metal constants from Ref. [85]. The 40 nm thick, ~75% duty cycle grating couples light of a specific frequency band into a GMR and the waveguide formed below it. This waveguide consists of a 100 nm thick, high-index, dielectric "waveguide" layer, such as Si_3N_4, surrounded by two cladding layers, which include the glass substrate and the SiO_2 "buffer" layer. Unlike similar

works, this "buffer" layer is shown to have an impressive effect on the confinement/bandwidth of the light in the waveguide structure, allowing us to tune the transmitted spectrum for different applications.

To predict the resulting transmission peaks, one can solve the eigenmode equation for the waveguide structure formed by the dielectric layers assuming transverse magnetic (TM, electric field perpendicular to the metal grating) polarized light. The permittivity of each layer is assumed to be ε_1, ε_2, and ε_3, for the "waveguide" layer, "buffer" layer, and substrate, respectively, yielding the equation for TM modes as:

$$(k_0^2\varepsilon_1 - \beta^2)^{1/2} d = m\pi + \arctan\left(\frac{\varepsilon_1}{\varepsilon_2}\cdot\frac{\beta^2 - k_0^2\varepsilon_2}{k_0^2\varepsilon_1 - \beta^2}\right)^{1/2} + \arctan\left(\frac{\varepsilon_1}{\varepsilon_3}\cdot\frac{\beta^2 - k_0^2\varepsilon_3}{k_0^2\varepsilon_1 - \beta^2}\right)^{1/2}$$

where β is the propagation constant, k_o is the free space wavenumber, d is the "waveguide" layer thickness, and m is an integer. The calculated dispersion is shown in Figure 5.2. The shaded region highlights the range of the TM_0 mode in the visible spectrum, showing nearly linear behavior over the entire visible spectrum. We also notice that the TM_1 mode lies outside of visible, allowing us to follow the linear dispersion with no interference from other guided modes.

The longitudinal wavevector (i.e. propagation constant β) of the guided modes can be provided by the first order scattering of incident light by the metal grating, given as $\beta = \pm 2\pi/P + k_0 \sin\theta$ (where P is the grating period and θ is the incident angle). We can choose the proper grating period to efficiently couple the incident light into GMR / waveguide modes at a specific resonant wavelength. Some refer to this combined resonance effect of both the grating and waveguide as a so-called Fano-resonance, typically producing a similar line-shape to our transmission spectrum and characterized by high intensity resonances [86]. To confirm this, COMSOL simulations of MRWG devices with periods from 250 nm to 450 nm (10 nm step) were run and the peak wavelengths were plotted as circles in Figure 5.2, showing good agreement with the calculated TM_0 modes for the waveguide structure alone. To avoid generating two different resonant modes, here we only consider normal incident light where θ =0. As was mentioned in the introduction, this is also where the strong angle-dependence of the structure is realized, making it non-ideal for large-area display applications. While propagating

in the waveguide, the modes can scatter again from the wide linewidth metal grating into far field. This is where the color from the filter is realized.

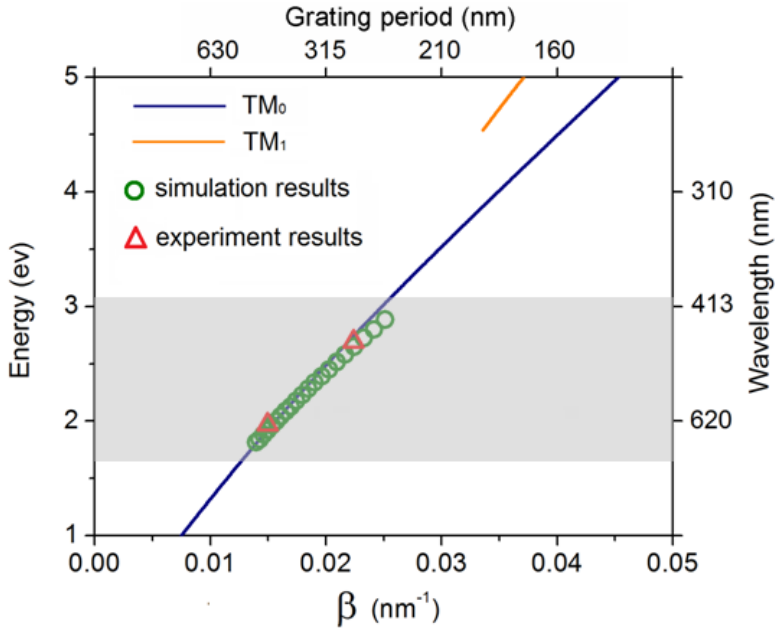

Figure 5.2 Calculated dispersion of the dielectric waveguide for TM polarized light. The waveguide layer is made of Si_3N_4 with 100nm-thickness. Surrounding material is SiO_2. Green circles and red triangles correspond to simulation and experiment results, respectively. Shaded region indicates the visible spectrum [18].

The dispersion relation in this figure shows strong agreement with the simulated transmission peaks (circles) for the MRWG structures. The triangles shown in the plot also show the peak wavelengths achieved during fabrication of actual structures for blue and red filters with 280 nm and 420 nm periods, respectively. These results also demonstrate good agreement with both the waveguide mode calculations and simulated structures. Below, the fabrication process is outlined for how these filters were achieved.

5.3 Fabrication process

To begin, fused silica substrates were cleaned before depositing 100 nm of Si_3N_4 for the "waveguide" layer and 50 nm of SiO_2 for the "buffer" layer (although this was later varied) using plasma-enhanced chemical vapor deposition (PECVD). An imprint resist (mr-I 8030, Microchem) was spun on the samples and then imprinted with a 280 nm period or 420 nm period

wide-linewidth mold (these two molds were available to us and could be used to realize blue and red color filters, respectively) using a Nanonex NX2000 (Nanonex, NJ). The resulting narrow linewidth resist pattern was then etched with an O_2 plasma to remove the residual resist layer. Approximately 40 nm of Ag was then deposited by e-beam evaporation, followed by liftoff in acetone to produce wide linewidth gratings. An example image is shown in Figure 5.3(a) for the 420 nm period, red color filter.

After fabrication, transmission measurements were taken using a Woollam variable angle spectroscopic ellipsometer (WVASE 32). Images were taken using a Hitachi SU8000 ultra-high resolution SEM.

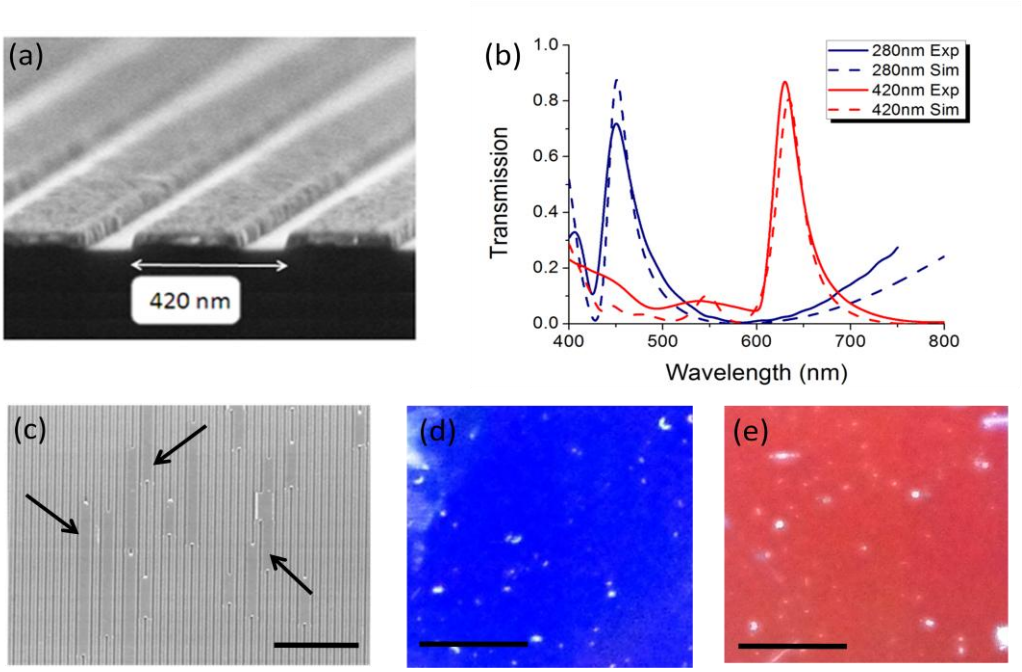

Figure 5.3 (a) SEM image of the fabricated structure. The grating period is 420nm. (b) Comparison between experimental and simulated spectra for blue (280 nm period) and red (420 nm period) color filters. (c) SEM image showing defects in 280 nm period metal grating. Scale bar 3 μm. Optical images of (d) blue and (e) red filter illuminated by TM-polarized white light. Scale bar 5 mm [18].

5.4 Results and discussion

In Figure 5.3(b), a comparison between simulated and experimental transmission spectra is shown for the 280 nm (blue) and 420 nm (red) period samples. From these spectra, the transmission peak wavelengths were also plotted in Figure 5.2 as triangles. In both of these

figures, we can see that the experimental peaks match very well with calculated waveguide modes and simulated values. The red filter spectrum is also shown to match particularly well with simulations and produced a peak transmission of approximately 90%.

The blue filter achieved approximately 75% transmission at its peak, which is lower than the simulated prediction, but the nearly identical line-shape of the spectrum led us to investigate the quality of the filter after fabrication. Upon investigation, we found that while the 420 nm period Ag grating shows very few defects, Figure 5.3(c) shows that the fabricated 280 nm period Ag grating contains a large number of defects, indicated by arrows. This can most likely be attributed to defects in the original mold used in the nanoimprinting process. This seems to explain why the overall transmission efficiency of the structure dropped while very few other features of the spectra were affected. With future improvements to the mold, we believe that the targeted ~90% transmission peak could be achieved.

Color images of both the blue and red filters illuminated by TM-polarized light are also shown in Figures 5.3(d) and (e), respectively, and still show pure colors with high transmission efficiencies for both devices. The overall filter size fabricated was 1.25 cm by 1.25 cm due to the original size of the mold. Another issue to address in the future is the large white dots in the images which were caused by particles and defects during the PECVD oxide/nitride processing of the substrate. With better tool control, this should be able to be eliminated as well.

Another advantage of the proposed MRWG is the ability to tune the bandwidth of the transmission peak from narrow to wide by controlling the thickness of the “buffer” layer. In Figure 5.3(b), the transmission peaks have a full-width at half maximum (FWHM) of approximately 30 nm, much narrower than previously reported results [14, 16, 68-71, 80-82, 84]. This could be quite useful in certain sensor and spectroscopic applications, but the device can also achieve much wider bandwidths by decreasing the thickness of the “buffer” layer. This observation can be explained by the theory behind a metal cladding dielectric waveguide [87]. When the “buffer” layer thickness is reduced, the loss of the waveguide modes from the metal grating will increase, causing a lower resonance Q-factor and widening the bandwidth by simultaneously reducing the waveguide cladding thickness and increasing the effects of the metal grating. Figure 5.4 shows an experiment done to confirm this where a red (420 nm period) spectrum from a sample fabricated with no “buffer” layer is compared with the original spectrum from Figure 5.3(b). This causes an increase in the FWHM from 30 nm to 70 nm. This ability to

tailor the bandwidth of the transmission spectrum while having little effect on the peak transmission can be very useful in display and image applications.

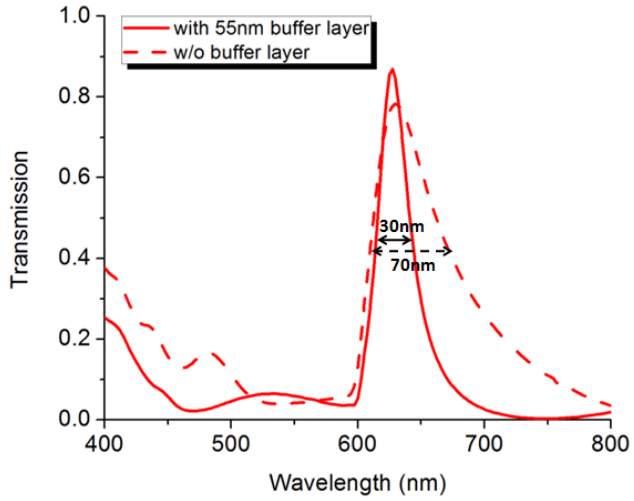

Figure 5.4 Experimental results demonstrating tunable transmission bandwidth variation for a red (420 nm period) filter with and without oxide "buffer" layer [18].

It should also be noted that simple changes in fabrication processing such as using 2D molds or a thicker metal grating can lead to a polarization-independent architecture or a polarizing filter, respectively, similar to the methods used in Chapter 4.

5.5 Conclusion

This work demonstrated a thin-film color filter device fabricated using nanoimprint lithography. It can potentially be used in a wide range of spectral filtering applications due to the high transmission efficiency, ability to determine the color by varying the period of the grating, and control over the spectral bandwidth of the peak by adjusting the thickness of the "buffer" layer. Since the structure only requires one patterning step, it could easily be utilized in higher throughput manufacturing processes such as roll-to-roll nanoimprint lithography [28] or dynamic nanoinscribing [88]. Although we used a 1D structure in this example, a 2D, polarization-independent structure can also be created using a similar design as a recent group demonstrated [89, 90]. A structure that only transmits TM-polarized light (while reflecting TE) can also be fabricated by using a thick metal grating.

Chapter 6

Hyperbolic metamaterial waveguides for broadband absorption

6.1 Introduction

Previous chapters have shown that MIM structures can be used to create strong absorption at certain resonant wavelengths. These resonances are created by coupling into Fabry-Perot or waveguide modes of subwavelength feature sizes, using high field confinement and lossy materials to absorb light at the specific frequency coupled into the structure. However, either by operating at longer wavelengths or using new fabrication technology, structures based on highly subwavelength features ($< \lambda/10$) begin to be approximated as a so-called "metamaterial." These materials can have properties not found in nature and a certain class of metamaterials known as hyperbolic metamaterials (HMM) has become a hot topic among scientists.

In this chapter, nanostructures made of tapered HMMs are created over large areas using nanoimprint lithography. Due to their impressive ability to couple in a wide band of wavelengths and high degree of confinement, these structures are able to achieve broadband absorption. Multiple designs are presented targeting absorption in visible, short IR, and mid IR. Following these results, analysis of simulations is used to discuss light coupling and propagation within the structure to better understand the broadband absorbing effect.

6.1.1 Metamaterials and negative refractive index

Often credited to the work of J.B. Pendry in the mid to late 1990s [91, 92], metamaterial research has taken off within the past couple of decades along with improvements in subwavelength patterning technology. Pendry referred to the idea of creating "artificial atoms," sometimes called "meta-atoms" by other scientists today, that would make up a new material with unique optical properties. Since these features would be highly subwavelength, like atoms in a natural material, their effects can be averaged out and lead to an approximation as an

effective medium with values of permittivity (ε) and permeability (μ) that can be controlled by the structural parameters [93-95].

This radical change in philosophy meant that the shape or organization of subwavelength structures could have a drastic effect on the optical properties. One of the primary fields that was targeted for metamaterial research involved negative refractive index materials (NIMs). Since they were proposed in 1968 [96] to the present day, scientists have sought to create NIMs in the visible regime for applications involving cloaking or perfect lenses for optical lithography [97]. The index of refraction of a material is given by $\boldsymbol{n = n' + in'' = \sqrt{\varepsilon\mu}}$. Where n' is the real part of the refractive index and n'' is the imaginary part. ε and μ are the permittivity ($\boldsymbol{\varepsilon = \varepsilon' + i\varepsilon''}$) and permeability ($\boldsymbol{\mu = \mu' + i\mu''}$), respectively. However, to achieve an ideal NIM, it is also important to define a figure of merit (FOM): $\left|\frac{\boldsymbol{n'}}{\boldsymbol{n''}}\right| = \left|\frac{\boldsymbol{\varepsilon'|\mu|+\mu'|\varepsilon|}}{\boldsymbol{\varepsilon''|\mu|+\mu''|\varepsilon|}}\right|$. This ratio between the real and imaginary parts is important in defining the achievable n' as compared to the loss present in the material (n'').

Looking at this equation, to achieve a negative value of n' along with a high FOM, we want to reduce loss and achieve simultaneous high negative ε' and μ'. As we discussed in Chapter 3, metallic structures already have natural bands of negative ε', but the negative μ' is not achievable in natural materials. In 2009, we performed our own work to attempt to fabricate a large-area material using NIL that would have a simultaneous negative ε' and μ' in the visible regime [98]. This structure was based off of Pendry's famous split ring resonator (SRR) structure outlined in Ref. [92] which approximates an inductor-capacitor resonator circuit with a distinct resonance where a magnetic field opposing the incoming field is generated, leading to a negative μ'. These ring-like structures could be created by sputtering metal over a pre-patterned substrate with a grating generated by NIL. This combination of SRR structures with –μ' and metallic gratings with –ε' is typical of NIM structures. A summary of the structure and results is shown in Figure 6.1.

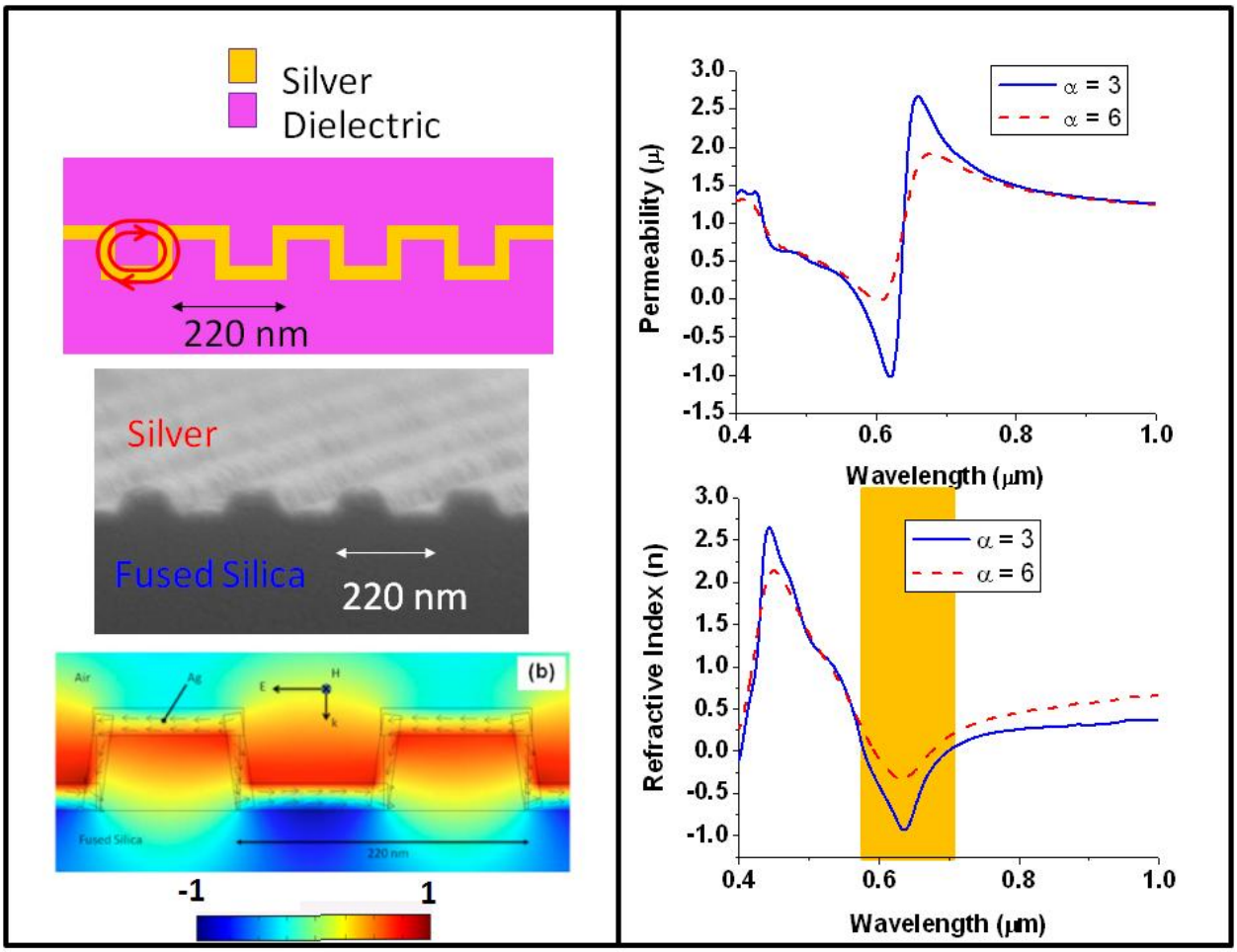

Figure 6.1 Summary of results from proposed NIM research showing, on the left, a schematic, SEM image of a fabricated grating, and COMSOL H-field profile (top to bottom). On the right, the top graph plots simulated μ' for structures with varying loss parameters (α values) while the bottom graph plots the simulated n' [98].

The left side of the figure shows 3 diagrams of the continuous split ring resonator grating (CSRRG) structure. The top diagram defines a 220 nm period Ag grating (metal thickness ~ 20 nm) created by sputtering the metal over a fabricated grating structure and coating it with the same material as the substrate. An example of the fabricated metal grating on fused silica prior to coating is shown below. This symmetric grating structure, when viewed from the edge shows a layer of connected SRRs (red arrows) which resonate with oppositely polarized magnetic fields when excited with TM-polarized waves (H-field in/out of the page represented by blue/red). The bottom diagram shows a COMSOL simulation at the resonant wavelength just over 600 nm where the incoming H-field is polarized into the page (blue) and the generated H-field has an

opposite polarity (out of the page, red). The figures to the right show the simulated real parts of the permeability (top) and refractive index (bottom) showing n' < 0 for a region of approximately 100 nm bandwidth in the visible regime (highlighted in yellow).

Another important factor in NIMs is the loss of the materials involved, primarily the metal or plasmonic material. As discussed in Chapter 3, metals have the necessary optical properties to generate $-\varepsilon'$ due to their plasma frequency, but their loss tends to be high in the visible regime, limiting the FOM. The plots in Figure 6.1 show two curves for $\alpha = 3$ and $\alpha = 6$ where α represents a loss factor incorporated into the model fit of the metal optical constants. Although the loss of metals can be improved by better deposition methods, an α of 6 as shown in the figure is certainly reasonable, and it can lead to major reduction in the FOM for our NIM. The high loss and low transmission of our structure unfortunately limited its practical use, despite the possibility of a negative index response in the visible regime.

Other scientists have been able to achieve very impressive results and shift the magnetic response and negative index properties into the optical regime primarily by using the so-called fishnet structure [24, 79, 99, 100]. The fishnet structure is a perforated stack of metal-insulator layers which were made to approximate SRRs as well, but now the MIM structure has two "splits" on each end and is layered in stacks. The structure from Ref. [24] is shown below in Figure 6.2.

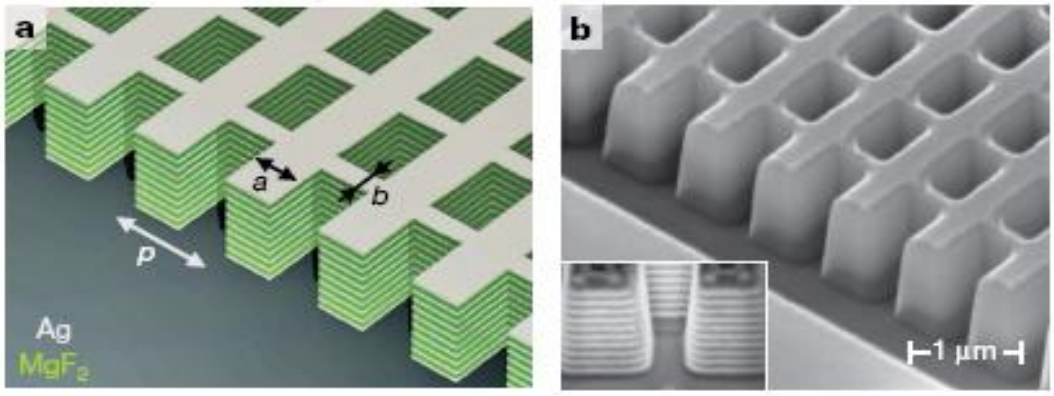

Figure 6.2 (a) Diagram showing multilayer fishnet structure (b) fabricated structure made with Ag/MgF_2 stacks using focused ion beam milling [24].

This structure is shown because it is very similar to the HMM discussed later. This is no surprise since negative index materials are inherently anisotropic as well, so properties of negative index materials such as opposing phase and power propagation are present in HMM structures. The results for the fishnet structure also provided major improvements in transmission and loss reduction by proving that neighboring metal-insulator layers led to a coupling effect which created a broader resonance and lower loss [24, 100].

6.1.2 Hyperbolic metamaterials (HMMs)

NIMs may still be one of the most heavily researched fields in metamaterials, but other anisotropic materials that do not focus on permeability, such as hyperbolic metamaterials (HMMs), are receiving considerable attention. The past few years have seen numerous publications in highly regarded journals primarily focused on the theoretically infinite photonic density of states (PDOS) that can be achieved in HMMs [23, 101-103]. Scientists have long studied the spontaneous emission rate of dyes or quantum dots and found that placing the emitters near or in a structure with a high PDOS will significantly enhance the Purcell factor, a metric for emission. While this field of research continues to progress, it is well known that the loss of typical materials used in HMM structures will inhibit an infinitely large PDOS from forming, so gain material incorporation may be necessary [104]. However, HMMs still possess interesting optical characteristics despite the loss. Other recent work in HMMs has focused on light propagation within the structure [105] and made use of unique optical properties of the material dispersion, investigating superluminal group velocity [106], creating materials for subwavelength imaging [107-109], or taking advantage of enhanced optical forces for optomechanical applications [110]. Some of these applications highlight one of the key properties of HMMs (and NIMs), namely, "phase compensation." It is well known that phase propagation can occur in the opposite direction of power propagation in these materials, and we will later discuss the relevance to our results.

There are two typical architectures discussed when analyzing HMMs: the nanowire and the multilayer metamaterial structures. Although I will mainly focus on the multilayer architecture, it is important to note that both structures are very similar, containing alternating, periodic metal and dielectric layers which are highly subwavelength in at least one dimension in order to generate a highly anisotropic permittivity. These are also sometimes referred to as "indefinite" media. The multilayer structure is defined in many of the references while a good

outline of the nanowire structure can be found in [111]. An example diagram of a multilayer effective medium and the resulting wave vector ($k=2\pi n/\lambda_o$) dispersion are shown in Figure 6.3(a) and (b).

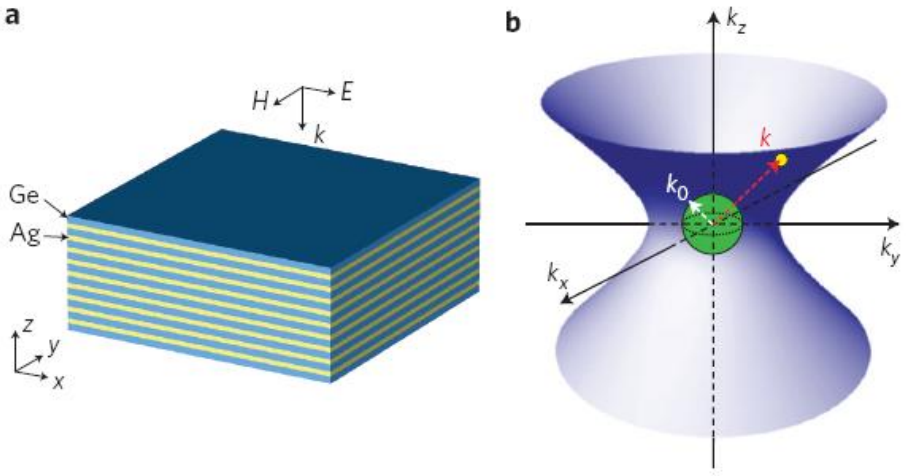

Figure 6.3 (a) Example structure of planar, multilayer effective medium made of highly subwavelength sheets of Ge and Ag and (b) the resulting hyperbolic isofrequency curve (green sphere shows free-space curve) at a certain frequency [22].

While still under some debate, most scientists use Maxwell-Garnet effective medium theory [112] for sufficiently small structures to calculate the permittivities in the direction parallel (ε_{xy}) and perpendicular (ε_z) to the sheet surfaces, getting the following equations:

$$\boldsymbol{\varepsilon_{xy} = f(\varepsilon_m) + (1 - f)(\varepsilon_d)}$$

$$\boldsymbol{\varepsilon_z = \frac{\varepsilon_m \varepsilon_d}{(1 - f)(\varepsilon_m) + f(\varepsilon_d)}}$$

where ε_m and ε_d are the complex permittivities of the metal and dielectric, respectively, and *f* is the fill ratio of the metal in a single metal-dielectric period. These two equations clearly demonstrate the anisotropy of the permittivity in perpendicular directions. Furthermore, as we know from analyzing metals in Chapter 3, at frequencies larger than the plasma frequency, metals can have a large, negative permittivity while the dielectric permittivity remains positive. From the equations above, we can see that ε_{xy} could easily become negative over a long range of frequencies while ε_z could remain positive. We can see the important effect this has on propagation within the material by looking at the dispersion equation for an anisotropic medium, shown below:

$$\frac{k_{xy}^{\,2}}{\varepsilon_z} + \frac{k_z^{\,2}}{\varepsilon_{xy}} = \frac{\omega^2}{c^2}$$

where k_{xy} refers to the wave vector in the x or y-direction (assuming symmetry), k_z is the z-direction wave vector (propagation direction), ω is the angular frequency of light, and c is the speed of light.

Figure 6.3 (b) shows a plot of the isofrequency, or k-space, curves for free space (green sphere, an isotropic material $\varepsilon_{xy}=\varepsilon_z$) and a hyperbolic material (an anisotropic material with $\varepsilon_{xy} < 0$ and $\varepsilon_z > 0$). Most dielectric materials are considered to be isotropic or contain anisotropy with positive values of both ε_{xy} and ε_z, forming a sphere or ellipsoid isofrequency curve as the equation above would suggest. When ε_{xy} becomes negative and ε_z stays positive, if frequency is held constant, instead of k_{xy} decreasing as k_z increases, k_{xy} now increases with k_z to stay on the same hyperboloid / isofrequency curve. This result is what has led to all of the research topics above. For example, we can see that instead of the range of allowed wave vectors being confined to a certain ellipsoid or sphere in a typical dielectric material, allowed states should theoretically be able to continue on to higher k_{xy} and k_z values, leading to ultra-high refractive indices and a much larger PDOS [23, 91-93]. The ability to sample higher order wave vectors than those allowed in typical materials is used in subwavelength imaging capabilities or hyperlensing [107-109]. The next section will discuss how HMM can be used to generate broadband absorption.

6.2 HMM broadband absorbers

Many articles in recent years have looked into tailoring plasmonic nanostructures with specific resonances into materials which will absorb over a wide range of frequencies. These broadband absorbers (BBAs) make use of the high loss in plasmonic structures that typically inhibits their practical use to create nearly perfect absorption at certain resonant wavelengths for structures such as color filters [113, 114] or utilizing Kirchoff's law to create selective thermal emitters [115], similar to the way that loss was utilized in the structures outlined in Chapters 3 and 4 for UV or visible light absorption. BBAs have been proposed for a different set of applications since materials with wide bands of absorption over certain regions like the IR or THz can be difficult to find [116]. This can include applications such as IR cloaking [117], thermal detection [118-120], solar cells [121, 122], creating wider band thermal emitters than

those in [115], or harvesting waste heat for energy applications [123]. Some of these methods use materials such as carbon nanotubes to absorb light over a very large range of frequencies, but this involves structures that are microns thick and there is little control over the spectrum. To create controlled absorption over a broad band, most scientists have focused on confining multiple structures with overlapping resonances into subwavelength pixels [20, 124-126]. However, while these structures can create very high absorption through field confinement along with angle intolerance, only a finite amount of absorbers can be crammed into an area, limiting the bandwidth and complicating the fabrication procedure.

Anisotropic metamaterial structures have also been proposed for broadband absorption, although these began as theoretical works to prove HMM properties through simulation [127-130]. One elegant design which is focused on below is a metamaterial architecture with a tapered structure of metal-insulator stacks which showed slow-light waveguide properties, effectively stopping light at a certain depth within the medium over a wide range of frequencies [21]. A diagram showing the structure and BBA capability is given in Figure 6.4.

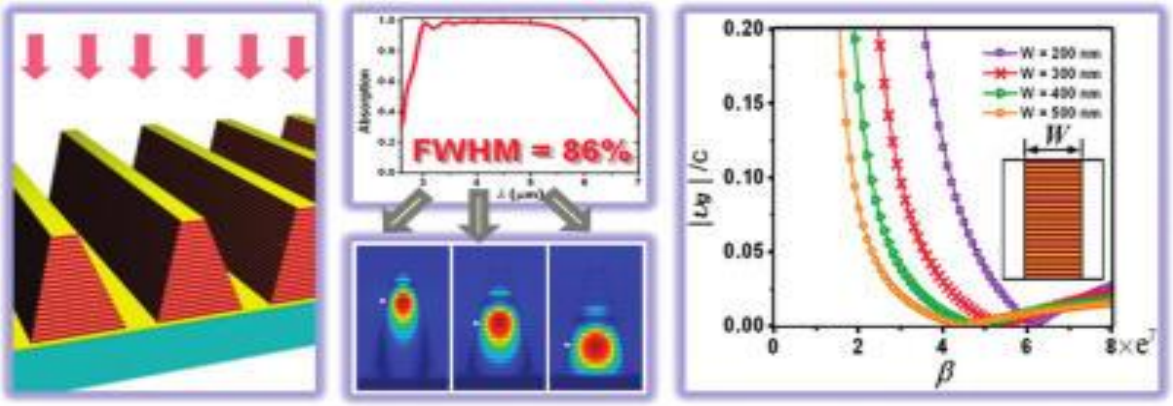

Figure 6.4 (Left) Diagram of tapered metal-dielectric BBA grating, (center) curve and field simulations showing absorption over a broad range of wavelengths, and (right) dispersion curves demonstrating slow-light waveguide theory [21].

Interestingly, this structure is quite similar to a nanostructured HMM which was recently analyzed in Ref. [22].

The goal of my work was to provide the first experimental evidence of metamaterial BBAs over large areas in the visble and IR range since structures had only been demonstrated in the microwave [131]. I also sought an explanation of this absorption by utilizing HMM theory

and worked to connect it with the two works of Ref. [21, 22] and explain how resonant phenomena can affect the quality of broadband absorption. This fabrication method and analysis could lead to many types of nanostructures with interesting optical properties not typically found in nature.

6.3 Fabrication procedure

Creating patterned nanostructures of alternating metal and dielectric layers over large areas in order to operate at visible or IR wavelengths comes with a host of challenges. As mentioned above, similar structures known as fishnet metamaterials have been fabricated, but these were mostly done through focused ion beam milling or e-beam lithography, limiting their practical applications. Creating a mask over a large area on pre-deposited metal-dielectric layers and using a reactive ion etching process has been proposed in Ref. [21], but thick masks of etch resistant materials and etch byproduct removal become major hindrances as the number of layers increases. Below is a simple method where all layers are directly deposited on a nanoimprinted resist template, naturally forming the tapered stack nanostructures. This is possible because physical vapor deposition (PVD) processes are not completely directional, and some lateral growth on top of the mask structure is very common, particularly with dielectric materials [132, 133]. This lateral growth effectively masks further deposition in the regions below, creating a tapered nanostructure on the substrate with decreasing width as PVD progresses. When fabricating the reflective color filters in Chapter 4, similar tapering occurred, even over thin depositions. For the purposes of this work, this can lead to significant changes in the width of the resulting structure by hundreds of nanometers.

The process to create tapered BBA arrays over large areas is presented in Figure 6.5.

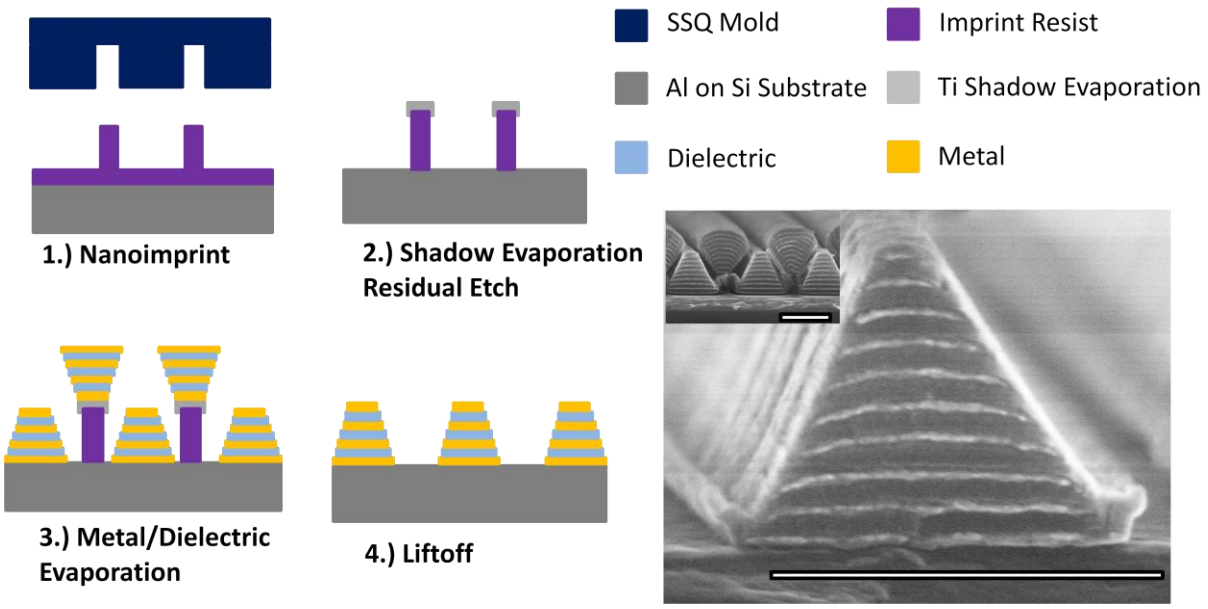

Figure 6.5 Fabrication process and SEM images for broadband absorber structure. (Left) Process flow for fabrication of tapered metal-dielectric structures using nanoimprint lithography. (Bottom right) SEM image of final 700 nm period structure with 9 stacks of Au-Al_2O_3 and (inset) prior to liftoff (Step 3). (scale bars represent 500 nm)

To begin, a reflective substrate (100 nm thick Al on a Si chip followed by a thin Cr adhesion layer) is coated with imprint resist and stamped under high temperature and pressure to create tall, narrow linewidth gratings (or a two-dimensional mesh if fabricating pillars). A thin Ti shadow deposition is then used to coat the tops of the gratings and a reactive ion etch is performed to remove the residual resist using an O_2 plasma. This shadow evaporation process prevents the thinning of the narrow resist lines while simultaneously determining the bottom width of our nanostructure.

In the next step, alternating metal and dielectric layers are deposited in succession until the desired height is achieved. Materials such as Au and Al were used for metals while SiO_2, Al_2O_3, and Ge were used for dielectrics. As illustrated in Step 3, the finite lateral growth on top of the resist masks deposition onto the substrate, creating a reduced linewidth in the final structure with subsequent deposition. The amount of lateral growth and overall tapering of the structure has been shown to be dependent on a variety of factors including the directionality of the evaporated material and its ability to diffuse on the surface before sticking. This means that parameters such as deposition rate, substrate temperature, surface mobility of materials, and collimation of sources can be used to affect the finished structure [79]. Typical sidewall angles

for fabricated structures were approximately 75°-80°. Finally, an acetone liftoff is performed to remove the mask and the material deposited on top, completing the BBA fabrication process (scanning electron microscope (SEM) images are shown in the bottom right of Figure 6.5).

Various results for tapered BBA nanostructures with a range of geometries and materials are presented to achieve absorption at visible and IR frequencies. The tapered deposition technique combined with nanoimprint lithography is compatible with most PVD materials and can be easily used to create one-dimensional grating or two-dimensional pillar structures, allowing for large-area fabrication of polarization-independent tapered architectures. This technique could be applied to other recent fields of study including improved absorption in solar cell devices [134] or field enhancement at nanotips [135].

6.4 Experimental results

Reflection spectra from fabricated BBA structures were taken using a Fourier Transform Infrared (FTIR) spectroscopy tool with a microscope attachment and compared with simulations performed using COMSOL Multiphysics. Data and simulations were performed with transverse magnetic (TM) polarized waves with electric field perpendicular to the grating. Dielectric properties of simulated materials were taken from tabulated data in literature [48, 49]. Utilizing this tapered deposition technique allows one to easily change materials and tailor the strong absorption to specific regions. To absorb at longer wavelengths, a larger period mold and/or a dielectric with a higher permittivity can be used while shorter periods and/or lower permittivity materials can be used to absorb primarily at shorter wavelengths. As mentioned earlier, changing the thickness of shadow evaporated material in Step 2 of Figure 6.5 can also lead to narrower BBA structures. Figure 6.6 shows data from 3 structures with targeted absorption in different regions.

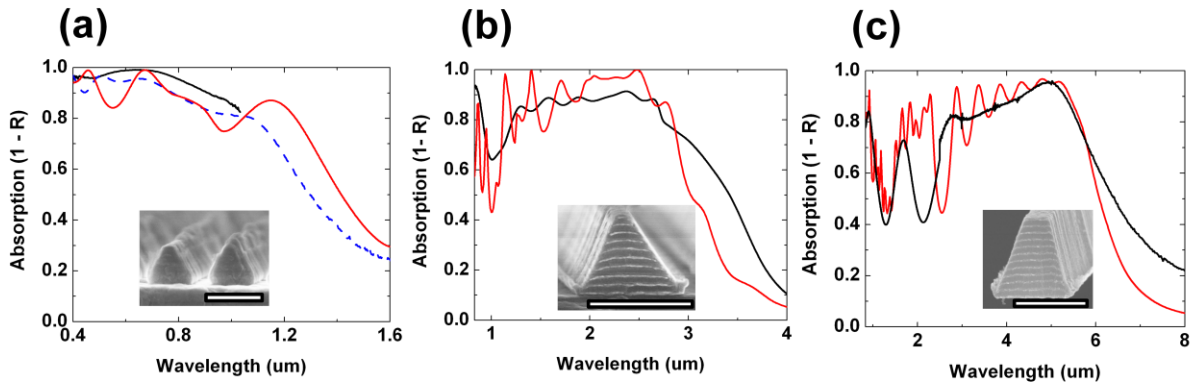

Figure 6.6: Data (black curve) and simulated (red curve) absorption curves for BBAs with SEM images inset. (a) 220 nm period, 3 stack structure (Al-SiO_2) absorbing from ~0.4-1.2 μm, includes angle data at 45° (dashed blue curve). (b) 700 nm period, 9 stack structure (Au-Al_2O_3) absorbing from ~1.5-3 μm. (c) 700 nm period, 11 stack structure (Au-Ge) absorbing from ~2.5-6 μm. (scale bars represent 200 nm, 500 nm, and 500 nm from (a)-(c))

From left to right, the structures shown were fabricated with the goal of creating absorbing nanostructures in progressive longer wavelength regions of the electromagnetic spectrum. Data and simulations are performed using TM-polarized light. Figure 6.6(b) shows the 700 nm period, 9 stack structure from Figure 6.5 using Au-Al_2O_3 stacks targeting short wave IR absorption, assuming a refractive index of Al_2O_3 of n ~ 1.75. To shift the absorption band to the mid-IR, the same period is used to create an 11 stack structure shown in Figure 6.6(c), switching in Ge for the dielectric with refractive index of n ~ 4. While the data and simulation show similar absorption ranges and peak values, simulations show peaks and valleys at shorter wavelengths that are not as strong in the data. We will see later that this is due to the ideal nature of the simulations which allows for cavity resonance modes to be setup at shorter wavelengths.

Finally, Figure 6.6(a) shows how the tapered deposition process can even be applied to BBA structures shorter than 200 nm. The tapered structure shown has a 220 nm period and was fabricated using Al-SiO_2 stacks (SiO_2, n ~ 1.45) to target absorption in the visible regime. In this figure, it should be noted that the black curve uses data from a visible reflection setup with an integrated spectrometer instead of FTIR. The dashed blue curve is taken from angled data obtained using a spectroscopic ellipsometer with source and detector positioned at 45° from normal. This data is included to provide a wider spectral range than the visible reflection setup (which matches pretty well with simulation) and also demonstrates, as discussed below, the high angular tolerance of these nanostructures, showing little variation in absorption between 0° and

45°. This data provides examples of the wide range of features and spectral ranges that can be targeted by this versatile process. Although not shown here, similar methods could be used to shift absorption into the long-IR and THz regimes as well.

The dependence of the absorption spectrum on the incident angle of radiation is important for many applications. Figure 6.7 displays a contour plot showing simulated absorption versus incident angle and wavelength for an 11-stack Au-Ge structure like that shown in Figure 6.6(c).

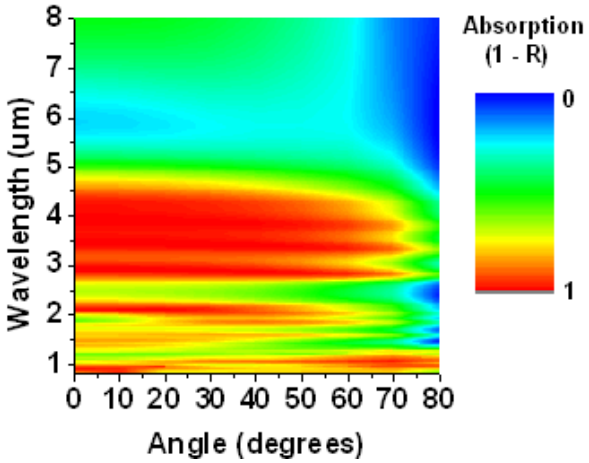

Figure 6.7: Contour plot of absorption versus wavelength and angle demonstrating strong absorption over a wide range of angles. Simulated structure is 11-stack samples with 700 nm period and Ge/Au used for materials, targeting absorption in the mid-wave IR.

Simulations were performed in COMSOL using TM polarized light from 0°-75° and averaged between data points to obtain the plot. Similar to metal-dielectric-metal nanoresonators with localized resonances, high angular tolerance of the primary region of absorption (~3-5 μm) is shown in Figure 6.7. As a further step towards verification of the angle tolerance of BBA stacks, an ellipsometer with measurement range in the visible/near IR up to ~1.6 μm was utilized to take angled reflection data from the 3 stack visible absorption structure shown in Figure 6.6(a). Since the tool is capable of measuring angled reflection over the range of 45°-75°, the comparison between data and simulation, summarized in Figure 6.8, shows a simulated absorption spectrum (a) and a separate plot (b) contains the measured data overlapping the simulated absorption in the 45°-75° range.

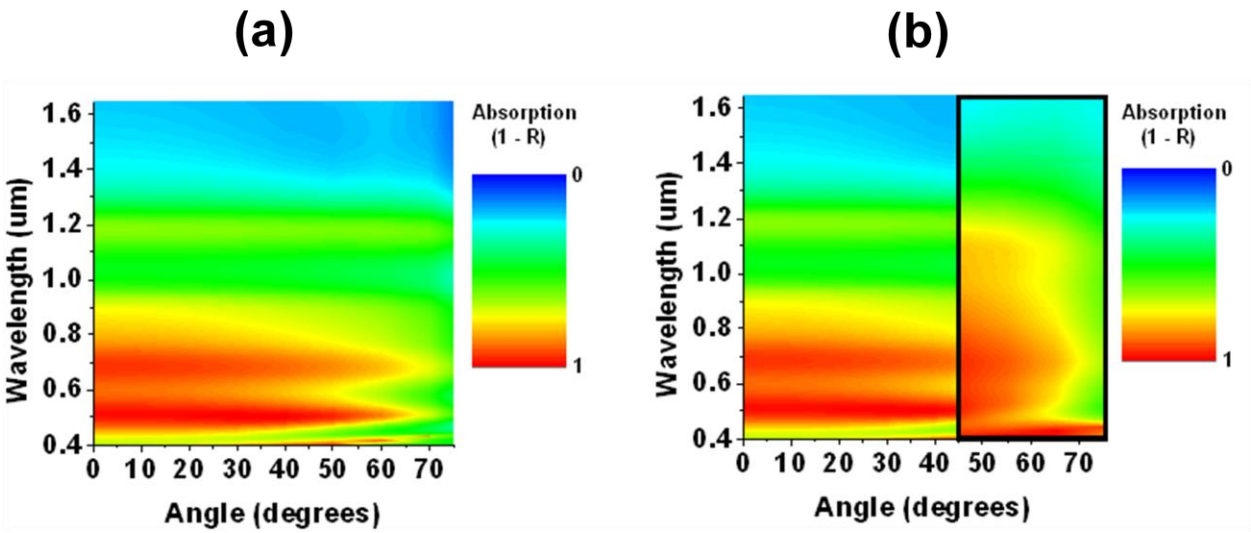

Figure 6.8: Contour plots showing angled absorption data compared with simulation. (a) Contour plot of simulated absorption for 3 stack, SiO_2-Al structure with 220 nm period. (b) Angled data (black box) overlaid on top of simulation plot from the left. Measured data is in the range of 45°-75°.

While the fabricated structure seems to show slightly higher absorption over a wider range of wavelengths than the simulated results, one can still pick out the distinct absorption peaks around 0.5 and 0.7 μm in the data at large angles. As shown in the simulations and agreeing with past results in Ref. [21], the absorption does not show major degradation until angles > 60°. This data provides a first demonstration of the high angle tolerance of BBA stack structures.

6.5 Analysis of HMM cavities

6.5.1 Effective medium simulations

Many papers have been published over the past few years on the topic of light propagation in HMM structures [136-140]. Many of these structures focus on the impressive subwavelength light confinement capabilities of HMMs and their ability to achieve extremely high refractive indices. However, most of these structures are focused on propagation of light in nanostructured waveguide materials with the goal of increased propagation lengths. Similar to the analysis in Chapter 3, it is our goal to effectively absorb light instead of increasing propagation. The analysis presented in this chapter also acknowledges light coupling effects into the structure, which has mainly been neglected in previous HMM works. The references

discussed below are two of the works which report results for HMM nanostructure excitation from the far-field.

In Ref. [21], multilayer metal-dielectric cavities are considered as slow-light waveguides where specific wavelengths slowed as they propagate through the air until their group velocity dips to zero at varying depths within the nanostructured metamaterial, with shorter wavelengths being slowed/absorbed at the top of the structure while longer wavelengths are absorbed after deeper propagation. The work identifies the nanostructures as anisotropic metamaterials using effective medium theory to approximate the ε_{xy} and ε_z permittivity. Similar multilayer metal-dielectric structures are presented in Ref. [22] as nanostructured HMM cavities with strong optical confinement due to the high k-vectors (and therefore, high refractive indices) allowed by the hyperbolic dispersion curve. The fabricated structures showed a good match with simulations despite the slight taper created during the fabrication process (due to a similar fabrication method to that in Section 6.4). The structures also demonstrated anomalous dispersion as predicted by HMM theory and previous works [139], meaning that higher order modes resonate at a longer wavelength instead of a shorter one, as is the case for typical material dispersion.

As would be expected, both of these theories along with those presented in other HMM papers can be used to explain the nature of broadband absorption in these nanostructures. The structures fabricated above and discussed in Ref. [22] are very similar in terms of materials and layer thicknesses, leading one to believe that HMM theory and mode confinement could explain the nature of the absorption and these structures are large enough that the waveguide theory proposed in Ref. [21] can indeed be applied, but the nature of this waveguide can be understood through HMM theory and knowledge of coupling into the structure from free space.

We can begin to analyze these BBA nanostructures by running simulations in COMSOL with effective media calculated by using the Maxwell-Garnet effective medium approximation discussed in Section 6.1. Much like Ref. [21, 22], the effective medium approximation produces nearly identical results for BBA nanostructures compared to those performed with multi-layered metal-dielectric stacks with the same fill ratio as long as the layer thicknesses are highly subwavelength. Since they can be easily fabricated using the methods outlined above, structures with 20 nm of Ag and 30 nm of Ge, for example, could be used to generate the effective medium (fill ratio of 0.4) primarily considered in these simulations, where a low-loss Drude model is used for Ag and a permittivity of $\varepsilon \sim 16$ is used for Ge. According to the effective medium

approximation, Figure 6.9 shows the calculated curves for ε_{xy} and ε_z (where z is the direction of propagation) given these parameters.

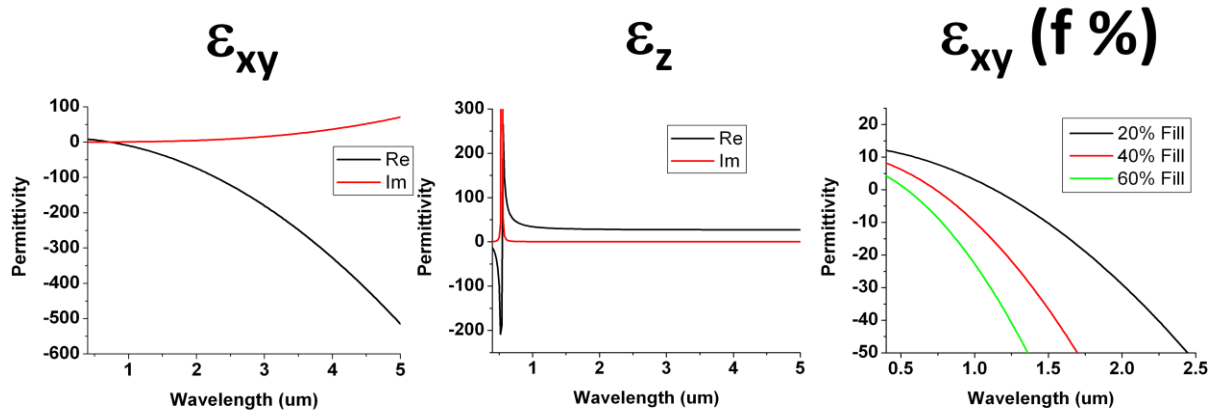

Figure 6.9 Effective medium calculations for Ag-Ge stacked structures showing (a) the effective permittivity (real (black) and imaginary (red) parts) along the direction perpendicular to propagation, (b) the effective permittivity parallel to the propagation direction, and (c) the real part of ε_{xy} for different metal fill ratios.

We can see from the figure that over the designed region of interest (mid-IR), the real part of the permittivity in direction parallel to propagation (ε_z) maintains a relatively constant, positive permittivity while the ε_{xy} dips to larger negative values beginning in the IR, creating a highly anisotropic material. The figure also shows that the effective region of anisotropy can be varied by changing the metal fill ratio. While not shown, lower index dielectrics will also shift the zero point of the Re(ε_{xy}) curve to shorter wavelengths. This will become important for creating BBA in shorter wavelength ranges.

Using these values, we can easily simulate many kinds of tapered BBA structures assuming they are anisotropic materials with ε_{xy} and ε_z shown above to discuss their properties in terms of HMM theory. For most simulations, a fill ratio of 0.4 is assumed and low-loss (low γ) Ag will be used for the study. However, to show the good match between simulations for MIM stacks and effective media, a higher loss Ag is assumed so we can compare with our measured results. Figure 6.10 below shows a simulated 700 nm period BBA structure made of MIM stacks along with the effective medium structure. 900 nm height, 500 nm base, and a sidewall slope of approximately 80° are used, similar to the structure in Figure 6.6(c), but using a Drude model for

Ag with lower loss. Incident light from free-space was assumed to have transverse magnetic (TM) polarization with the magnetic field in the y direction.

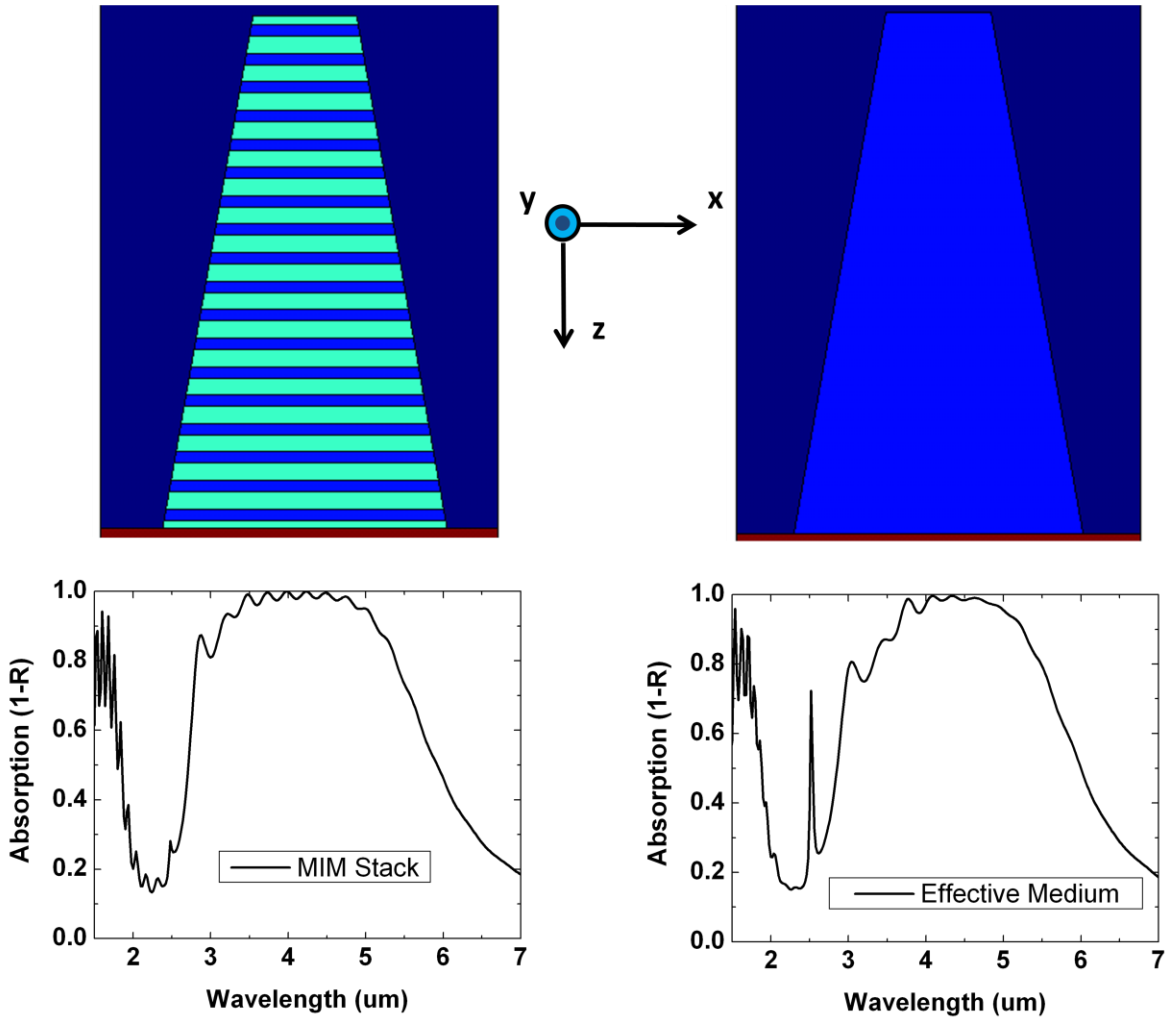

Figure 6.10 Effective medium vs. MIM stack simulations of BBA nanostructures with 700 nm period, 500 nm base width, 900 nm height, and 40% metal fill ratio. On the left, a diagram showing the metal-dielectric stack structure (20 nm Ag (blue), 30 nm Ge (light blue) in air (dark blue) on an Al substrate (red) and the absorption spectrum. On the right, a diagram and plot for an effective medium with the same fill ratio and Ag / Ge optical properties.

We can see that the effective medium approximation pretty accurately predicts the spectrum from the MIM stack simulation. If thinner Ag/Ge layers are used in the stack simulation (keeping the same fill %), a better match is achieved, but these structures can be much more difficult to fabricate. The stack simulation shows that loss is also effectively increased since light is absorbed well over the full band from 3-5 μm while the effective medium shows less absorption

in the 3-3.5 μm range. Also, there is a sharp resonant peak just above 2.5 μm that is present in the effective medium case that will be discussed later in future works (Chapter 7).

Figure 6.11 shows magnetic field profile simulations along with a comparison between effective media simulations for BBA nanostructures assuming a low loss Drude model for Ag or a higher loss model. The higher loss model actually more closely approximates parameters achieved in experiments such as Ref. [48, 49] for deposited Ag. We will see that the lower loss model is useful for highlighting properties in the HMM nanostructures, but that typical Ag with higher loss actually improves BBA capabilities, and yields similar results to the stack simulation shown in Figure 6.10.

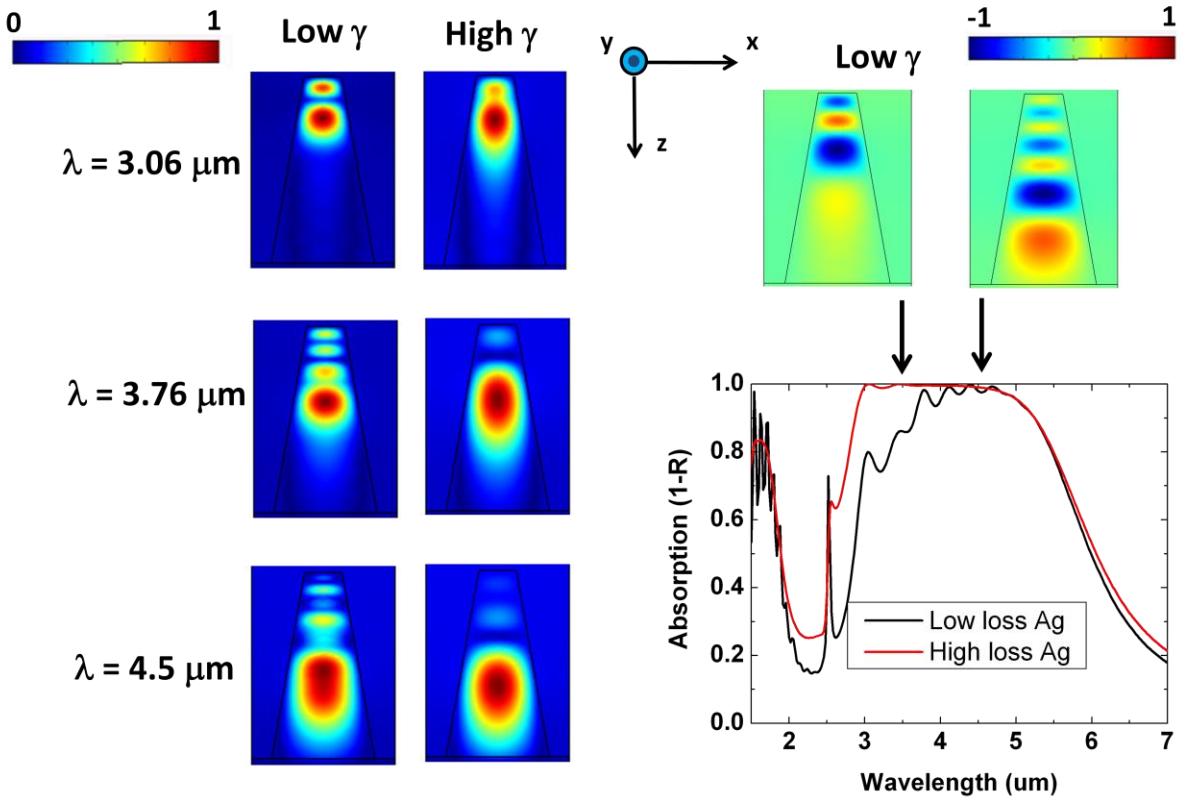

Figure 6.11 Effective medium simulations of BBA nanostructures with 700 nm period, 500 nm base width, 900 nm height, and 40% metal fill ratio. On the left, 6 profiles showing the normalized H_y at 3 different wavelengths given two media with low or high loss (γ) Ag assumed. Low-loss and high-loss absorption spectra are shown on the bottom right. Field profile simulations on the top right show non-normalized H_y at two wavelengths (3.5 μm and 4.5 μm).

We can begin by noticing that the normalized H_y profiles and high γ Ag spectrum are very similar to the results obtained in Ref. [21], although over a slightly different wavelength

range due to changes in the feature sizes. High absorption is obtained over a large band from 3-5 μm and normalized fields show large enhancement at deeper parts of the structure for longer wavelengths. When looking at the low γ results, however, we begin to see that the broad response degrades into small peaks in absorption (including the very sharp peak above 2.5 μm that will be investigated in future work) and that multiple nodes are seen in the field profiles. We can also see that the amount of nodes grows with increasing wavelength, suggesting higher order modes at larger λ values like the HMM cavities in Ref. [22].

Unlike the work presented in Ref. [21], the simulations above and presented below suggest that light propagates within the HMM after being coupled in at a certain depth. When loss is reduced in the material, the wave may continue to propagate and absorption will become governed by the intrinsic properties of the HMM nanostructure. The next section discusses the propagation inside of the tapered metal-dielectric structure, relating the results to propagations in a HMM waveguide.

6.5.2 Propagation in HMM waveguide

The next figure shows field profile simulation results demonstrating the unique power and phase propagation in the HMM waveguide structure when coupled from free space. It includes H_y plots that show that the nodes seen in Figure 6.11 are propagating in the +z direction and that absorption is not merely due to pure cavity modes as would be suggested by the results in Ref. [22] for smaller cavities. Finally, time averaged power flow simulations show that power flow is in the reverse (-z) direction. These results are shown in Figure 6.12.

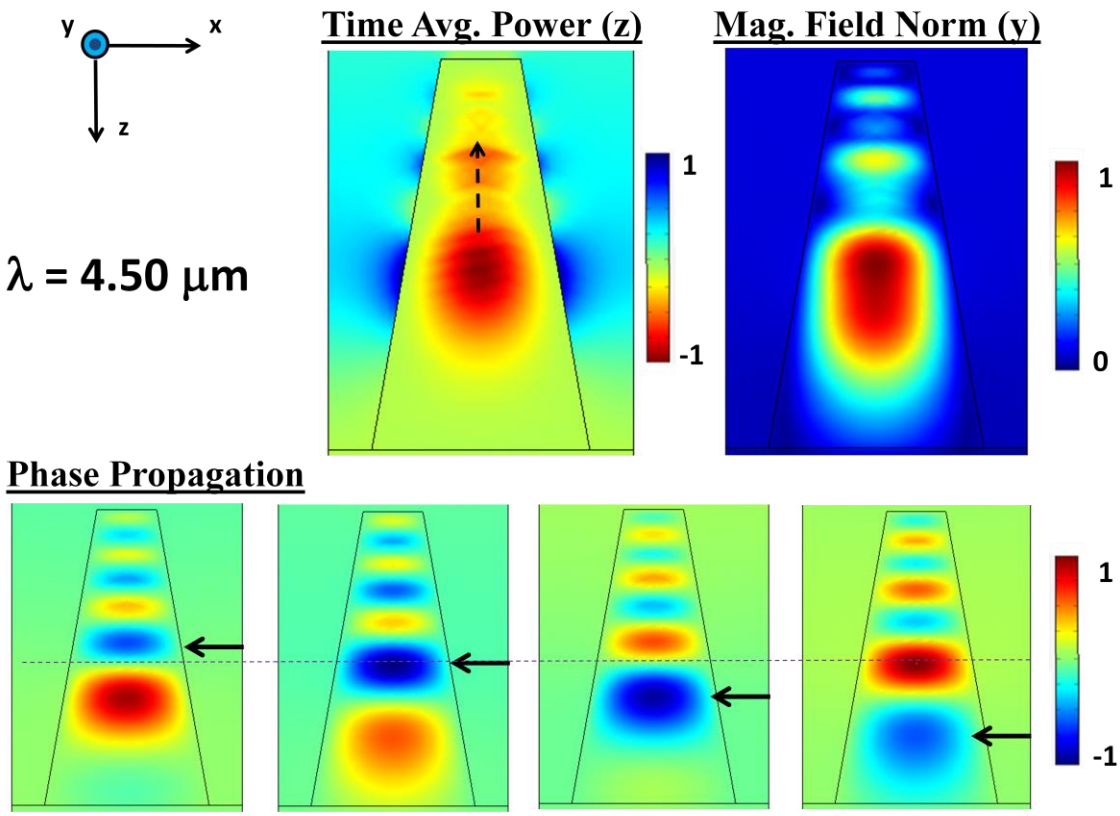

Figure 6.12 COMSOL field profile simulations at λ = 4.50 μm. The top right plot shows the normalized H_y, as in Figure 6.11. The time averaged power flow for the z-direction is also shown on top in the middle. The phase propagation (with arrows following a single node) is shown below. The field profiles highlight that phase propagation opposes power propagation within the waveguide.

We can also see that the strongest magnetic field (dark spots in red or blue nodes) appear at approximately the same width / depth in the structure, as predicted by the normalized H_y plots for a given wavelength. These results highlight the opposing power flow and phase propagation that is indicative of highly anisotropic metamaterials. However, opposing phase and power does not explain why power flows inside of the structure against the direction of the incoming wave in free space. In NIMs, power flow still occurs along the same direction in free-space while the phase propagation reverses direction.

This brings up the question of the nature of light coupling into this structure. In Ref. [21], light propagates around the HMM structure in air until a certain depth before being absorbed. From Figure 6.9, we can see that the permittivity along the z propagation direction of the effective medium is much higher than free-space (ε ~ 27) in the IR, suggesting that most light would be reflected from the interface before it could be coupled in at a certain point. Research

into waveguide modes of anistropic materials seems to have confirmed this, stating that light propagating into a tapered metamaterial structure would be reflected due to mode coupling between competing forward and backward propagating modes [130]. Since the results from the previous sections clearly demonstrate that the majority of light is absorbed and that power flow is in the –z direction, the question then becomes how light is so effectively coupled into the structure from free-space. The answer comes by remembering that our effective media are stacks of MIM resonators and, from Chapter 4, we remember that light can be easily coupled into MIM structures of a certain size / width [55, 141, 142]. Furthermore, these structures contain high angle tolerance, effectively "funneling" light into the MIM resonator from a wide range of angles / wave vectors, explaining the angle tolerance properties shown above in data and simulation. It is shown below that light can be coupled into the structure along its entire depth, but primarily at a certain width depending on the incoming wavelength, similar to what one would expect for stacks of MIM resonators with varying widths.

By applying HMM theory and assuming that most light coupling into the structure occurs at a specific width deeper within the structure, it becomes easier to understand how BBA can be achieved in these cavities with the power and phase propagation presented above. Figure 6.13 shows a plot of a HMM isofrequency curve according to effective medium theory to illustrate the effect of tapering on the nanocavities.

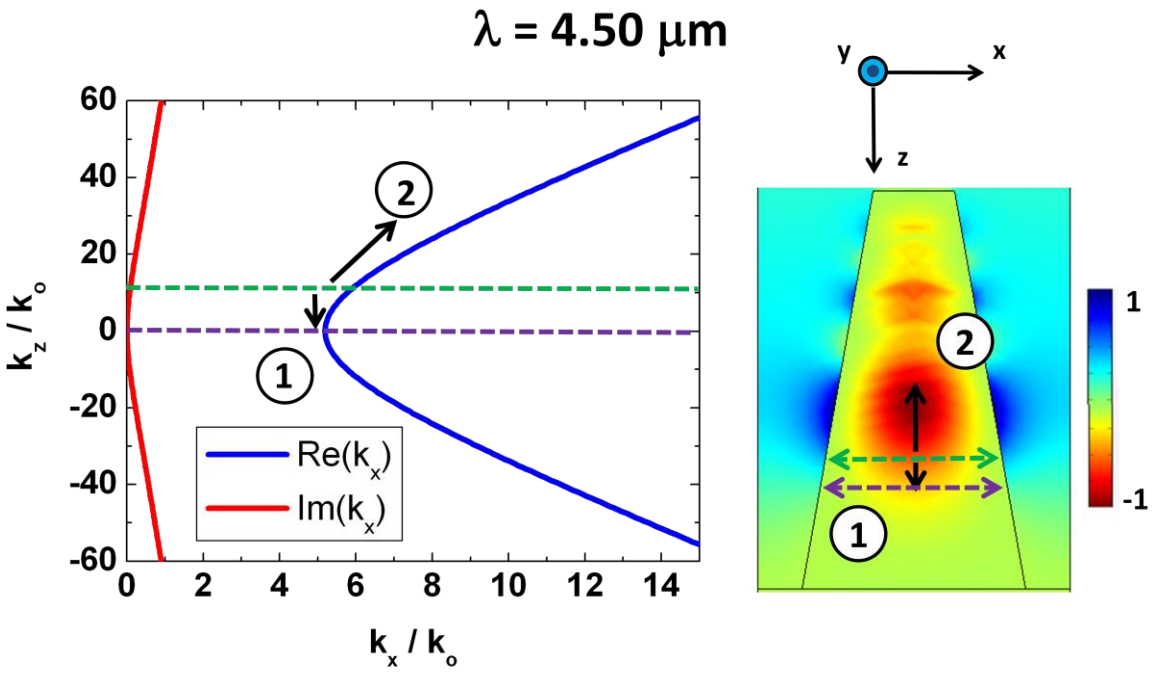

Figure 6.13 Figure showing example of isofreqency curve (Re(k_x) and Im(k_x) vs. k_z) normalized to k_o for λ = 4.5 μm calculated using effective medium and the hyperbolic dispersion relation (shown below). The dashed green line could represent a coupling into the HMM medium while the numbers 1 and 2 represent propagation towards or away from the k_x=0 point (purple line). On the right, the coupling and k_x=0 points are labeled over the time averaged power flow field profile from Figure 6.12.

The red and blue curves plotted on the left in Figure 6.13 do not take the tapered nanostructure into account. This is a plot generated from the dispersion equation with ε_{xy}, ε_z, and ω given by effective medium theory and the chosen wavelength (4.5 μm).

$$\frac{k_{xy}^2}{\varepsilon_z} + \frac{k_z^2}{\varepsilon_{xy}} = \frac{\omega^2}{c^2}$$

The effect of the nanostructure can be seen try tracing along the blue curve as we progress through the structure, assuming that light is coupled in at some specific width. A simple Fabry-Perot resonant equation (as outlined in the supplement of Ref. [22]) can estimate the k_x value given a certain width (or vice versa). Since the round trip phase should be equal, $2k_xL_x$ should be equal to $2m_x\pi$, where k_x and L_x represent the wave vector and width in the x direction while m_x is an integer value determining the number of nodes. Assuming m_x=1 (in this region,

we can see from COMSOL simulations that magnetic fields show no nodes in the x-direction), then $k_x/k_o = \lambda_o/2L_x$.

Assuming that light is coupled in at a point represented by the dashed green line, if phase propagation occurs in the +z direction (toward (1)), larger widths and, therefore, smaller k_x values are tolerated. It can be seen from the curve that only a small change in k_x (or width) will lead to the point where $k_z=0$ (k_x~5.2, shown with dashed purple line) and phase fronts will become evanescent in the +z direction. If our nanostructure was an isotropic, or not an indefinite, material and had ε_{xy}, $\varepsilon_z > 0$, a decrease in k_x would need to be accompanied by an increase in k_z to stay on the same frequency curve. The opposite is true for a HMM since $\varepsilon_{xy} < 0$ and $\varepsilon_z > 0$. Power flow preferentially occurs in the –z direction (toward (2)) towards larger k_x and k_z values, however, the Im(k_x) is also increasing with larger k_x, k_z, so light is not able to achieve a standing wave resonance. Furthermore, when Ag has a higher loss closer to experimental values, power becomes attenuated even faster in the –z direction.

This result is similar to that predicted in Ref. [21] with a few key changes. Ref. [21] essentially uses the (k_x, k_z)=(5.2, 0) point to predict the width where strong absorption occurs. Plugging this into the Fabry-Perot equation above for λ_o = 4.5 μm yields a width of approximately L_x ~ 433 nm, but both Ref. [21] and the above results show a narrower width where the strongest field occurs. Furthermore, the equation can overestimate the range of wavelengths which can be absorbed. The width of the structure varies from ~180 nm – 500 nm for the structure in Figure 6.11. This would predict absorption ranging from λ_o ~1.87 – 5.20 μm, while the strongest absorption of the actual structure ranges from ~3 – 5 μm, and little absorption occurs from λ_o ~ 2 – 2.5 μm. This is because the work is assuming that waves are propagating until the waveguide slows the light down to a group velocity of zero. As mentioned above, the power flow and HMM curve shows that waves cannot couple in well from the top of the structure. To enter the top of the structure, the light would have to vertically couple into the small width / large k portion of the waveguide. The large k_x and k_z values suggest very high refractive indices and the loss in the structure may be higher at these values, as shown by the Im(k_x) plot. If light is coupled into the structure at various widths / depths dependent on the wavelength and continues to propagate with reverse phase and power flow, not only does this explain the power propagation in –z direction, but it also shows that field enhancement (and not necessarily absorption) would occur at a slightly shallower depth above the k_z = 0 point

(narrower width) as shown in our COMSOL field profiles as well as in Ref. [21]. Unlike Ref. [21], this theory also predicts that shorter wavelengths with $m_x = 3$ (3 H_y nodes in the x-direction), for example, will also be absorbed by our structure. This can be confirmed in Figure 6.11 which shows another strong absorption band at wavelengths of approximately 1.5 μm – 2 μm, corresponding to the $m_x = 3$ modes. The gap in absorption from $\lambda_o \sim 2 – 2.5$ μm is the absence of the $m_x = 2$ modes since only odd modes can be excited in MIM structures at 0° incident angle due to the symmetric magnetic field at both ends of the resonator.

Returning to absorbed wavelengths where $m_x=1$, to confirm that longer wavelengths are coupled in at deeper points in the structure (or large L_x values), we can look at the isofrequency plots in Figure 6.14 for the 3 wavelengths absorbed by the structure presented in Figure 6.11.

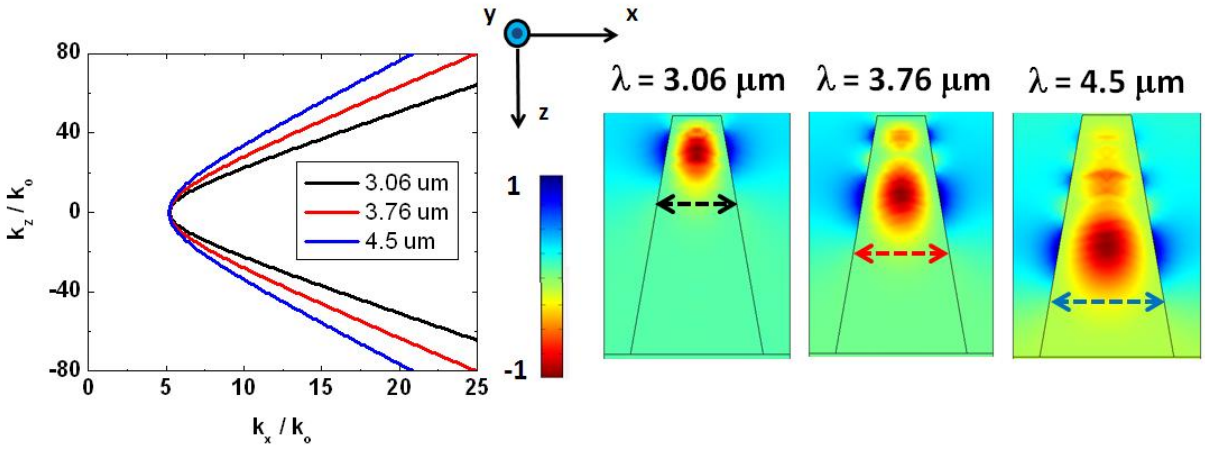

Figure 6.14 Figure showing example of hyperbolic k-space curves (k_x, k_z) normalized to k_o for λ = 3.06. 3.76, and 4.5 μm calculated using effective medium and the hyperbolic dispersion relation. Dashed lines in nanostructure reflect the point calculated using $k_x \sim 5.2$ when $k_z=0$.

Although the $k_z = 0$ point discussed above does not accurately represent the location of absorption as predicted by Ref. [21], it can be used to show the point below where power flow occurs in the –z direction and, therefore, give an estimate of the coupling point. Since the k_x values where $k_z = 0$ are nearly identical, according to the $k_x/k_o = \lambda_o/2L_x$ equation, this means that the width (L_x) where $k_z = 0$ is linearly related to the wavelength. The time averaged power flow plots for the z direction each have the calculated width where $k_z = 0$ labeled with a colored, dashed line. These lines clearly represent the point where power propagates in the –z direction, suggesting that the coupling point must occur above this width. As we will discuss later, this can also lead to the formation of an effective cavity for light confinement.

6.5.3 Designing the BBA

Knowing that the new coupling and HMM theory can better explain the field profiles and power propagation presented above, we can begin to explain the optimization of the BBA structure. The bunching of the k-space curves near the $k_z = 0$ point also helps to describe the desired structure for the BBA and why an ideal height and base width are essential for defining the absorption band and strength, but the sidewall angle also becomes important. The discussion below will also include the concept of cavity modes. In large tapered HMMs, longer wavelengths couple near the bottom where a large range of k_x and k_z values are allowed, but as light couples in closer to the top and the confinement becomes smaller in both the x and/or z directions, k_x and k_z are confined to larger values, leading to singular resonant absorption peaks like those described in Ref. [22].

We can begin to analyze ideal BBAs by looking at the effect of the height with a constant sidewall angle and base width, shown in Figure 6.15.

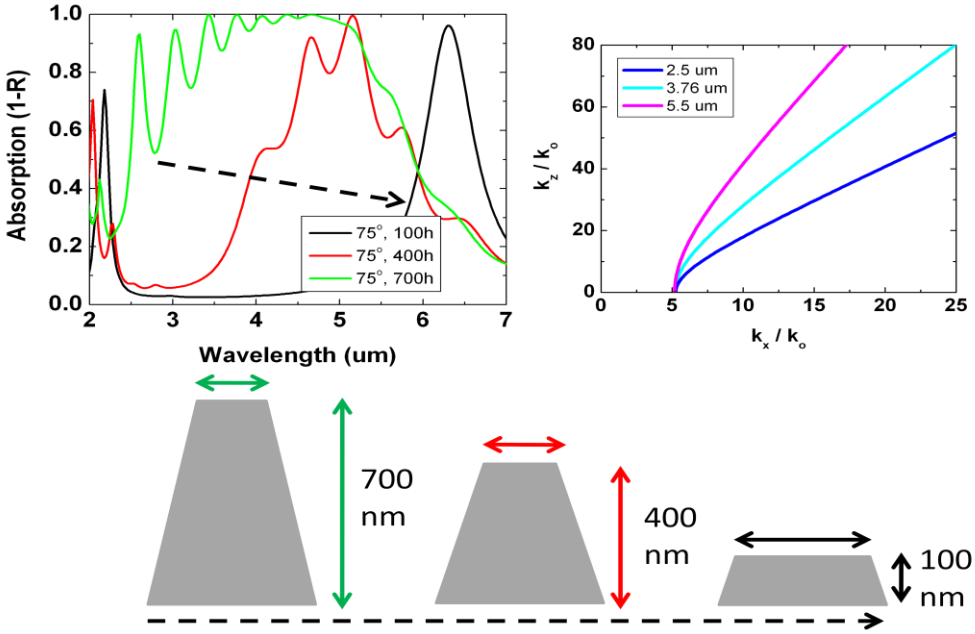

Figure 6.15 Figure demonstrating the effect of height change with constant sidewall angle (75°) and base width (bottom) on the absorption spectrum (top left). Hyperbolic isofrequency curves for 3 wavelengths are plotted in the top right.

When the structure height is 100 nm, it approximates the absorption profile of a single MIM resonator cavity. As mentioned above, the z confinement limits the coupled light to very high k_z values while k_x is comparatively smaller. As shown in the isofrequency curves in the top right,

longer wavelengths are required to satisfy the conditions for larger k_z and small k_x values, hence the absorption peak of λ_o ~6.5 μm shown. When the height is increased, a more broadband profile begins to form. For example, the increase in height from 100 nm to 400 nm with a constant sidewall angle (75°) means that the top width will change from ~450 nm to ~285 nm, allowing the structure to couple in light at shorter wavelengths. The 700 nm height improves the BBA, however, as demonstrated from the power flow profiles above, wavelengths absorbed near the top of the structure (shorter λ) are confined to smaller areas with higher k_x and k_z values (and higher effective index), once again causing cavity resonance peaks to begin to form. Like Ref. [22], resonances at longer wavelengths have more nodes, demonstrating an anomalous dispersion. At non-resonant wavelengths, light can still propagate in the structure and will be absorbed due to loss mechanisms similar to longer wavelengths, but the proximity to the top allows some of the power to be coupled out of the structure, leading to the dips in absorption between the resonance peaks.

This simultaneous k_x and k_z constraint puts more of a limit on the minimum width where absorption can effectively occur and explains why smaller L_x values are not the sole variable in determining effective absorption. This confinement rule also explains the sharp resonance peak seen in Figures 6.10 and 6.11, corresponding to a $(m_x, m_z) = (1, 1)$ resonance with a much sharper bandwidth. It's possible that this resonance could be used for plasmonic sensing applications, but Figure 6.10 also showed that this resonance tends to disappear for structures with non-ideal metal parameters. The distinct cavity resonance peaks are also not visible for non-ideal metals due to the increased loss in the structure reducing the chances of power being coupled out at shorter wavelengths.

The figure above demonstrated that taller structures are needed to absorb over a wider wavelength range before cavity resonances begin to alter the profile. It then becomes apparent that, given a certain height, the sidewall angle would affect the range of widths available for coupling. Naturally, smaller sidewall angles would lead to a wider variation in L_x, allowing light of shorter wavelengths to couple into the structure, but they would also lead to more discrete absorption peaks due to cavity modes. Larger angles would limit the coupling range of the structure unless the height is increased to > 1 μm. This is summarized in Figure 6.16.

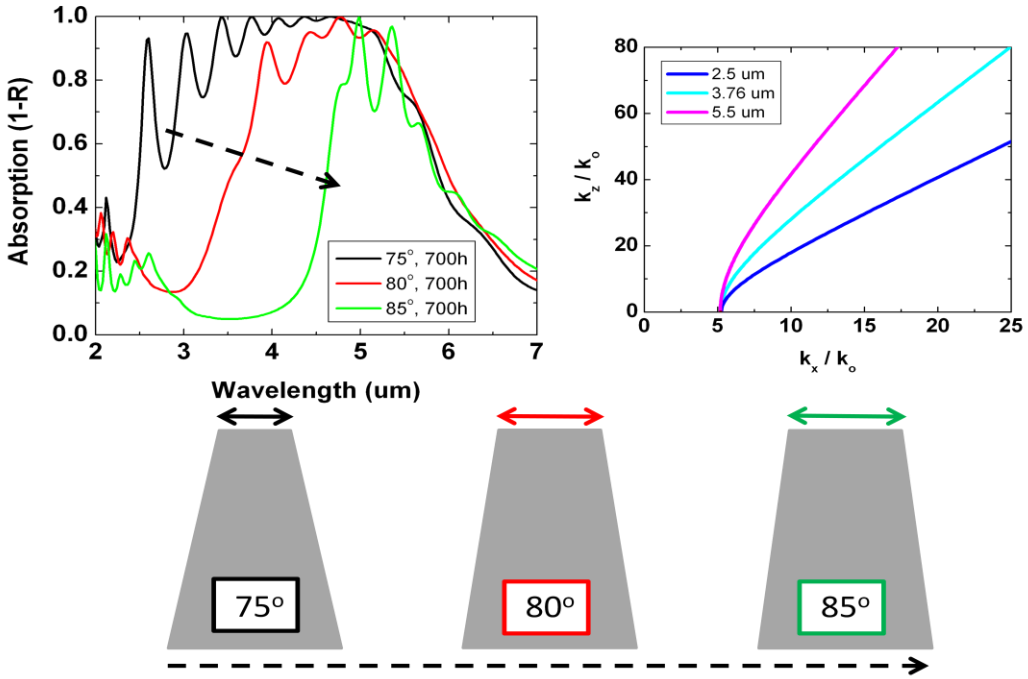

Figure 6.16 Figure demonstrating the effect of sidewall angle change with constant height (700 nm) and base width (bottom) on the absorption spectrum (top left). Hyperbolic isofrequency curves over for 3 wavelengths are plotted in the top right.

The absorption spectra plotted in the top left of Figure 6.16 demonstrate that a steeper sidewall angle can indeed lead to a wider range of absorption when the base width and height are held constant. Once again, since the 75° structure is the same as Figure 6.15, shorter wavelengths can be absorbed, but discrete cavity resonances begin to appear. The 80° sidewall structure now achieves much better BBA absorption that the 75° sidewall structure with a 400 nm height over the same range, despite having very similar top and bottom widths. When the sidewall angle is increased to 85°, the absorption range decreases and cavity modes immediately appear. A large increase in k_z (decrease in L_z) is needed to affect a small change in k_x (decrease in L_x), leading to a large variation in cavity size for a small change in wavelength.

Based off of the work performed in Ref. [21], one may conclude that the range of widths within the structure completely determines the absorption throughout. This would mean that shorter structures with the same range of widths (only the height and sidewall angle vary) would produce similar absorption spectra. From our results above, we know that shorter heights can lead to more discrete absorption profiles, but there is also an effect on the magnitude of absorption. Results of a simulation demonstrating this property are shown below in Figure 6.17.

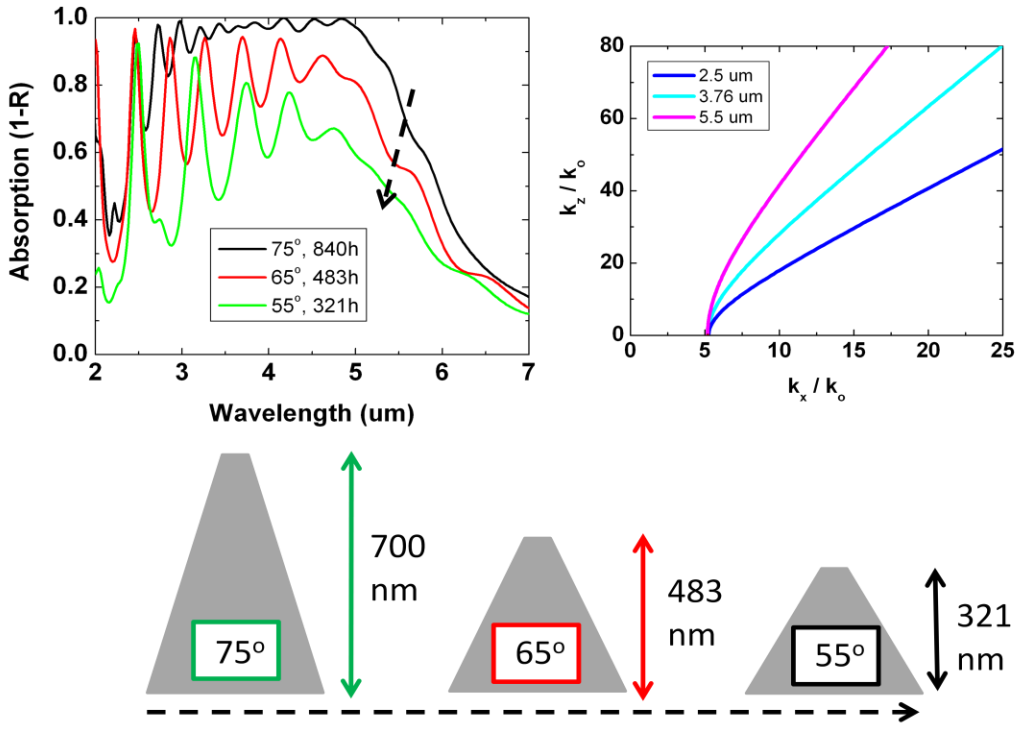

Figure 6.17 Figure demonstrating the effect of sidewall angle change with constant top (50 nm) and base width (500 nm) on the absorption spectrum (top left). Hyperbolic isofrequency curves over for 3 wavelengths are plotted in the top right.

Profiles were chosen where L_x varied from 500 nm to 50 nm in all structures. It is easy to see the resonances becoming more discrete for structures with shallow heights and steeper sidewall angles while the overall range of absorption stays relatively constant. There is also an overall decrease in the magnitude of absorption, particularly at longer wavelengths. Ref. [21] demonstrated that the metal base plane can actually increase absorption since reflected light can couple into the structure for absorption, but the substrate can also interfere with the effective cavity confinement for longer wavelengths and increase reflection. It is also interesting to note that the cavity mode at the shortest wavelength (~ 2.5 μm) stays relatively stable, suggesting that steeper tapers can provide more discrete confinement of short wavelengths.

Finally, we can discuss the ability to shift BBA to other wavelength ranges (into the short-wave IR, for example). As discussed above, a taller structure with a narrower top width can achieve absorption at shorter wavelengths, but the cavity modes that form lead to discrete, rather than broadband, absorption. Increasing the metal loss in the structure can solve this issue, but structures will need to be > 1 μm in height to achieve absorption over the entire short and mid

IR. Furthermore, the spacing between the periodic MIM resonators with smaller L_x is continuously growing with taller structures, limiting the % of light that can be effectively coupled in. If we wish to achieve a BBA in only the NIR, we have the choice of shrinking the nanostructure (and periodicity) or keeping similar feature sizes while changing the effective medium by altering the filling material from Ge (ε ~ 16) to a lower permittivity material (ε ~ 4). Figure 6.18 summarizes simulations targeting absorption in the short wave IR.

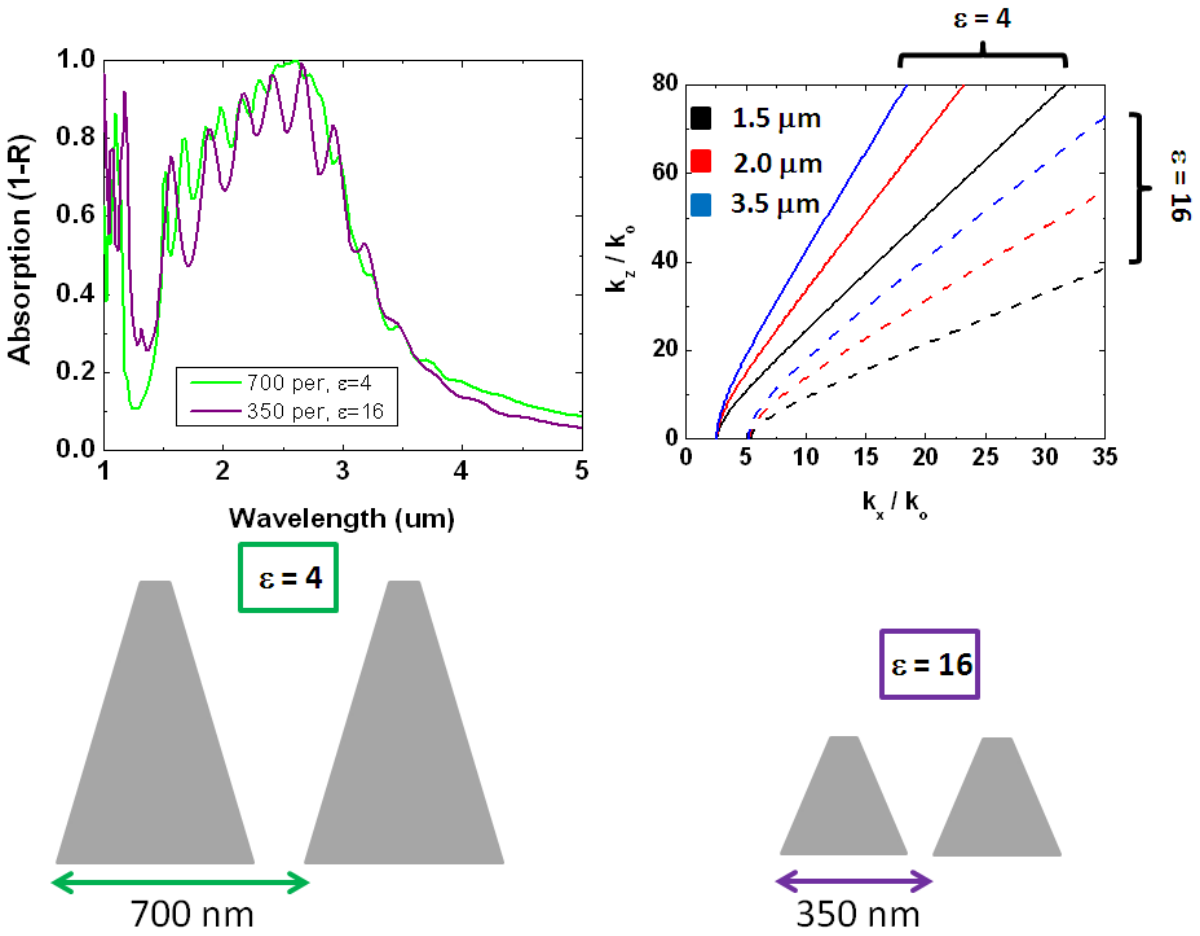

Figure 6.18 Figure demonstrating two structures for absorption in the short IR. One replaces Ge with Al_2O_3 (ε ~ 4), maintaining similar geometrical parameters (bottom left) while the other uses the same effective medium and feature sizes are decreased (bottom right). Absorption spectra show similar ranges of absorption with varying degrees of cavity confinement (top left). Hyperbolic isofrequency curves over for 3 short IR wavelengths are plotted in the top right.

This figure shows that effective BBA in the short wave IR can be achieved either through feature size reduction or change of the effective medium. Isofrequency curves for short IR wavelengths and fill materials (ε = 4 and ε = 16) are shown in the top right, demonstrating that smaller

structures with higher index fill materials will form more discrete resonances at shorter wavelengths than larger structures with a lower index. The absorption curves for two structures are plotted in the top left. The first structure has a 700 nm period, 900 nm height structure with a 75° sidewall angle and the same fill % and base width of previous results, but the fill material in the effective medium is decreased to $\varepsilon = 4$ (bottom left). The second structure uses the same Ag-Ge effective medium as above, but it now has a 350 nm period, 380 nm height, 250 nm base width and a 75° sidewall angle. Both structures effectively absorb over the same region, but as expected from our results above, the smaller Ag-Ge structures form more defined cavity resonances since they are operating on isofrequency curves with more discrete spacing between (k_x, k_z) points.

6.6 Conclusion

Broadband absorbing nanostructures were fabricated over large areas using nanoimprint lithography. Absorption was demonstrated in the visible, short IR, and mid IR and a high degree of angle tolerance was demonstrated in data and simulation. While simulations have shown similar structures acting as broadband absorbers in the past, this analysis provides better understanding by: a.) discussing dimensional limitations including height, width, and sidewall angle for effective absorption b.) addressing coupling efficiency from the far-field over a wide range of wavelengths c.) analyzing light propagation within the medium and explaining inconsistencies in previous studies regarding power flow. Through extensive analysis of simulations, it was shown that the tapered stacks of metal-dielectric layers can be approximated as a nanostructured hyperbolic metamaterial. The light can effectively couple into the medium at various widths / depths as would be expected since the medium approximates a stack of MIM resonators, and power is absorbed or confined within due to the high wave vectors / refractive indices present in HMMs.

This work could open up new avenues of research into the propagation of light through HMMs. Experimentation with newly researched plasmonic materials can be pursued to generate low-loss structures with properties outside of those found in nature. One example in particular will be discussed in the final section where a new structure with a sharp resonance could be used as a plasmonic sensor or generate high field confinement for taking advantage of nonlinear effects.

Chapter 7
Conclusion

7.1 Summary

In this dissertation, nanoscale waveguide structures were utilized to filter specific frequency bands over a variety of spectral ranges. Improved fabrication capabilities and understanding of optical phenomena led to research for a wide range of applications including UV suppression, color filtering, and broadband IR absorption. Structures were created over large areas with reproducible steps that could be applied to larger scale industrial manufacturing.

In Chapter 2, nanoimprint lithography was used to fabricate some of the highest aspect-ratio Si nanostructures reported in literature created by deep reactive ion etching. By refining recipes in advanced processing equipment, large area fabrication of structures with ~60:1 aspect ratio were presented. High aspect-ratio Si nanowall structures were also researched as potential candidates for Li ion battery electrodes. These methods were further used to improve UV filtering capabilities of free-standing Si nanogratings used in space-based particle sensors. The optical properties of these nanogratings were accessed in Chapter 3, showing that the trenches between the gratings can be approximated as lossy, nanoscale, metal-insulator-metal waveguides. Results for gratings with atomic layer deposition coatings were presented, demonstrating greatly enhanced UV/visible suppression while allowing a sufficient rate of particle transmission for measurement. Along with a better particle to UV ratio, the increased stability of the Si nanostructures and ease of fabrication could make them useful for many future space missions.

In Chapters 4 and 5, nanoscale waveguides were used to filter specific frequency bands in the visible spectrum. In Chapter 4, waveguides were presented where light of a chosen band is well-confined and absorbed within the structure. This band could be easily manipulated by changing the grating period. A new method of fabricating a large-scale reflective color filter using multilayer pattern transfer lithography was presented. Specifically, a filter where blue light was well absorbed to create a complementary yellow color with high angle tolerance was

demonstrated on a flexible substrate, making it a candidate for reflective display technologies. In Chapter 5, nanoscale dielectric waveguides coupled with grating resonances were used to create transmission color filters with impressive transmission efficiency of ~90% that can be controlled by selecting the period of the grating. Red and blue color filters were fabricated over large areas, with the red reaching its peak theoretical efficiency. Furthermore, the bandwidth of the resulting spectrum was controlled through a simple layer thickness variation, making the structures useful for sensing applications.

In Chapter 6, multilayered, tapered stacks of metal-insulator layers were fabricated over large areas to demonstrate broadband absorption. When these layers are highly subwavelength in thickness, each stack can be approximated as a waveguide with properties determined by effective medium theory. Various structures were fabricated over large areas to demonstrate broadband absorption in the visible, near IR, and mid IR regimes using a simple process where tapering is created due to lateral growth during evaporation. The broadband absorption capabilities are demonstrated to be properties of the hyperbolic dispersion of the effective medium. Light can be effectively coupled into various widths / depths of the structure over a wide range of wavelengths and effectively absorbed through a combination of material losses and cavity resonances. Further understanding and control of the effective medium properties could lead to interesting applications in defense applications or thermo-photovoltaics.

7.2 Future work

7.2.1 Si as a plasmonic material in the UV

In Chapter 3, the measured optical constants of Si were investigated in the UV regime, showing that Si has more metallic properties in this range due to a high plasma frequency. With recent advances in fabrication and the lack of plasmonic materials in the UV region, Si could be useful as a semi-metallic material for applications where higher loss may be tolerated. In Chapter 3, a reverse polarization effect was observed in free-standing Si gratings, with TE polarized light being transmitted at a much higher percentage than TM. An Al grid structure with a period closer to the effective wavelength demonstrated a reverse polarization effect in Ref. [6]. This is in contrast with traditional wire grid polarizers which reflect TE and pass TM. While wire grid structures have been proposed for UV wavelengths, the subwavelength periods of these polarizers make them much more difficult to fabricate for deep UV applications. With the

semiconductor industry transitioning towards shorter wavelengths for photolithography, new optical structures in this range such as polarizers may become very useful if a cheap, effective material and fabrication method can be realized. These structures could also find applications in other space-based applications if polarized UV measurements are required.

Running simulations in COMSOL for Si gratings with various period, depths, and duty cycles shows that high aspect-ratio Si gratings could be used as polarizers with high TE:TM transmission ratios for a variety of important wavelengths. For example, simulated structures with 240 nm period and 2 μm depth (very similar to those fabricated in Chapter 2 and 3) but narrow line widths of approximately 70 nm could produce TE:TM ratios of approximately 50 or much larger for wavelengths in the deep UV. These include ~121 nm (Ly-α emission from the Sun) as well as 157 nm and 193 nm (used in photolithography) wavelengths. Figure 7.1 displays the TE and TM transmission and highlights areas where TE:TM ratios >50 exist in simulation.

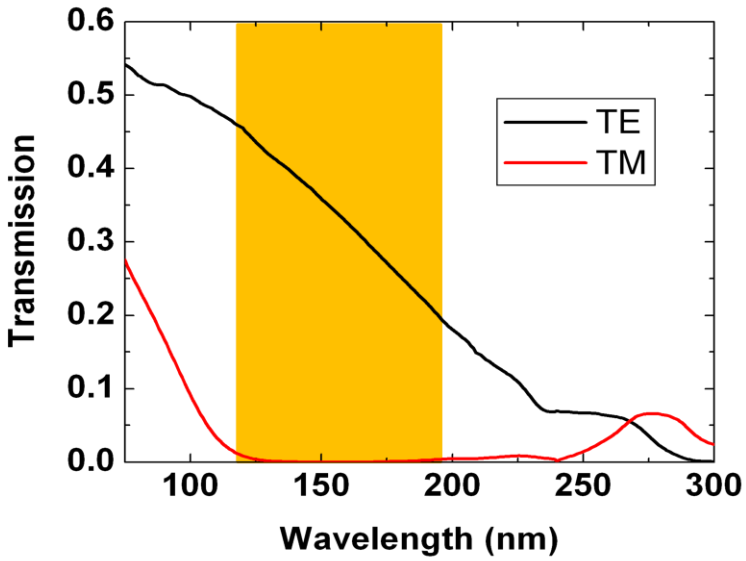

Figure 7.1 TE and TM polarized transmission through 240 nm period, 2 mm deep, 70 nm linewidth Si nanograting structure. Yellow region shows area where TE:TM extinction ratio is greater than 50.

These structures utilize the lossy, plasmonic TM modes to absorb light while the TE modes are passed relatively well as waveguide modes. This is just one example of utilizing Si as a plasmonic material at deep UV wavelengths. Applications in sensing and metamaterials could also be interesting to investigate.

7.2.2 High aspect ratio Si and ALD for photonics applications

In recent years, various high aspect ratio structures have been investigated for photonics applications. Two related examples have been light-funneling nanoslit structures with high coupling and absorption efficiency and annular aperture arrays [80, 113, 114]. Both structures have been proposed for applications such as color filters, field enhancement structures for non-linear optics, or solar cells. Example diagrams of both structures are given below in Figure 7.2.

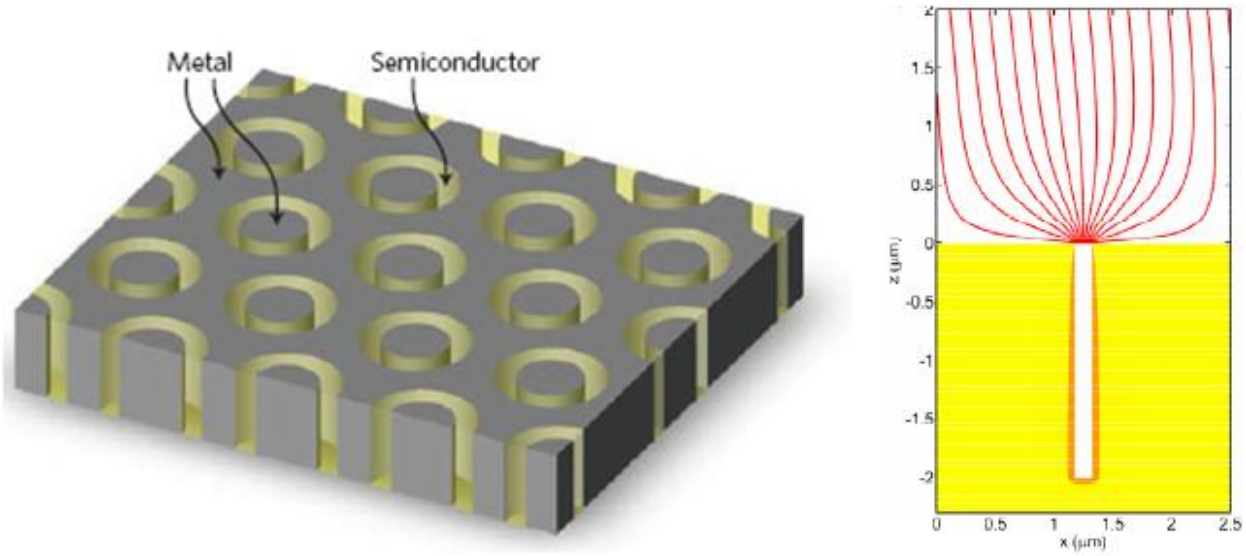

Figure 7.2 Example figures from papers demonstrating annular aperture arrays (left) [143] and light funneling nanoslit structures (right) [113].

Fabricating high aspect-ratio metallic structures over large areas has proven to be difficult. Previous fabricated structures were typically created using focused ion beam lithography and not applicable for large area applications. Etching methods are also typically not possible for such high aspect-ratio metals, but Si structures can be easily fabricated with the dimensions required and used as templates. Atomic layer deposition (ALD) on Si membranes was used to narrow holes for filtration applications [37] but, as seen in Chapters 2 and 3, ALD can be used to deposit metals such as Pt as well. This allows Si to act as a high aspect-ratio template for plasmonic applications since nanoslits and annular aperture arrays can be generated over large areas much easier than other methods. An example of an attempt to fabricate an array 700 nm period, ~2 μm deep Si nanoslits coated with Pt, creating trench widths < 100 nm, for light funneling applications in the infrared is shown in Figure 7.3.

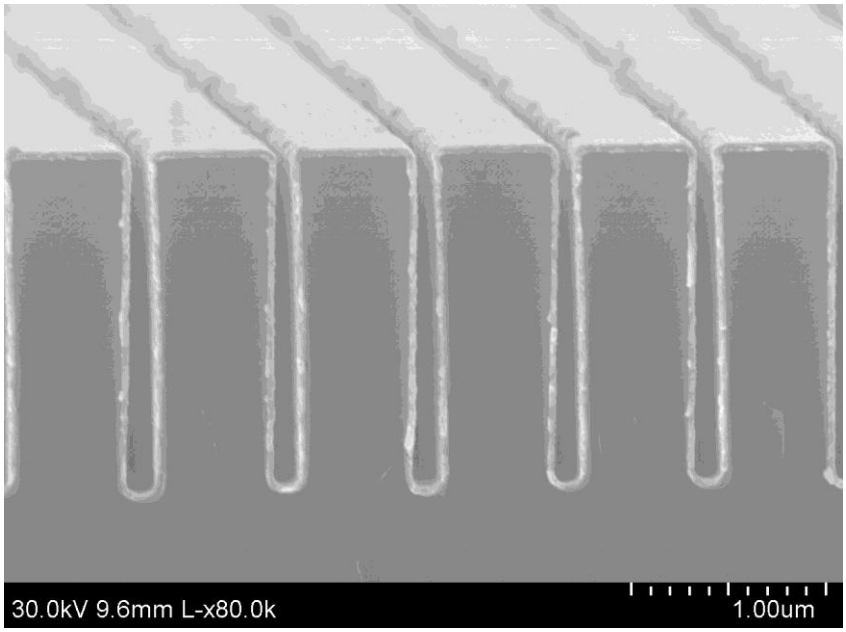

Figure 7.3 High aspect-ratio Si nanoslits fabricated using deep reactive ion etching and coated with Pt using ALD.

7.2.3 HMM nanostructures with high Q resonances

The hyperbolic metamaterial (HMM) nanostructures analyzed in Chapter 6 were used to create broadband absorbers in the visible and infrared. Also mentioned in the chapter was a sharp resonance peak with a high quality factor (Q) at shorter wavelengths. This high Q comes from a discrete cavity mode near the peak of the tapered structure with strong confinement (see Figure 7.4). This sharp resonance could make this structure very useful for plasmonic sensing and the high field confinement could be used for generating non-linear optical effects [45, 141]

However, similar to other plasmonic resonators, when actual devices are fabricated and higher loss is accounted for in the structure, this high Q mode tends to disappear or increase in bandwidth (see Figure 6.11). As demonstrated in Chapter 6, hyperbolic metamaterial nanostructures can couple in light very efficiently and confine it to very small regions due to the large wave vectors / refractive indices that are possible. A dual-tapered nanostructure (similar to a bow tie) of the same metamaterial on a reflective substrate can be used to generate a high Q resonance, even with higher loss metals, leading to effective trapping of a very small band of wavelengths. This structure may also have the advantage of confining light away from the edges of the nanostructure, which are often rough and cause additional loss. It is possible that

experimenting with the sidewall angle could show that steeper sidewalls could provide even more discrete confinement, similar to what was shown in Figure 6.17.

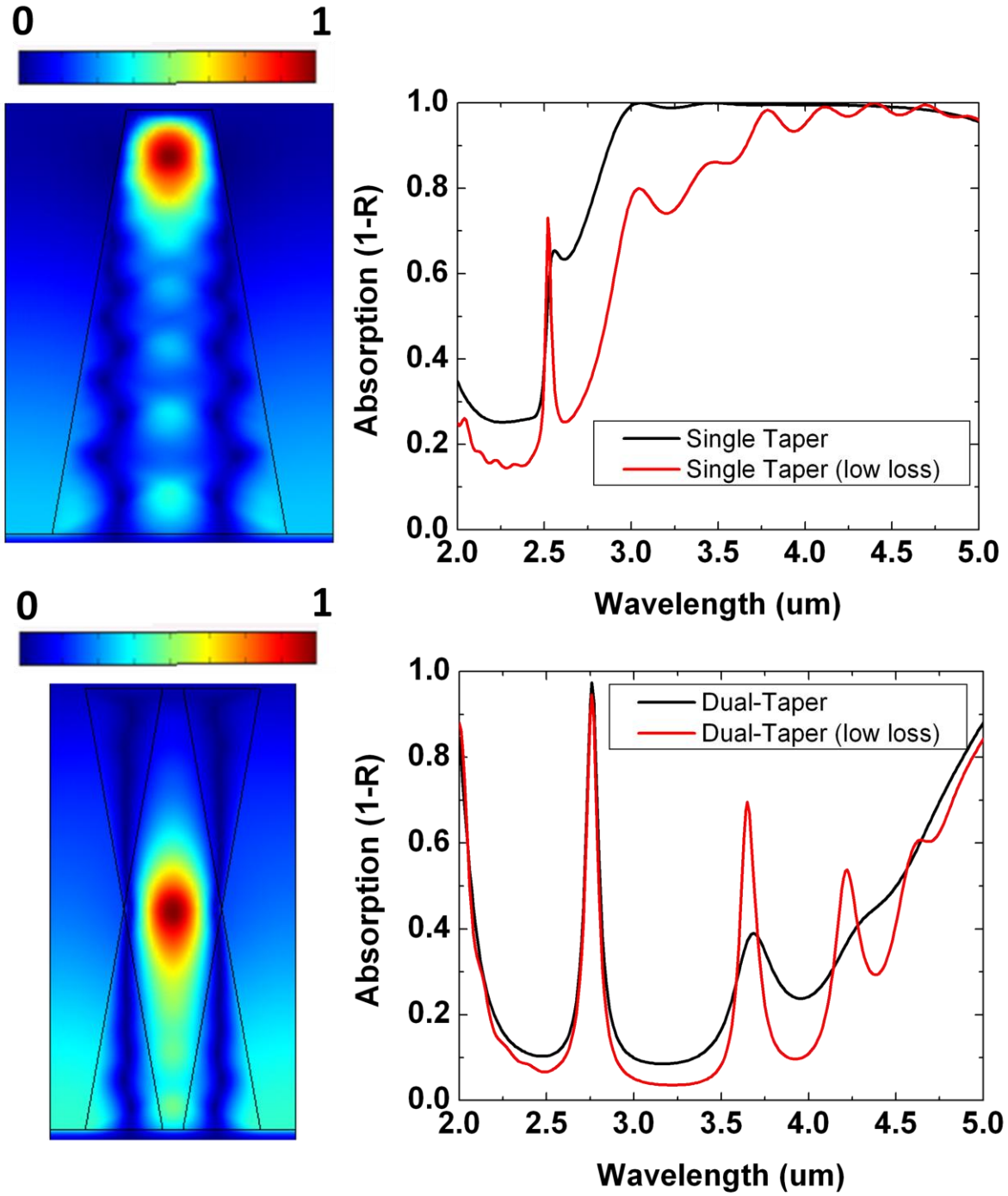

Figure 7.4 Figure showing single taper (top) and dual-taper (bottom) HMM nanostructures to attain high Q absorption. Normalized magnetic field profiles demonstrate strong field enhancement at the top of the structure with a single taper and the intersection of the dual-taper. High Q resonances disappear with increased loss in the single taper structure but remain in the dual taper.

This structure demonstrates some of the interesting properties that could be attainable with hyperbolic metamaterial nanostructures. Applications in fields such as solar cells, non-linear optics, and light emission from incorporated emitters could also be investigated.

7.2.4 Si nanowall structures with CNT coating for solar cells

Si nanowall structures were fabricated in Chapter 2 for use as Li ion battery anodes in order to allow for easy expansion of Si during incorporation of Li. It was also shown that higher initial charging capacity could be reached due to the reduced surface area of nanowall structures as compared to previous works using Si nanowires. It is also possible that nanowalls can improve operation of other devices using nanowires due to this reduced surface area while still maintaining certain advantages of nanostructured materials.

One area where this improvement could be utilized is in the field of hybrid solar cells using Si and carbon nanotubes (CNTs) [144]. This recent work showed that impressive efficiencies greater than 13% were achieved by creating a heterojunction solar cell from a Si substrate coated with CNTs doped through an acid process. Good interface properties between the CNTs and Si, including better charge separation and transport, are achieved through the doping step using acid infiltration, but the thin coating on a flat Si surface does not lend itself to efficient light absorption. Si nanowire structures are often cited for their impressive absorption properties, but the surface state issues mentioned above could reduce the efficiency in charge separation and transport. Previous works have shown that Si nanograting or nanowall structures can lead to increased absorption efficiency [145], and the reduced surface area compared to nanowires could help preserve the impressive interface properties of the original structure.

Working with the group at the University of Maryland, a particular period of nanowall or nanograting will be fabricated using crystalline or amorphous Si in order to enhance absorption efficiency over a certain wavelength range. A CNT coating and doping process will then be attempted to see if interface properties can be preserved while improving optical absorption efficiency.

Appendix A: Free-standing Si nanograting fabrication

1. Sample preparation
    a. Choose silicon-on-insulator (SOI) wafer with device layer thickness for desired grating height. The process below is outlined for grating heights of 2.5 μm. Layers will be defined as in Figure 2.11, with the device layer of 2.5 μm, buried oxide layer (BOX) of 600 nm, and handle layer of 350 μm.
    b. Cleave off sample large enough to fit top grating imprint molds or back side mask (whichever is larger) with some space on the edge for handling. In particular, samples should have a fair amount of space at the edges as compared to the back side mask because this Si will be removed and remove stability from the sample (~ 1 inch x 1 inch, or larger).
    Note: It will help with alignment, handling, and defect reduction later if larger imprint molds are used for the top pattern and you can choose the free-standing area later through the back-side alignment step 3(d).
    c. Clean samples with piranha-clean recipe (1:1 mixture of H_2SO_4:H_2O_2) for 20 minutes and rinse in DI water for 10 minutes.
2. Top Cr mask process (220 nm period + 11 μm cross grating mask definition)
    a. Using GSI PECVD tool, grow approximately 200 nm of SiO_2 on device layer of SOI chip. Standard tool recipe was used with temperature at 380° C. Another piranha-clean can be performed if surface contamination is expected.
    b. Blow any dust off of device layer oxide mask and spin coat mr-I 8030 (typically diluted with propylene glycol methyl ether acetate (PGMEA)) onto sample for required thickness determined by the duty cycle and depth of 220 nm imprint mold. Bake at 140° C for 3 minutes to remove solvent.

c. Imprint sample with 220 nm period grating mold. Place 220 nm period mold in contact with resist surface. Wrap sample in Al foil and cut away excess. Inside of Nanonex NX2000, place the foil-coated sample on the bottom silicone sheet. Attach top silicone sheet to adapter ring and place over the sample/bottom silicone, making sure springs / screws fit correctly. Imprint at 180° C and 600 psi for 5 minutes if using hard mold, 180° C and 500 psi for 2 minutes if using soft mold. Peel off mold along grating direction.
d. Shadow evaporation can be performed to alter the grating linewidth or protect the sidewalls before etching, if necessary. Sample was place on an angled holder (steep enough to insure only sidewall coating) inside of the SJ-20 e-beam evaporator and pumped down to $<2x10^{-6}$ Torr. A desired thickness of Ti was deposited (typically only 5-10 nm for sidewall protection) and the process is repeated to coat the other sidewall of the grating.
e. Residual mr-I 8030 is removed in the LAM 9400 RIE tool using standard O_2 plasma recipe (20 sccm O_2, 30 W bias, 100 W TCP, 12 mT) for nano-scale etching. This will need to be adjusted by the user each time, but at the current tool conditions, the etch rate was approximately 100 nm of mr-I for every 35 seconds of etching. Approximately 10% of etch time should be added to ensure full etching. The typical etch time used was ~ 15-18 seconds in my case.
f. Deposit 20 nm of Cr in the Enerjet e-beam evaporator, pumping down to $<2x10^{-6}$ Torr.
g. Perform liftoff by placing the sample in a beaker full of acetone. Place beaker in an ultrasound agitator for approximately 5 minutes to ensure full liftoff of Cr on top of the grating mask. After IPA and drying, place the sample in the O_2 plasma asher for approximately 2-3 minutes to remove excess resist. The 220 nm grating pattern has now been defined in Cr on the oxide layer on top of the device layer.
h. Repeat steps (b)-(g) above for definition of the 11 μm period cross-grating. A piranha clean can again be performed prior to these steps, if necessary. Note that the 11 μm mold created for the group may not have changed much, so I

will state that I used ~400 nm of mr-I 8030 for the imprint process (the grating height is also ~400 nm). This was accomplished by spinning undiluted mr-I 8030 on the surface with the 220 nm Cr grating / oxide at 1.5 kRPM for 30 seconds. Imprinting was performed perpendicular to the 220 nm period grating. A thin shadow evaporation layer of Ti was used for protection.

i. Following step (h), an O_2 RIE is performed to remove the residual layer and a Cr mask should be on top of the deposited oxide layer on the device Si resembling Figure 2.11 (c).

3. Front and back-side oxide mask definition
    a. Using GSI PECVD tool, grow approximately 3 μm of SiO_2 on the back-side (handle layer) of the chip at 380° C. Special care must be taken on this step when placing the grating face down in the GSI tool because no resist protection can be used on the top surface due to the temperature. It may be advisable to define this oxide mask in the future before doing the top imprinting processes, but this hasn't been tested.
    b. To protect the top-side mask from the next processing steps, spin coat a layer of any thickness of SPR 220 resist on the Cr mask side and soft bake for 2-3 minutes at 115° C.
    c. On the back-side 3 μm oxide mask / handle, after adding a thin layer of HMDS, spin coat approximately 3 μm of SPR 220 resist. Soft bake for 90 seconds at 115° C.
    d. Expose the back side using the MA/BA-6 tool using back-side 1 mm period mask. Take note of the top pattern to make sure that back-side pattern aligns with the grating area on top. This is a good opportunity to choose an area of the Cr grating mask with fewer defects. The time used should be for significant overexposure (~12-15 seconds). Hard bake sample for 90 seconds at 115° C.
    e. Develop in AZ 300k developer tank or beaker for approximately 45 seconds. You should not see any more resist drifting away from the sample at this time. DI rinse and dry the sample.

f. Use LAM 9400 tool to define the bottom oxide (Gases (in sccm): 8 SF_6, 50 C_4F_8, 50 He, 50 Ar, 100 W Bias, 500 W TCP, 10 mT) using the SPR 220 unexposed resist pattern as a mask. An etch rate of approximately 140 nm / minute was assumed. A final time of approximately 1350 seconds was used.
g. Remove all resist (top and bottom) by immersing sample in acetone and IPA and performing another piranha clean. The sample now has the top-side Cr mask and the back-side oxide mask.
h. Use the LAM 9400 tool to etch the top oxide mask. The afk_oxide_hjp5 recipe was used (Gases (in sccm): 10 SF_6, 50 C_4F_8, 50 He, 50 Ar, 10 O_2, 350 W Bias, 500 W TCP, 20 mT). This is a slight variation on our typical oxide etch with higher bias power to etch more vertical oxide structures. 55 seconds of etching time was used. Not much more time can be used since the Cr mask will wear away.
i. Remove any leftover Cr by immersing the sample in Cr etchant. Another piranha clean can be performed at this point if desired. The sample now has an oxide mask on the top and bottom.

4. Deep reactive ion etching (DRIE) and making a free-standing Si grating
    a. To perform the back-side DRIE step, a recessed 4" carrier wafer is used to protect the front surface during the long etch for the back. To define the wafer, use steps similar to 3 (a)-(f) above. Deposit oxide on a Si wafer and spin on SPR 220. An area can be defined either by using a pre-made mask or by wrapping the wafer in Al foil and manually cutting the area that should be exposed in the MA/BA-6. This area should be only slightly larger than the top-side grating mask that it will be protecting (Figure A.1). After exposing and developing, this resist mask can be used to etch the PECVD oxide layer underneath. After removing the resist, this oxide layer can then be used as a mask for DRIE in the STS Pegasus 4 tool. The etched depth of the recess should be at least in the tens of microns, so an etch time of approximately 10 minutes was used for the standard LNF Recipe 3. The wafer should then be coated with new GSI PECVD oxide in order to protect the carrier during Si etching.

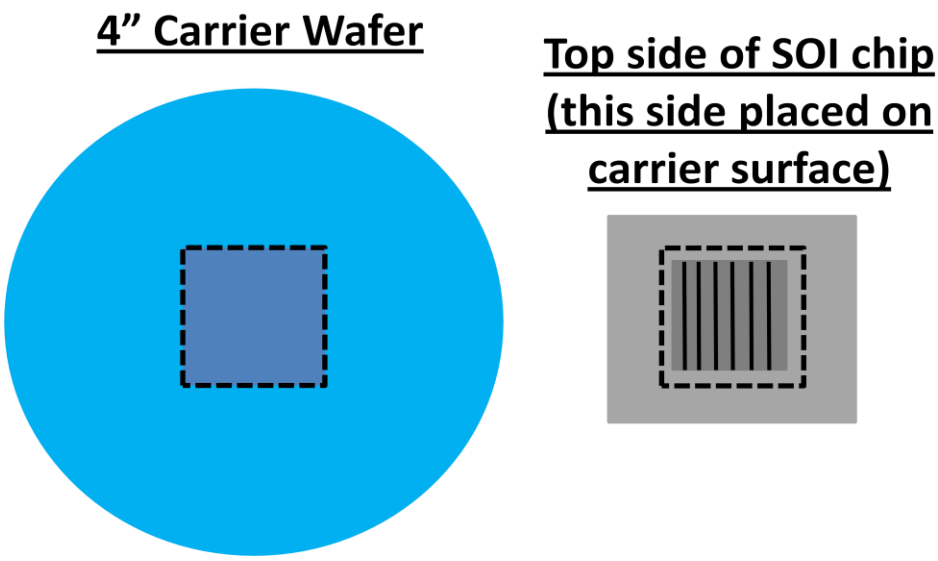

Figure A.1: Diagram showing the defined size of the recessed carrier wafer for back-side etching (not to scale). Light blue is for the 4” Si carrier wafer as compared to the light gray for the SOI chip. Dark gray represents the patterned top grating area. The recessed area is shown in dark blue. The dark blue area is slightly larger than the patterned grating area, but still small enough to not overlap the SOI chip sides.

b. Attach the sample with the grating side facing into the recess of the carrier defined above. The attachment process at the time was done by melting a crystal bond material around the recessed area when the wafer is on a hot plate at ~80° C. The sample is then placed onto the carrier, leaving the back side exposed. When the wafer is cooled, the sample will adhere to the surface and the front should be very well sealed from any etchant gases / contamination.

c. After performing a quick O_2 descum in the Pegasus 4 (20 mT, 200 sccm O_2, 2500 W Coil, 75 W Bias) DRIE was performed using the standard LNF Recipe 3 (10 °C, **Dep:** 4 seconds, 200 sccm C_4F_8, 2000 W coil; **Etch:** 6.5 seconds, 600 SF_6, 60 O_2, 4000 W coil, 50 W bias (100 W boost, 2 seconds) 80% etch duty cycle; **Other:** Dep. Pressure: Delay 100 mT, Boost 100 mT, Main 25 mT; Etch Pressure: Delay 100 mT, Boost 50 mT, Main 100 mT) for approximately 27 minutes to etch the 350 μm Si handle layer (see Figure 2.12). Due to changing tool conditions, this etch should be monitored continuously after approximately 20-25 minutes. The user should look for the

exposure of the oxide layer underneath the Si handle, which appears darker. Dark spots will typically appear at the corners of the defined back-side mask and work towards the center since deep etches are not uniform over the entire area. One should wait until the back-side pattern appears black throughout. The chip can be removed by placing the carrier on the 80° C hot plate and using a razor blade and tweezers to force the piece up. Residual crystal bond can be removed using water, but care must be taken since there is now a thin layer of Si. You may want to test this once or twice using the back-side pattern on a separate SOI chip that doesn't have a grating on top.

d. Next, the BOX layer is removed from the back side of the SOI chip. Once again, the mnf_oxide1 recipe in the LAM 9400 is used. An etch time of approximately 750 seconds was performed to remove the 600 nm layer.
e. The final top DRIE step needs a new kind of recessed carrier wafer (Figure A.2). It can be defined using the same processes as step 4(a). 4 recessed lines away from the central recessed area are used to make sure that the pressure is the same on the front and back of the chip. The central recessed area should be slightly larger than the back-side, 1 mm period patterned area.

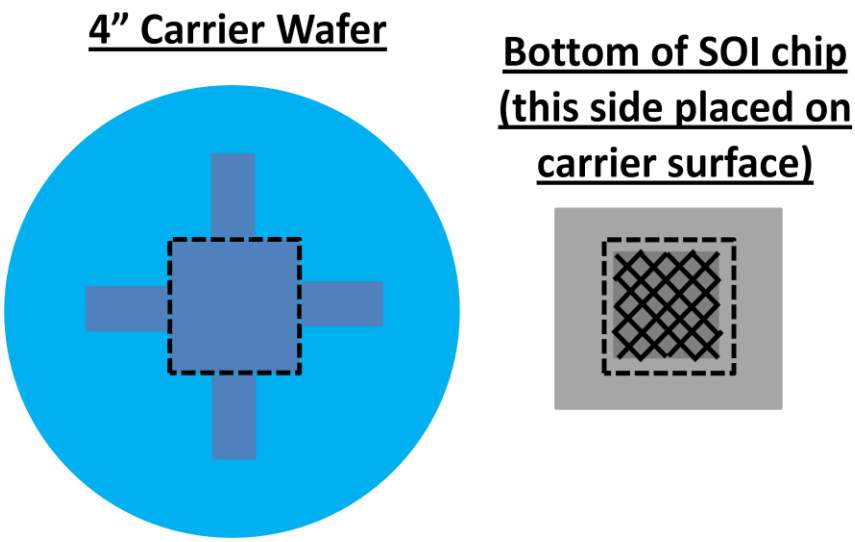

Figure A.2: Diagram showing the defined size of the recessed carrier wafer for front-side etching (not to scale). Light blue is for the 4” Si carrier wafer as compared to the light gray for the SOI chip. Dark gray represents the patterned back-side area with 1 mm period squares. The recessed area is shown in dark blue. The central dark blue area is slightly larger than the back-side patterned area, but still small enough to not overlap the SOI chip sides.

f. The final DRIE step to define the top grating is then performed. Using the recipe outlined in Table 3.1 should be used as a starting point, but the etch rates and processes could be improved, especially by using metal masks. For example, a hold time could be introduced into the process to reduce any heat that might be generated during etching. This means that the sample will hold on the -15° C chuck for a certain time (maybe 2-4 seconds) before a new etch / deposition cycle is started, allowing any heat generated to be dissipated. 12 minutes for 2.5 μm grating (-15 °C, **Dep:** 1 seconds, 150 sccm C_4F_8, 2000 W coil; **Etch:** 6.5 seconds, 80 sccm C_4F_8, 200 SF_6, 1100 W coil, 30-48 W bias (linear ramp); **Other:** Delay times added for etch gas flow, pressure, and power (5 seconds), 7.5 mT etch and dep.)

g. This will define the final patterned grating. If necessary, this is a good opportunity to remove any crystal bond from previous processing, but this needs to be done by lightly rubbing the heated chip with a wet swab, making sure to avoid any liquid contact with the free-standing grating area which can cause sticking of the grating lines.

Appendix B: Single interface and metal-insulator-metal plasmon modes

Single interface surface plasmon

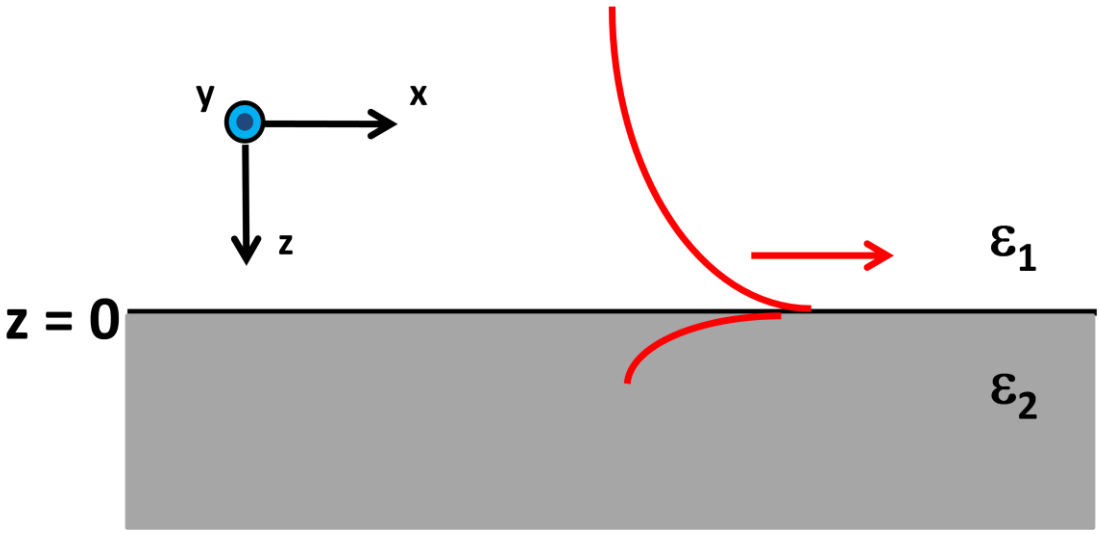

Figure B.1: Diagram showing single interface surface plasmon mode.

Figure B.1 shows the diagram used to derive a surface plasmon mode at the interface between a dielectric (permittivity of ε_1) and metal (permittivity of ε_2), assuming that we are operating at lower frequencies than the plasma frequency discussed in Chapter 3. This derivation can be found in many textbooks but is mainly taken from Ref. [147]. If the z = 0 point or x-y plane is assumed to be the interface, light propagation in the x-direction can be simply derived. As also stated in Chapter 3, only light with magnetic field polarized in the y-direction can excite plasmon modes, leaving us with the following equations for the E and H fields in each medium:

$$\boldsymbol{E_1} = (E_{x1}, 0, E_{z1}) \exp[i(k_x x - \omega t)] \exp(ik_{z1} z)$$

$$\boldsymbol{H_1} = (0, H_{y1}, 0) \exp[i(k_x x - \omega t)] \exp(ik_{z1} z)$$

$$\boldsymbol{E_2} = (E_{x2}, 0, E_{z2}) \exp[i(k_x x - \omega t)] \exp(ik_{z2} z)$$

$$\boldsymbol{H_2} = (0, H_{y2}, 0) \exp[i(k_x x - \omega t)] \exp(ik_{z2} z)$$

where the subscripts 1 and 2 refer to the dielectric and metal, respectively. ω is the frequency while x, z represent the coordinate position. Note that the wave vectors (k_z) in the z-direction are separately defined for each medium while k_x remains the same for both due to continuity at the boundary.

Applying the Maxwell equation of $\nabla \cdot E = 0$:

$$E_{z1} = -E_{x1}\frac{k_x}{k_{z1}}$$

$$E_{z2} = -E_{x2}\frac{k_x}{k_{z2}}$$

Applying Faraday's law ($\nabla \times E = -\mu\frac{\partial H}{\partial t}$) and assuming μ is the permeability of free space (μ_o) for both materials gives:

$$H_{y1} = \omega E_{x1}\varepsilon_1\varepsilon_0/k_{z1}$$

$$H_{y2} = \omega E_{x2}\varepsilon_2\varepsilon_0/k_{z2}$$

Next we can apply the boundary conditions stating that the tangential components of H and E are continuous at the interfaces ($H_{y1} = H_{y2}$, $E_{x1} = E_{x2}$), leading to:

$$\frac{\varepsilon_1}{k_{z1}} = \frac{\varepsilon_2}{k_{z2}}$$

while recognizing that, assuming that k_z values are indeed imaginary in both media (trapped surface waves, meaning $ik_{z1} > 0$ and $ik_{z2} < 0$):

$$k_{z1} = -i\sqrt{{k_x}^2 - \varepsilon_1 k^2} \quad (k_x^2 > \varepsilon_1 k^2)$$

$$k_{z2} = i\sqrt{{k_x}^2 - \varepsilon_2 k^2} \quad (k_x^2 > \varepsilon_2 k^2)$$

where $k = \omega/c$. Substituting these equations into the one above gives the surface plasmon relation.

$$k_x = k\sqrt{\frac{\varepsilon_1\varepsilon_2}{\varepsilon_1 + \varepsilon_2}}$$

We know from our constraint on operating frequency that $\varepsilon_1 > 0$ while $\varepsilon_2 < 0$ in this range, giving a real k_x (needed for propagation in the x-direction) if $|\varepsilon_2| > \varepsilon_1$. This equation also displays how the k_x wave vector cannot be excited directly since it is greater than the maximum achievable wave vector from the dielectric $\sqrt{\varepsilon_1}k$.

Metal-insulator-metal waveguide

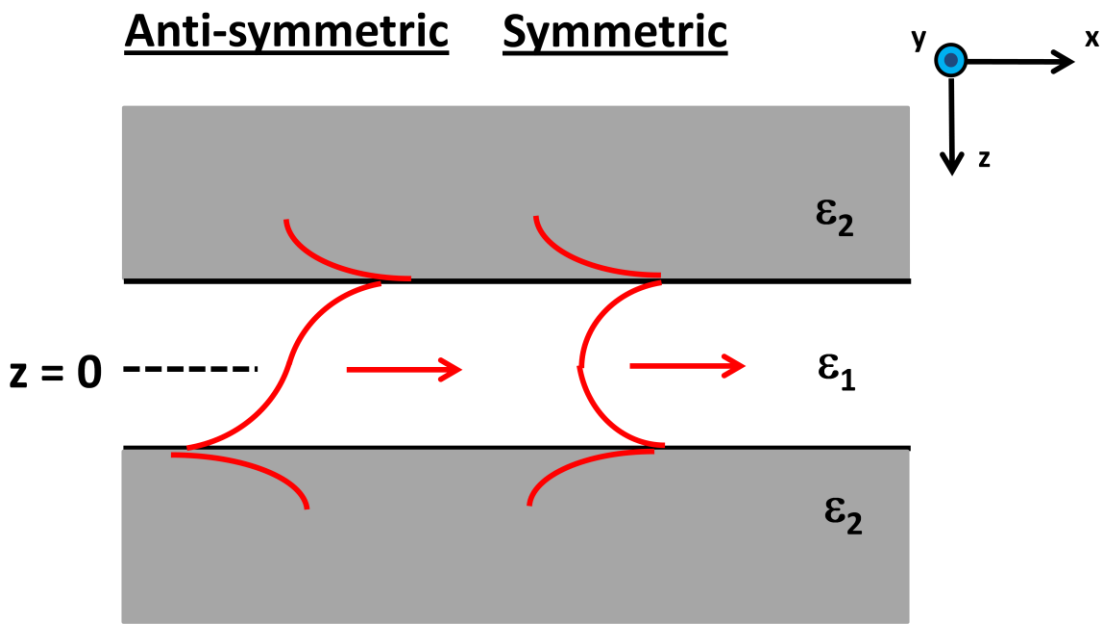

Figure B.2: Diagram showing metal-insulator-metal waveguide modes.

Without much alteration to the single-interface analysis, we can derive the relationships for metal-insulator-metal (MIM) waveguides. This consists of two semi-infinite metal plates surrounding a dielectric core of thickness d. The z = 0 point is taken to be at the center of the core (from z = -d/2 to d/2). Since both TE (E-field in the y-direction) and TM (B-field in the y-direction) are discussed in Chapter 3, both derivations will be provided, but TM is still the polarization which supports plasmon propagation. Most of this derivation is described in Ref. [13].

We can begin by defining the E and B components of the fields given polarization and knowing the exponential decay that occurs in the metallic cladding. For example, the TM polarized light inside the core is given as:

$$\boldsymbol{E_{x1}} = \exp(-ik_{z1}z) \pm \exp(ik_{z1}z)$$

$$\boldsymbol{E_{y1}} = 0$$

$$\boldsymbol{E_{z1}} = \frac{\mathrm{k_x}}{\mathrm{k_{z1}}}[\exp(-ik_{z1}z) \mp \exp(ik_{z1}z)]$$

$$\boldsymbol{B_{x1}} = 0$$

$$\boldsymbol{B_{y1}} = \frac{-\omega\varepsilon_1}{\mathrm{ck_x}}[\exp(-ik_{z1}z) \mp \exp(ik_{z1}z)]$$

$$\boldsymbol{B_{z1}} = 0$$

The TE polarized light inside the core is given as:

$$\boldsymbol{E_{x1}} = 0$$

$$\boldsymbol{E_{y1}} = \exp(ik_{z1}z) \pm \exp(-ik_{z1}z)$$

$$\boldsymbol{E_{z1}} = 0$$

$$\boldsymbol{B_{x1}} = \frac{-\mathrm{k_{z1}c}}{\omega}[\exp(ik_{z1}z) \mp \exp(-ik_{z1}z)]$$

$$\boldsymbol{B_{y1}} = 0$$

$$\boldsymbol{B_{z1}} = \frac{\mathrm{k_x c}}{\omega}[\exp(ik_{z1}z) \pm \exp(-ik_{z1}z)]$$

Outside of the guide for TM, the decay and continuity constraints lead to:

$$\boldsymbol{E_{x2}} = [\exp(-ik_{z1}d/2) \pm \exp(ik_{z1}d/2)]\exp(ik_{z2}(z - d/2))$$

$$\boldsymbol{E_{y2}} = 0$$

$$\boldsymbol{E_{z2}} = \frac{\varepsilon_1 k_x}{\varepsilon_2 k_{z1}}[\exp(-ik_{z1}d/2) \mp \exp(ik_{z1}d/2)]\exp(ik_{z2}(z - d/2))$$

$$\boldsymbol{B_{x2}} = 0$$

$$\boldsymbol{B_{y2}} = \frac{-\omega\varepsilon_1}{\mathrm{ck_x}}[\exp(-ik_{z1}d/2) \mp \exp(ik_{z1}d/2)]\exp(ik_{z2}(z - d/2))$$

$$\boldsymbol{B_{z2}} = 0$$

And, for TE:

$$\boldsymbol{E_{x1}} = 0$$

$$\boldsymbol{E_{y1}} = [\exp(ik_{z1}d/2) \pm \exp(-ik_{z1}d/2)]\exp(ik_{z2}(z - d/2))$$

$$\boldsymbol{E_{z1}} = 0$$

$$\boldsymbol{B_{x1}} = \frac{-\mathrm{k_{z1}c}}{\omega}[\exp(ik_{z1}d/2) \mp \exp(-ik_{z1}d/2)]\exp(ik_{z2}(z - d/2))$$

$$\boldsymbol{B_{y1}} = 0$$

$$\boldsymbol{B_{z1}} = \frac{\mathrm{k_x c}}{\omega}[[\exp(ik_{z1}d/2) \pm \exp(-ik_{z1}d/2)]\exp(ik_{z2}(z - d/2))$$

The relationship between k_x and k_z must also be followed due to momentum conservation:

$$k_{z1,2}{}^2 = \varepsilon_{1,2}(\frac{\omega}{c})^2 - k_x^2$$

The signs used are chosen based off of the two allowed modes in propagation, the anti-symmetric and symmetric modes (shown in Figure B.2). The anti-symmetric modes follow the dispersion equations of:

$$\varepsilon_1 k_{z2} + \varepsilon_2 k_{z1} \tanh\left(\frac{-ik_{z1}d}{2}\right) = 0 \quad TM$$

$$k_{z2} + k_{z1} \tanh\left(\frac{-ik_{z1}d}{2}\right) = 0 \quad TE$$

The symmetric mode equations are given by:

$$\varepsilon_1 k_{z2} + \varepsilon_2 k_{z1} \coth\left(\frac{-ik_{z1}d}{2}\right) = 0 \quad TM$$

$$k_{z2} + k_{z1} \coth\left(\frac{-ik_{z1}d}{2}\right) = 0 \quad TE$$

References

1. H.B. Niemann, S.K. Atreya, S.J. Bauer, K. Biemann, B. Block, G.R. Carignan, T.M. Donahue, R.L. Frost, D. Gautier and J.A. Haberman, "The Gas Chromatograph Mass Spectrometer for the Huygens Probe," *Space Sci. Rev.*, **104**, 553 (2002).

2. T.E. Moore, D.J. Chornay, M.R. Collier, F.A. Herrero, J. Johnson, M.A. Johnson, J.W. Keller, J.F. Laudadio, J.F. Lobell and K.W. Ogilvie, "The low-energy neutral atom imager for IMAGE," *Space Sci. Rev.*, **91**, 155 (2000).

3. C.J. Pollock, K. Asamura, J. Baldonado, M.M. Balkey, P. Barker, J.L. Burch, E.J. Korpela, J. Cravens, G. Dirks and M.-C. Fok, "Medium energy neutral atom (MENA) imager for the IMAGE mission," *Space Sci. Rev.*, **91**, 113 (2000).

4. P. Mukherjee, T. Zurbuchen, and L.J. Guo, "Fabrication and testing of freestanding Si nanogratings for UV filtration on space-based particle sensors," *Nanotechnology*, **20**, 325301 (2009).

5. P. Mukherjee, A. Bruccoleri, R.K. Heilmann, M.L. Schattenburg, A.F. Kaplan, and L.J. Guo, "Plasma etch fabrication of 60:1 aspect-ratio silicon nanogratings with 200 nm pitch," *Jour. Vac. Sci. Technol. B*, **28**, C6P70 (2010).

6. G.G. Kang, I. Vartiainen, B.F. Bai, H. Tuovinen, and J. Turunen, "Inverse polarizing effect of subwavelength metallic gratings in deep ultraviolet band," *Appl. Phys. Let.*, **99**, 071103 (2011).

7. A. Lehmuskero, B.F. Bai, P. Vahimaa, and M. Kuittinen, "Wire-grid polarizers in the volume plasmon region," *Opt. Express*, **17**, 5481 (2009).

8. J. Wan, A.F. Kaplan, J. Zheng, X. Han, Y. Chen, N. Faenza, T. Li, L.J. Guo, and L. Hu, "Silicon nanowalls for Li-ion batteries fabricated using nanoimprint lithography," *Adv. Ener. Mater.* (in submission).

9. T.M. Lee, Y.J. Choi, S.Y. Nam, C.W. You, D.Y. Na, H.C. Choi, D.Y. Shin, K.Y. Kim, and K.I. Jung, "Color filter patterned by screen printing," *Thin Solid Films*, **516**, 7875 (2008).

10. H.E. Kondakci, M. Yaman, O. Koylu, A.Dana, and M. Bayindir, "All chalco-genide glass omnidirectional photonic band gap variable infrared filters," *Appl. Phys. Lett.*, **94**, 111110 (2009).

11. M. Razeghi and A. Rogalski, "Semiconductor ultraviolet detectors," *J. Appl. Phys.*, **79**, 7433 (1996).

12. J. Le Perchec, R. Espiau de Lamaestre, M. Brun, N. Rochat, O. Gravrand, G. Badano, J. Hazart, and S. Nicoletti, "High rejection bandpass optical filters based on subwavelength metal patch arrays," *Opt. Express*, **19** 15720 (2011).

13. J. A. Dionne, L.A. Sweatlock, H.A. Atwater, and A. Polman, "Plasmon slot waveguides: towards chip-scale propagation with subwavelength-scale localization," *Phys. Rev. B* **73**, 35407 (2006).

14. Y.T. Yoon and S.S. Lee, "Transmission type color filter incorporating a silver film based etalon," *Opt. Express*, **18**, 5344 (2010).

15. G. Vincent, S. Collin, N. Bardou, and J.L. Pelouard, "Large-area dielectric and metallic freestanding gratings for midinfrared optical filtering applications," *Jour. Vac. Sci. Technol. B,* **26**, 1852 (2008).

16. T.W. Ebbesen, H.J. Lezec, H.F. Ghaemi, T. Thio, and P.A. Wolff, "Extraordinary optical transmission through subwavelength hole arrays," *Nature* **391 ,** 667 (1998).

17. A.F. Kaplan, T. Xu, Y.K. Wu, and L.J. Guo, "Multilayer pattern transfer for plasmonic color filter applications," *Jour. Vac. Sci. Technol. B* **28,** C6O60 (2010).

18. A.F. Kaplan, T. Xu, and L.J. Guo, "High Efficiency Resonance-Based Color Filters with Tunable Transmission Bandwidth Fabricated Using Nanoimprint Lithography," *Appl. Phys. Lett.* **99**, 143111 (2011).

19. P. Bouchon, C. Koechlin, F. Pardo, R. Haïdar, and J.-L. Pelouard, "Wideband Omnidirectional Infrared Absorber with a Patchwork of Plasmonic Nanoantennas," *Opt. Lett.*, **37**, 1038 (2012).

20. Y. Cui, J. Xu, K.H. Fung, Y. Jin, A. Kumar, S. He, N.X. Fang, "A Thin Film Broadband Absorber Based on Multi-Sized Nanoantennas," *Appl. Phys. Lett.* **99**, 253101 (2011).

21. Y. Cui, K.H. Fung, J. Xu, H. Ma, Y. Jin, H. Se, N.X. Fang, "Ultrabroadband Light Absorption by a Sawtooth Anisotropic Metamaterial Slab," *Nano. Lett.* **12**, 1443 (2012).

22. X. Yang, J. Yao, J. Rho, X. Yin, and X. Zhang, "Experimental realization of three-dimensional indefinite cavities at the nanoscale with anomalous scaling laws," *Nature Photonics*, **6**, 450 (2012).

23. C.L. Cortes, W. Newman, S. Molesky, and Z. Jacob, "Quantum nanophotonics using hyperbolic metamaterials," *J. Opt.*, **14**, 063001 (2012).

24. J. Valentine, J. Li, S. Zhang, T. Zentgraf, G. Bartal, X. Zhang, "Three-Dimensional Optical Metamaterial with Negative Refractive Index," *Nature* **, 455**, 376 (2008).

25. S.Y.Chou, P. R. Krauss, and P.J. Renstrom, "Imprint of sub-25 nm vias and trenches in polymers," *Appl. Phys. Lett.*, **67**, 3114 (1995).

26. L.J. Guo, "Nanoimprint Lithography: Methods and Material Requirements," *Adv. Mater.*, **19**, 495 (2007).

27. C. Pina-Hernandez and L.J. Guo, "High-resolution functional epoxysilsesquioxane-based patterning layers for large-area nanoimprinting," *ACS Nano*, **4**, 4776 (2010).

28. S.H. Ahn and L.J. Guo, "Large-Area Roll-to-Roll and Roll-to-Plate Nanoimprint Lithography: A Step toward High-Throughput Application of Continuous Nanoimprinting," *ACS Nano*, **3**, 2304 (2009).

29. C. Cardinaud, M.C. Peignon, and P.Y. Tessier, "Plasma etching: principles, mechanisms, application to micro-and nano-technologies," *Appl. Surf. Sci.*, **164**, 72 (2000).

30. H. Jansen, H. Gardeniers, M. de Boer, M. Elwenspoek, and J. Fluitman, "A survey on the reactive ion etching of silicon in microtechnology," *J. Micromech. Microeng.*, **6**, 14 (1996).

31. M.J. de Boer, J.G.E. Gardeniers, H.V. Jansen, E. Smulders, M.J. Gilde, G. Roelofs, J.N. Sasserath, and M. Elwenspoek, "Guidelines for etching silicon MEMS structures using fluorine high-density plasmas at cryogenic temperatures," *J. Microelectromech. Syst.*, **11**, 385 (2002).

32. F. Lärmer and A. Schilp, "Method for anisotropic plasma etching of substrate," USA Patent, 5501893, Robert Bosch GmbH (1996).

33. B. Volland, F. Shi, P. Hudek, H. Heerlein, and I.W. Rangelow, "Dry etching with gas chopping without rippled sidewalls," *J. Vac. Sci. Technol. B*, **17**, 2768 (1999).

34. K.J. Morton, G. Nieberg, S. Bai, and S.Y. Chou, "Wafer-scale patterning of sub-40 nm diameter and high aspect ratio (>50:1) silicon pillar arrays by nanoimprint and etching," *Nanotech.* **19**, 345301 (2008).

35. M.D. Kelzenberg, S.W. Boettcher, J.A. Petykiewicz, D.B. Turner-Evans, M.C. Putnam, E.L.Warren, J.M. Spurgeon, R.M. Briggs, N.S. Lewis, and H.A. Atwater, "Enhanced absorption and carrier collection in Si wire arrays for photovoltaic applications," *Nat. Mater.*, **9**, 239 (2010).

36. C.K. Chan, H. Peng, G. Liu, K. McIlwrath, X.F. Zhang, R.A. Huggins, and Y. Cui, "High-performance lithium battery anodes using silicon nanowires," *Nat. Nanotech.*, **3**, 31 (2008).

37. L. Sainiemi, J. Viheriälä, T. Sikanen, J. Laukannen, and T. Niemi, "Nanoperforated silicon membranes fabricated by UV-nanoimprint lithography, deep reactive ion etching and atomic layer deposition," *J. Micromech. Microeng.*, **20**, 077001 (2010).

38. P. Mukherjee, M.G. Kang, T.H. Zurbuchen, L.J. Guo, and F.A. Herrero, "Fabrication of high aspect ratio Si nanogratings with smooth sidewalls for a deep-UV blocking particle filter," *Jour. Vac. Sci. and Technol. B*, **25**, 2645 (2007).

39. J.A. Gilbert, T.H. Zurbuchen, A.F. Kaplan, and L.J. Guo, "Comparison of silicon nanoscale gratings to carbon foils for use in space plasma mass spectrometers," *AGU Fall Meeting Abstracts*, B1629 (2010).

40. J.T.M. van Beek, R.C. Fleming, P.S. Hindle, J.D. Prentiss, M.L. Schattenburg, and S. Ritzau, "Nanoscale freestanding gratings for ultraviolet blocking filters," *J. Vac. Sci. Technol. B,* **16**, 3911 (1998).

41. G.B. Andrews, T.H. Zurbuchen, B.H. Mauk, H. Malcom, L.A. Fisk, G. Gloeckler, G.C. Ho, J.S. Kelley, P.L. Koehn, T.W. LeFevere, S.S. Livi, R.A. Lundgren, and J.M. Raines, "The Energetic Particle and Plasma Instrument on the MESSENGER Spacecraft," *Space Sci. Rev.*, **131**, 523 (2007).

42. M.L. Brongersma and P.G. Kik, *Surface Plasmon Nanophotonics, Springer Series in Optical Sciences vol 131,* Dordrecht: Springer (2007).

43. S.A. Maier, *Plasmonics: Fundamentals and Applications*, New York: Springer (2007).

44. W.L. Barnes, A. Dereux, and T.W. Ebbesen, "Surface plasmon subwavelength optics," *Nature* **424**, 824 (2003).

45. R. Zia, J.A. Schuller, A. Chandran, M.L. Brongersma, "Plasmonics: the next chip-scale technology," *Mater. Today* **9,** 20 (2006).

46. S. Hayashi and T. Okamoto, "Plasmonics: visit the past to know the future," *J. Phys. D: Appl. Phys* **45**, 433001 (2012).

47. A. Boltasseva and H.A. Atwater, "Low-loss plasmonic metamaterials," *Science* **331**, 290 (2011).

48. E.D. Palik, *Handbook of Optical Constants of Solids,* Academic Press (1985).

49. E.D. Palik, *Handbook of Optical Constants of Solids II,* Academic Press (1991).

50. H.J. Hinz and H. Raether, "Line shape of the volume plasmons of silicon and germanium," *Thin Solid Films* **58**, 281 (1979).

51. Y.R. Hong, K. Asakawa, D.H. Adamson, P.M. Chaikin, and R.A. Register, "Silicon nanowire grid polarizer for very deep ultraviolet fabricated from a shear-aligned diblock copolymer template," *Opt. Lett.* **32**, 3125 (2007).

52. R. Zia, M.D. Selker, P.B. Catrysse, and M.L. Brongersma, "Geometries and materials for subwavelength surface plasmon modes," *J. Opt. Soc. Am. A* **21**, 2442 (2004).

53. J.A. Dionne, H.J. Lezec, and H.A. Atwater, "Highly confined photon transport in subwavelength metallic slot waveguides," *Nano Lett.* **6**, 1928 (2006).

54. H.T. Miyazaki and Y. Kurokawa, "Squeezing visible light waves into a 3-nm thick ad 55-nm long plasmon cavity," *Phys. Rev. Lett.* **96**, 097401 (2006).

55. Y. Kurokawa and H.T. Miyazaki, "Metal-insulator-metal plasmon nanocavities: analysis of optical properties," *Phys. Rev. B* **75**, 035411 (2007).

56. J. A. Dionne, L. A. Sweatlock, A. Polman, and H. A. Atwater, "Planar metal plasmon waveguides: frequency-dependent dispersion, propagation, localization, and loss beyond the free electron model," *Phys. Rev. B* **72**, 075405 (2005).

57. M. Ritala and M. Leskelä, "Atomic layer epitaxy – a valuable tool for nanotechnology?" *Nanotechnology* **10**, 19 (1999).

58. S.M. George, “Atomic layer deposition: an overview,” *Chem. Rev.* **110**, 111 (2012).

59. T. Aaltonen, M. Ritala, Y.L. Tung, Y. Chi, K. Arstila, K. Meinander, and M. Leskelä, “Atomic layer deposition of platinum thin films,” *Chem. Mater.* **15**, 1924 (2003).

60. X.T. Kong, W.G. Yan, Z.B. Li, and J.G. Tian, “Optical properties of metal-multi-insulator-metal plasmonic waveguides,” *Opt. Express* **20**, 12133 (2012).

61. D. Dai and S. He, “Low-loss hybrid plasmonic waveguide with double low-index nano-slots,” *Opt. Express* **18**, 17958 (2010).

62. N.N. Feng and L. Dal Negro, “Plasmon mode transformation in modulated-index metal-dielectric slot waveguides,” *Opt. Lett.* **32**, 3086 (2007).

63. H. Okabe, “Intense Resonance Line Sources for Photochemical Work in the Vacuum Ultraviolet Region,” *J. Opt. Soc. Amer.*, **54**, 478 (1964).

64. W. Cai, U.K. Chettiar, H.K. Yuan, V.C. de Silva, A.V. Kildeshev, V.P. Drachev, and V.M. Shalaev, “Metamagnetics with rainbow colors,” *Opt. Express*, **15**, 3333 (2007).

65. Y. Gong, S. Yerci, R. Li, L. Dal Negro, and J. Vuckovic, “Enhanced light emission from erbium doped silicon nitride in plasmonic metal-insulator-metal structures,” *Opt. Express* 17, 20642 (2009).

66. K. Diest, J. A. Dionne, M. Spain, and H. A. Atwater, “Tunable Color Filters Based on Metal-Insulator-Metal Resonators,” *Nano Lett.* **9**, 2579 (2009).

67. K. Kumar, H. Duan, R.S. Hegde, S.C.W. Koh, J.N. Wei, and J.K.W. Yang, “Printing colour at the optical diffraction limit,” *Nature Nanotech.* **7**, 557 (2012).

68. T. Xu, Y.K. Wu, X.G. Luo, and L.J. Guo, “Plasmonic nanoresonators for high-resolution colour filtering and spectral imaging,” *Nat. Comm.* **1**, 59 (2010).

69. Y. Kanamori, M. Shimono, and K. Hane, “Fabrication of Transmission Color Filter Using Silicon Subwavelength Gratings on Quartz Substrates,” *IEEE Photonics Technol. Lett.* **18**, 2126 (2006).

70. D. Inoue, A. Miura, T. Nomura, H. Fujikawa, K. Sato, N. Ikeda, D. Tsuya, Y. Sugimoto, and Y. Koide, “Polarization independent visible color filter comprising an aluminum film with

surface-plasmon enhanced transmission through a subwavelength array of holes," *Appl. Phys. Lett.* **98**, 093113 (2011).

71. Y. Ye, Y. Zhou, H. Zhang, and L. Chen, "Polarizing color filter based on subwavelength metal-dielectric grating," *Applied Optics* **50**, 1356 (2011).

72. T. Xu, A.F. Kaplan, and L.J. Guo, "Angle-independent reflective Fabry-Perot color filter," *J. Opt. Soc. Am. B* (under review).

73. T.H. Noh, Y.T. Yoon, S.S. Lee, D.Y. Choi, and S.C. Lim, "Highly angle-tolerant spectral filter based on an etalon resonator incorporating a high index cavity," *J. Opt. Soc. Korea* **16,** 299 (2012).

74. M.A. Kats, R. Blanchard, P. Genevet, and F. Capasso, "Nanometre optical coatings based on strong interference effects in highly absorbing media," *Nature Materials*, DOI: 10.1038/NMAT3443.

75. Y. Xia and G.M. Whitesides, "Soft Lithography," *Angew. Chem. Int. Ed.* **37**, 550 (1998).

76. M.G. Kang and L.J. Guo, "Metal transfer assisted nanolithography on rigid and flexible substrates," *J. Vac. Sci. Technol. B* **26**, 2421 (2008).

77. Y. L. Loo, R.L. Willett, K.W. Baldwin, and J.A. Rogers, "Additive, Nanoscale Patterning of Metal Films with a Stamp and a Surface Chemistry Mediated Transfer Process: Applications in Plastic Electronics," *Appl. Phys. Lett.* **81**, 562 (2002).

78. M.G. Kang, H.J. Park, S.H. Ahn, and L.J. Guo, "Transparent Cu nanowire mesh electrode on flexible substrates fabricated by transfer printing and its application in organic solar cells," *Solar Energy Mat. and Solar Cells*, **94**, 1179 (2010).

79. D. Chanda, K. Shigeta, S. Gupta, T. Cain, A. Carlson, A. Mihi, A. Baca, G. Bogart, P. Braun, and J.A. Rogers, "Large-area flexible 3D optical negative index metamaterial formed by nanotransfer printing," *Nat. Nanotech.*, **6**, 402 (2011).

80. G. Si, Y. Zhao, H. Liu, S. Teo, M. Zhang, T.J. Huang, A.J. Danner, and J. Teng, "Annular aperture array based color filter," *Appl. Phys. Lett.*, **99**, 033105 (2011).

81. H.F. Ghaemi, T. Thio, D.E. Grupp, T.W. Ebbesen, and H.J. Lezec, "Surface plasmons enhance optical transmission through subwavelength holes," *Phys. Rev. B* **58,** 6779 (1998).

82. A. Degiron, H.J. Lezec, W.L. Barnes, and T.W. Ebbesen, "Effects of hole depth on enhanced light transmission through subwavelength hole arrays," *Appl. Phys. Lett.* **81,** 4327–4329 (2002).

83. S.S. Wang, R. Magnusson, J.S. Bagby, and M.G. Moharam, "Guided-mode resonances in planar dielectric-layer diffraction gratings," *J. Opt. Soc. Am. A* **7**, 1470 (1990).

84. N. Nguyen-Huu, Y.L. Lo, and Y.B. Chen, "Color filters featuring high transmission efficiency and broad bandwidth based on resonant waveguide-metallic grating," *Opt. Comm.*, **284**, 2473 (2011).

85. P.B. Johnson and R.W. Christy, "Optical Constants of the Noble Metals," *Phys. Rev. B* **6**, 4370 (1972).

86. B. Luk'yanchuk, N.I. Zheludev, S.A. Maier, N.J. Halas, P. Nordlander, H. Giessen, and C.T. Chong, "The Fano resonance in plasmonic nanostructures and metamaterials," *Nature Materials* **9**, 707 (2010).

87. Optical integrated circuits, chapter 2, pp16, McGraw-Hill Professional, 1989.

88. S.H. Ahn and L J. Guo, "Dynamic Nanoinscribing for Continuous and Seamless Metal and Polymer Nanogratings," *Nano Lett.* **9**, 4392 (2009).

89. Y.T. Yoon, C.H. Park, and S.S. Lee, "Highly efficient color filter incorporating a thin metal-dielectric resonant structure," *Appl. Phys. Express* **5**, 022501 (2012).

90. C.H. Park, Y.T. Yoon, and S.S. Lee, "Polarization-independent visible wavelength filter incorporating a symmetric metal-dielectric resonant structure," *Opt. Express* **20**, 23769 (2012).

91. J.B. Pendry, A.J. Holden, W.J. Stewart, and I. Youngs, "Extremely low frequency plasmons in metallic nanostructures," *Phys. Rev. Lett.* **76**, 4773 (1996).

92. J.B. Pendry, A.J. Holden, D.J. Robbins, and W.J. Stewart, "Magnetism from conductors and enhanced nonlinear phenomena," *IEEE Trans. Microwave Theory Tech.* **47**, 2075 (1999).

93. D.R. Smith, J.B. Pendry, and M.C.K. Wiltshire, "Metamaterials and negative refractive index," *Science* **305**, 788 (2004).

94. C.M. Watts, X. Liu, and W.J. Padilla, "Metamaterial electromagnetic wave absorbers," *Adv. Mater.* **24**, OP98 (2012).

95. Y. Liu and X. Zhang, "Metamaterials: a new frontier of science and technology," *Chem. Soc. Rev.* **40**, 2494 (2011).

96. V.G. Veselago, "The electrodynamics of substances with simultaneously negative values of ε and μ," *Sov. Phys. Usp.* 10, 509 (1968).

97. J.B. Pendry, "Negative refraction makes a perfect lens," *Phys. Rev. Lett.* **85**, 3966 (2000).

98. A.F. Kaplan, Y.H. Chen, M.G. Kang, T. Xu, X. Luo, and L.J. Guo, "Subwavelength grating structures with magnetic resonances at visible frequencies fabricated by nanoimprint lithography for large area applications," *Jour. Vac. Sci. Technol. B,* **27**, 3175 (2009).

99. S. Xiao, U.K. Chettiar, A.V. Kildishev, V.P. Drachev, and V.M. Shalaev, "Yellow-light negative-index metamaterials," *Opt. Lett.* **34**, 3478 (2009).

100. S. Zhang, W. Fan, N.C. Panoiu, K.J. Malloy, R.M. Osgood, and S.R.J. Brueck, "Optical negative-index bulk metamaterials consisting of 2D perforated metal-dielectric stacks," *Opt. Express* **14**, 6778 (2006).

101. Z. Jacob, I.I. Smolyaninov, and E.E. Narimanov, "Broadband Purcell effect: radiative decay engineering with metamaterials," *Appl. Phys. Lett.* **100**, 181105 (2012).

102. J. Kim, V.P. Drachev, Z. Jacob, G.V. Naik, A. Boltasseva, E.E. Narimanov, and V.M. Shalaev, "Improving the radiative decay rate for dye molecules with hyperbolic metamaterials," *Opt. Express* **20**, 8100 (2012).

103. H.N.S. Krishnamoorthy, Z. Jacob, E.E. Narimanov, I. Kretzschmar, and V.M. Menon, "Topological transitions in metamaterials," *Science* **336**, 205 (2012).

104. X. Ni, S. Ishii, M.D. Thoreson, V.M. Shalaev, S. Han, S. Lee, and A.V. Kildishev, "Gain-assisted hyperbolic metamaterials," *QELS Conference* San Jose, CA (2012).

105. M. Yu, Y. Wang, W. Zhang, R. Guo, and X. Zhou, "Optical properties of strongly anisotropic metamaterials," *Appl. Phys. A* **108**, 65 (2012).

106. H. Luo, W. Hu, W. Shu, F. Li, and Z. Ren, "Superliminal group velocity in an anisotropic metamaterial," *Europhys. Lett.* **74**, 1081 (2006).

107. J. Rho, Z. Ye, Y. Xiong, X. Yin, Z. Liu, H. Choi, G. Bartal, and X. Zhang, "Spherical hyperlens for two-dimensional sub-diffractional imaging at visible frequencies," *Nat. Comm.* **1**, 1 (2010).

108. S. Thongrattanasiri and V.A. Podolskiy, "Hypergratings: nanophotonics in planar anisotropic metamaterials," *Opt. Lett.* **34**, 890 (2009).

109. A. Fang, T. Koschny, and C.M. Soukoulis, "Optical anisotropic metamaterials: negative refraction and focusing," *Phys. Rev. B* **79**, 245127 (2007).

110. Y. He, S. He, J. Gao, and X. Yang, "Giant transverse optical forces in nanoscale slot waveguides of hyperbolic metamaterials," *Opt. Express* **20**, 22372 (2012).

111. J. Yao, X. Yang, X. Yin, G. Bartal, and X. Zhang, "Three-dimensional nanometer-scale optical cavities of indefinite medium," *Proc. Nat. Acad. Sci.* **108**, 11327 (2011).

112. T.C. Choy, *Effective medium theory*, Oxford: Clarendon Press (1999).

113. P. Bouchon, F. Pardo, B. Portier, L. Ferlazzo, P. Ghenuche, G. Dagher, C. Dupuis, N. Bardou, R. Haïdar, and J.L. Pelouard, "Total funneling of light in high aspect ratio plasmonic nanoresonators," *Appl. Phys. Lett.* **98**, 191109 (2011).

114. Y.K. Wu, A.E. Hollowell, C. Zhang, and L.J. Guo, "Angle-insensitive plasmonic absorbers for structural color," *ACS Nano* (in submission).

115. X. Liu, T. Tyler, T. Starr, A.F. Starr, N.M. Jokerst, and W.J. Padilla, "Taming the blackbody with infrared metamaterials as selective thermal emitters," *Phys. Rev. Lett.* **107**, 045901 (2011).

116. M. Pu, M. Wang, C. Hu, C. Huang, Z. Zhao, Y. Wang, and X. Luo, "Engineering heavily doped silicon for broadband absorber in the terahertz regime," *Opt. Express* **20**, 25513 (2012).

117. H. Shi, J.G. Ok, H.W. Baac, and L.J. Guo, "Low density carbon nanotube forest as an index-matched and near perfect absorption coating," *Appl. Phys. Lett.* **99**, 211103 (2011).

118. Z.P. Yang, L. Ci, J.A. Bur, S.Y. Lin, and P.M. Ajayan, "Experimental observation of an extremely dark material made by a low-density carbon nanotube array," *Nano. Lett.* **8**, 446 (2011).

119. J.J. Talghader, A.S. Gawarikar, and R.P. Shea," Spectral selectivity in infrared thermal detection," *Light: Sci. & Appl.* doi:10.1038/lsa.2012.24 (2012).

120. J. Lehman, C. Engtrakul, T. Gennett, A. Dillon, "Single-wall carbon nanotube coating on a pyroelectric detector," *Appl. Opt.* **44**, 483 (2005).

121. Thomas Søndergaard, S.M. Novikov, T. Holmgaard, R.L. Eriksen, J. Beerman, Z. Han, K. Pedersen, and S.I. Bozhevolnyi, "Plasmonic black gold by adiabatic nanofocusing and absorption of light in ultra-sharp convex grooves," *Nat. Commun.* DOI: 10.1038/ncomms1976 (2012).

122. S.F. Leung, M. Yu, Q. Lin, K. Kwon, K.L. Ching, L. Gu, K. Yu, and Z. Fan, "Efficient photon capturing with ordered three-dimensional nanowell arrays," *Nano. Lett.* **12,** 3682 (2012).

123. T.J. Coutts, "A review of progress in thermophotovoltaic generation of electricity," *Renew. Sustain. Energy Rev.* **3**, 77 (1999).

124. P. Bouchon, C. Koechlin, F. Pardo, R. Haïdar, and J.L. Pelouard, "Wideband omnidirectional infrared absorber with a patchwork of plasmonic nanoantennas," *Opt. Lett.* **37**, 1038 (2012).

125. J. Hendrickson, J. Guo, B. Zhang, W. Buckwald, and R. Soref, "Wideband perfect light absorber at midwave infrared using multiplexed metal structures," *Opt. Lett.* **37**, 371 (2012).

126. C.W. Cheng, M.N. Abbas, C.W. Chiu, K.T. Lai, M.H. Shih, and Y.C. Chang, "Wide-angle polarization independent infrared broadband absorbers based on metallic multi-sized disk arrays," *Opt. Express* **20**, 10376 (2012).

127. J. Yang, X. Hu, X. Li, Z, Liu, Z. Liang, X. Jiang, and J. Zi, "Broadband absorption enhancement in anisotropic metamaterials by mirror reflections," *Phys. Rev. B* **80**, 125103 (2009).

128. J. Yang, X. Hu, X. Li, Z. Liu, X. Jiang, and J. Zi, "Cancellation of reflection and transmission at metamaterial surfaces," *Opt. Lett.* **35**, 16 (2010).

129. S. He, Y. He, and Y. Jin, "Revealing the truth about 'trapped rainbow' storage of light in metamaterials," *Sci. Reports* DOI: 10.1038/srep00583 (2012).

130. K.L. Tsakmakidis, A.D. Boardman, and O. Hess, "'Trapped rainbow' storage of light in metamaterials," *Nature* **450**, 397 (2007).

131. F. Ding, Y. Cui, X. Ge, Y. Jin, and S. He, "Ultra-broadband microwave metamaterial absorber," *Appl. Phys. Lett.* **100**, 103506 (2012).

132. H. Lee, Y. Park, J. Kim, J. Choi, and J. Kim, "Investigation of formation of spindt-type cathode by simulation and experiments," *J. Vac. Sci. Technol. B* **17**, 547 (1999).

133. D.N. Hill, J.D. Lee, J.K. Cochran, and A.T. Chapman, "Vapour deposited cone formation during fabrication of low voltage emitter array cathodes," *J. Mater. Sci.* **31**, 1789 (1996).

134. J. Zhu, C.M. Hsu, Z. Yu, S. Fan, and Y. Cui, "Nanodome solar cells with efficient light management and self-cleaning," *Nano. Lett.* **10**, 1979 (2010).

135. M. Fleischer, A. Weber-Bargioni, M.V.P. Altoe, A.M. Schwartzberg, P.J. Schuck, S. Cabrini, and D.P. Kern, "Nanocone near-field scanning optical microscopy probes," *ACS Nano* **5**, 2570 (2011).

136. Y. He, S. He, J. Gao, and X. Yang, "Nanoscale metamaterial optical waveguides with ultrahigh refractive indices," *J. Opt. Soc. Am. B* **29**, 2559 (2012).

137. T. Jiang, J. Zhao, and Y. Feng, "Stopping light by an air waveguide with anisotropic metamaterial cladding," *Opt. Express* **17**, 170 (2009).

138. W.T. Lu and S. Sridhar, "Slow light, open-cavity formation, and large longitudinal electric field on a slab waveguide made of indefinite permittivity metamaterials," *Phys. Rev. A* **82**, 013811 (2010).

139. M. Yan, L. Thylén, and M. Qiu, "Layered metal-dielectric waveguide: subwavelength guidance, leveraged modulation sensitivity in mode index, and reversed mode ordering," *Opt. Express* **19**, 3818 (2011).

140. J. Elser, A.A. Govyadinov, I. Avrutsky, I. Salakhutdinov, and V.A. Podolskiy, "Plasmonic nanolayer composites: coupled plasmon polaritons, effective-medium response, and subdiffraction light manipulation," *J. Nanomaterials* **2007**, 79469 (2007).

141. A. Candran, E.S. Barnard, J.S. White, and M.L. Brongersma, "Metal-dielectric-metal surface plasmon-polariton resonators," *Phys. Rev. B* **85**, 085416 (2012).

142. J. Yang, C. Sauvan, A. Jouanin, S. Collin, J.L. Pelouard, and P. Lalanne, "Ultrasmall metal-insulator-metal nanoresonators: impact of slow wave effects on quality factor," *Opt. Express* **20**, 16880 (2012).

143. H.A. Atwater and A. Polman, "Plasmonics for improved photovoltaic devices," *Nature Materials* **9**, 205 (2010).

144. Y. Jia, A. Cao, X. Bai, Z. Li, L. Zhang, N. Guo, J. Wei, K. Wang, H. Zhu, D. Wu, and P.M. Ajayan, "Achieving high efficiency silicon-carbon nanotube heterojunction solar cells by acid doping," *Nano Lett.* **11**, 1901 (2011).

145. Y. Lu and K. Reinhardt, "Manipulation of absorption in Si thin films with ordered nanostructures," *Phys. Status Solidi C* **8**, 839 (2011).

146. J.R. Sambles, G.W. Bradbery, and F. Yang, "Optical excitation of surface plasmons: an introduction," *Contemp. Phys.* **32**, 173 (1991).